

# **High Energy Gamma-rays from Active Galactic Nuclei**



# Contents

|          |  |           |
|----------|--|-----------|
| <b>1</b> | <b>Topics</b>  | <b>5</b>  |
| 1.1      | ICRANet participants . . . . .                                 | 5         |
| 1.2      | Students . . . . .   | 5         |
| 1.3      | Ongoing collaborations . . . . .                               | 5         |
| <b>2</b> | <b>Brief description</b>                                       | <b>7</b>  |
| <b>3</b> | <b>Publications-2017</b>                                       | <b>11</b> |
| 3.1      | Publications-2011-2016 . . . . .                               | 12        |
| <b>4</b> | <b>Comparing 3C 120 jet emission at small and large scales</b> | <b>15</b> |
| 4.1      | Introduction . . . . .   | 15        |
| 4.2      | Observations and data analysis of central region . . . . .     | 17        |
| 4.2.1    | Fermi LAT data extraction . . . . .                            | 17        |
| 4.2.2    | Temporal variability . . . . .                                 | 19        |
| 4.2.3    | Spectral analysis . . . . .                                    | 20        |
| 4.2.4    | Swift observations . . . . .                                   | 21        |
| 4.2.5    | Swift XRT . . . . .  | 22        |
| 4.2.6    | Swift UVOT . . . . .   | 22        |
| 4.3      | Chandra observations of the knots . . . . .                    | 23        |
| 4.4      | Modeling the spectral energy distributions . . . . .           | 24        |
| 4.4.1    | The core region . . . . .                                      | 24        |
| 4.4.2    | The large-scale jet emission . . . . .                         | 28        |
| 4.4.3    | Fitting technique . . . . .                                    | 29        |
| 4.5      | Results and discussion . . . . .                               | 30        |
| 4.5.1    | The origin of emission from the inner Jet . . . . .            | 31        |
| 4.5.2    | The origin of emission from knots . . . . .                    | 33        |
| 4.5.3    | Jet energetics . . . . .                                       | 35        |
| 4.6      | Summary . . . . .  | 36        |

|          |  |           |
|----------|--|-----------|
| <b>5</b> | <b>Rapid Gamma-ray variability of NGC 1275</b>         | <b>37</b> |
| 5.1      | Introduction . . . . .                                 | 37        |
| 5.2      | FERMI LAT OBSERVATIONS AND DATA ANALYSIS . . . . .     | 40        |
| 5.2.1    | Temporal variability . . . . .                         | 41        |
| 5.3      | Spectral analysis . . . . .                            | 44        |
| 5.3.1    | <i>Fermi</i> data . . . . .                            | 44        |
| 5.3.2    | Swift UVOT/XRT data . . . . .                          | 45        |
| 5.4      | RESULTS and DISCUSSIONS . . . . .                      | 45        |
| 5.4.1    | $\gamma$ -ray photon index variation . . . . .         | 47        |
| 5.4.2    | Minimum flux variability period: . . . . .             | 49        |
| 5.4.3    | The origin of emission . . . . .                       | 50        |
| 5.5      | SUMMARY . . . . .                                      | 51        |
| <b>6</b> | <b>High Energy Gamma-Ray Emission From PKS 1441+25</b> | <b>53</b> |
| 6.1      | Introduction . . . . .                                 | 53        |
| 6.2      | Fermi LAT DATA ANALYSIS . . . . .                      | 56        |
| 6.2.1    | Spectral analysis . . . . .                            | 57        |
| 6.2.2    | Temporal analysis . . . . .                            | 59        |
| 6.3      | BROADBAND SED MODELLING . . . . .                      | 62        |
| 6.3.1    | Broadband SED . . . . .                                | 62        |
| 6.3.2    | Theoretical modeling . . . . .                         | 64        |
| 6.3.3    | Fitting technique . . . . .                            | 65        |
| 6.3.4    | SED modeling and results . . . . .                     | 65        |
| 6.4      | DISCUSSION and CONCLUSIONS . . . . .                   | 69        |

# 1 Topics

- High energy gamma-rays from active galactic nuclei
- Galactic sources of high energy neutrinos
- High energy emission from gamma-ray bursts

## 1.1 ICRA Net participants

- Sahakyan Narek
- Aharonian Felix

## 1.2 Students

- Zargaryan David
- Baghmany an Vardan
- Karlica Mile
- Gasparyan Sargis
- Tumanyan Meri
- Mkrtchyan Tatevik

## 1.3 Ongoing collaborations

- Razmik Mirzoyan (Max Planck Institute for Physics, Munich, Germany)
- Paolo Giommi (ASI Science Data Center)

## 1 Topics

---

- Ulisses Barres de Almeida (Centro Brasileiro de Pesquisas Físicas - CBPF/MCT)
- Bernardo Fraga (Centro Brasileiro de Pesquisas Físicas - CBPF)

## 2 Brief description

The main scientific activities of our group are in the field of X- and gamma-ray Astrophysics and Astroparticle physics. The results from the data analysis of Swift XRT, NuStar, Chandra and Fermi LAT telescopes are used to investigate the particle acceleration and emission processes in the different classes of active galactic nuclei. The analysis of available data allows to investigate the emission processes and relativistic outflows in the most extreme regimes (keV-TeV).

Below we present several abstracts from the papers published in 2017.

- On a GRB afterglow model consistent with hypernovae observations

We describe the afterglows of long gamma-ray-burst (GRB) within the context of a binary-driven hypernova (BdHN). In this paradigm afterglows originate from the interaction between a newly born neutron star ( $\nu$ NS), created by an Ic supernova (SN), and a mildly relativistic ejecta of a hypernova (HN). Such a HN in turn result from the impact of the GRB on the original SN Ic. The observed power-law afterglow in the optical and X-ray bands is shown to arise from the synchrotron emission of relativistic electrons in the expanding magnetized HN ejecta. Two components contribute to the injected energy: the kinetic energy of the mildly relativistic expanding HN and the rotational energy of the fast rotating highly magnetized  $\nu$ NS. As an example we reproduce the observed afterglow of GRB 130427A in all wavelengths from the optical ( $10^{14}$  Hz) to the X-ray band ( $10^{19}$  Hz) over times from 604 s to  $5.18 \times 10^6$  s relative to the Fermi-GBM trigger. Initially, the emission is dominated by the loss of kinetic energy of the HN component. After  $10^5$  s the emission is dominated by the loss of rotational energy of the  $\nu$ NS, for which we adopt an initial rotation period of 2 ms and a dipole/quadrupole magnetic field of  $\lesssim 7 \times 10^{12}$  G/ $\sim 10^{14}$  G. This approach opens new views on the roles of the GRB interaction with the SN ejecta, on the mildly relativistic kinetic energy of the HN and on the pulsar-like phenomena of the  $\nu$ NS. This scenario differs from the current ultra-relativistic treatments of the afterglow in the collapsar-fireball model and it is, instead, consistent with the current

observations of the mildly relativistic regimes of X-ray flares,  $\gamma$ -ray flares and plateau emission in the BdHN.

- Comparing 3C 120 jet emission at small and large scales

Important information on the evolution of the jet can be obtained by comparing the physical state of the plasma at its propagation through the broad-line region (where the jet is most likely formed) into the intergalactic medium, where it starts to significantly decelerate. We compare the constraints on the physical parameters in the innermost ( $\leq$  pc) and outer ( $\geq$  kpc) regions of the 3C 120 jet by means of a detailed multiwavelength analysis and theoretical modeling of their broadband spectra. The data collected by Fermi LAT ( $\gamma$ -ray band), Swift (X-ray and ultraviolet bands) and Chandra (X-ray band) are analyzed together and the spectral energy distributions are modeled using a leptonic synchrotron and inverse Compton model, taking into account the seed photons originating inside and outside of the jet. The model parameters are estimated using the Markov Chain Monte Carlo method. The  $\gamma$ -ray flux from the inner jet of 3C 120 was characterized by rapid variation from MJD 56900 to MJD 57300. Two strong flares were observed on April 24, 2015 when, within 19.0 minutes and 3.15 hours the flux was as high as  $(7.46 \pm 1.56) \times 10^{-6} \text{ photon cm}^{-2} \text{ s}^{-1}$  and  $(4.71 \pm 0.92) \times 10^{-6} \text{ photon cm}^{-2} \text{ s}^{-1}$  respectively, with  $\geq 10\sigma$ . During these flares the apparent isotropic  $\gamma$ -ray luminosity was  $L_\gamma \simeq (1.20 - 1.66) \times 10^{46} \text{ erg s}^{-1}$  which is not common for radio galaxies. The broadband emission in the quiet and flaring states can be described as synchrotron self-Compton emission while inverse Compton scattering of dusty torus photons cannot be excluded for the flaring states. The X-ray emission from the knots can be well reproduced by inverse Compton scattering of cosmic microwave background photons only if the jet is highly relativistic (since even when  $\delta = 10$  still  $U_e/U_B \geq 80$ ). These extreme requirements can be somewhat softened assuming the X-rays are from the synchrotron emission of a second population of very-high-energy electrons. We found that the jet power estimated at two scales is consistent, suggesting that the jet does not suffer severe dissipation, it simply becomes radiatively inefficient.

- Rapid Gamma-ray variability of NGC 1275

We report on a detailed analysis of the  $\gamma$ -ray light curve of NGC 1275 using the Fermi large area telescope data accumulated in 2008-2017. Major  $\gamma$ -ray flares were observed in October 2015 and December 2016/January 2017 when

---

the source reached a daily peak flux of  $(2.21 \pm 0.26) \times 10^{-6} \text{ photon cm}^{-2} \text{ s}^{-1}$ , achieving a flux of  $(3.48 \pm 0.87) \times 10^{-6} \text{ photon cm}^{-2} \text{ s}^{-1}$  within 3 hours, which corresponds to an apparent isotropic  $\gamma$ -ray luminosity of  $\simeq 3.84 \times 10^{45} \text{ erg s}^{-1}$ . The most rapid flare had e-folding time as short as  $1.21 \pm 0.22$  hours which had never been previously observed for any radio galaxy in  $\gamma$ -ray band. Also  $\gamma$ -ray spectral changes were observed during these flares: in the flux versus photon index plane the spectral evolution follows correspondingly a counter clockwise and a clockwise loop inferred from the light curve generated by an adaptive binning method. On December 30, 2016 and January 01, 2017 the X-ray photon index softened ( $\Gamma_X \simeq 1.75 - 1.77$ ) and the flux increased nearly  $\sim 3$  times as compared with the quiet state. The observed hour-scale variability suggests a very compact emission region ( $R_\gamma \leq 5.22 \times 10^{14} (\delta/4) \text{ cm}$ ) implying that the observed emission is most likely produced in the subparsec-scale jet if the entire jet width is responsible for the emission. During the active periods the  $\gamma$ -ray photon index hardened, shifting the peak of the high energy spectral component to  $> \text{GeV}$ , making it difficult to explain the observed X-ray and  $\gamma$ -ray data in the standard one-zone synchrotron self-Compton model.

- High Energy Gamma-Ray Emission From PKS 1441+25

We present the  $\gamma$ -ray observations of the flat-spectrum radio quasar PKS 1441+25 ( $z=0.939$ ), using the Fermi large Area Telescope data accumulated during January - December 2015. A  $\gamma$ -ray flare was observed in January 24, when the flux increased up to  $(2.22 \pm 0.38) \times 10^{-6} \text{ photon cm}^{-2} \text{ s}^{-1}$  with the flux-doubling time scale being as short as  $\sim 1.44$  days. The spectral analysis shows that from April 13 to April 28, 2015 the MeV-to-GeV photon index has hardened and changes in the range of  $\Gamma = (1.73 - 1.79)$  for most of the time. The hardest photon index of  $\Gamma = 1.54 \pm 0.16$  has been observed on MJD 57131.46 with  $11.8\sigma$  which is not common for flat-spectrum radio quasars. For the same period the  $\gamma$ -ray spectrum shows a possible deviation from a simple power-law shape, indicating a spectral cutoff at  $E_{cut} = 17.7 \pm 8.9 \text{ GeV}$ . The spectral energy distributions during quiescent and flaring states are modeled using one-zone leptonic models that include the synchrotron, synchrotron self Compton and external inverse Compton processes; the model parameters are estimated using the Markov Chain Monte Carlo method. The emission in the flaring states can be modeled assuming that either the bulk Lorentz factor or the magnetic field has increased. The modeling shows that

## *2 Brief description*

---

there is a hint of hardening of the low-energy index ( $\sim 1.98$ ) of the underlying non-thermal distribution of electrons responsible for the emission in April 2015. Such hardening agrees with the  $\gamma$ -ray data, which pointed out a significant  $\gamma$ -ray photon index hardening on April 13 to 28, 2015.

### 3 Publications-2017

- D. Zargaryan, S. Gasparyan, V. Baghmanyan and N. Sahakyan, "Comparing 3C 120 jet emission at small and large scales", *Astronomy & Astrophysics*, Volume 608, id. A37, 10, 2017.
- U. Barres de Almeida, F. Bernardo, P. Giommi, N. Sahakyan, S. Gasparyan and C. Brandt, "Long-Term Multi-Band and Polarimetric View of Mkn 421: Motivations for an Integrated Open-Data Platform for Blazar Optical Polarimetry", *Galaxies*, vol. 5, issue 4, p. 90, 2017.
- V. Baghmanyan, S. Gasparyan and N. Sahakyan, "Rapid Gamma-Ray Variability of NGC 1275", *The Astrophysical Journal*, Volume 848, Issue 2, article id. 111, 8, 2017.
- N. Sahakyan and S. Gasparyan "High energy gamma-ray emission from PKS 1441+25", *Monthly Notices of the Royal Astronomical Society*, 470, 3, p.2861-2869, 2017.
- N. Sahakyan, V. Baghmanyan, and D. Zargaryan, "Gamma-ray Emission from Non-Blazar AGNs", *AIP Conference Proceedings*, Volume 1792, Issue 1, id.050002, 2017.
- N. Sahakyan and S. Gasparyan, "High Energy Gamma-Rays From PKS 1441+25", *AIP Conference Proceedings*, Volume 1792, Issue 1, id.050005, 2017.
- V. Baghmanyan, "Gamma-Ray Variability of NGC 1275", *AIP Conference Proceedings*, Volume 1792, Issue 1, id.050007, 2017.
- D. Zargaryan, "The Gamma-Ray Emission from Broad-Line Radio Galaxy 3C 120", *AIP Conference Proceedings*, Volume 1792, Issue 1, id.050008, 2017.

### 3.1 Publications-2011-2016

- N. Sahakyan, "Galactic sources of high energy neutrinos: Expectation from gamma-ray data", EPJ Web of Conferences, Volume 121, id.05005, 2016.
- Sahakyan, N., Zargaryan, D. and Baghmanyany, V. "On the gamma-ray emission from 3C 120", Astronomy & Astrophysics, Volume 574, id.A88, 5 pp., 2015.
- Sahakyan, N., Yang, R., Rieger, F., Aharonian, F. and de Ona-Wilhelmi, E. "High Energy Gamma Rays from Centaurus a" Proceedings of the MG13 Meeting on General Relativity ISBN 9789814623995, pp. 1028-1030, 2015.
- Sahakyan, N., Piano, G. and Tavani, M. "Hadronic Gamma-Ray and Neutrino Emission from Cygnus X-3", The Astrophysical Journal, Volume 780, Issue 1, article id. 29, 2014.
- Sahakyan, N., Rieger, F., Aharonian, F., Yang, R., and de Ona-Wilhelmi, E. "On the gamma-ray emission from the core and radio lobes of the radio galaxy Centaurus A", International Journal of Modern Physics: Conference Series, Volume 28, id. 1460182, 2014.
- Sahakyan, N., Yang, R. Aharonian, F. and Rieger, F., " Evidence for a Second Component in the High-energy Core Emission from Centaurus A?", The Astrophysical Journal Letters, Volume 770, Issue 1, L6, 2013.
- Yang, R.-Z., Sahakyan, N., de Ona Wilhelmi, E., Aharonian, F. and Rieger, F., "Deep observation of the giant radio lobes of Centaurus A with the Fermi Large Area Telescope", Astronomy & Astrophysics, 542, A19, 2012.
- Sahakyan, N., "High energy gamma-radiation from the core of radio galaxy Centaurus A", Astrophysics, 55, 14, 2012.
- Sahakyan, N., "On the Origin of High Energy Gamma-Rays from Giant Radio Lobes Centarus A", International Journal of Modern Physics Conference Series, 12, 224, 2012.

- Vissani, F., Aharonian, F. and Sahakyan, N., "On the detectability of high-energy galactic neutrino sources", *Astroparticle Physics*, 34, 778, 2011.



# 4 Comparing 3C 120 jet emission at small and large scales

## 4.1 Introduction

The recent observations in the High Energy (HE;  $\geq 100$  MeV)  $\gamma$ -ray band show that the extragalactic  $\gamma$ -ray sky is dominated by the emission of Active Galactic Nuclei (AGNs) of different types. Dominant in these are blazars - an extreme class of AGNs which have jets that are forming a small angle with respect to the line of sight [92]. Blazars are very bright and luminous sources known to emit electromagnetic radiation in almost all frequencies that are currently being observed, ranging from radio to Very High Energy (VHE;  $> 100$  GeV)  $\gamma$ -ray bands. Their broadband spectrum is mainly dominated by non-thermal emission produced in a relativistic jet pointing toward the observer. Other important class of  $\gamma$ -ray emitting AGNs observed by Fermi Large Area Telescopes (Fermi LAT) are radio galaxies with relativistic jets at systematically larger angles [4, 58]. Due to larger jet inclination angle as compared with blazars, the jet emission is not significantly Doppler boosted, making it less prevalent over such components as the radiation from mildly relativistic outflows or emission from extended structures. This opened a new window to have an insight into the particle acceleration and emission processes in different components of AGNs.

The radio galaxy 3C 120, at a distance of  $\approx 144.9$  Mpc, is an active and powerful emitter in all the observed wavebands. In the radio band, its characteristics are closer to the Fanaroff-Riley class I radio sources [26] with a powerful one-sided radio jet from sub- $pc$  to  $100$  kpc scales [48]. The one-sided parsec-scale jet has been studied by long baseline interferometry and superluminal motion has been observed with apparent speed up to  $4-6 c$  [50, 44, 43]. Recently, using X-ray and radio observations, [63] found that the dips in the X-ray emission are followed by ejections of bright superluminal knots in the radio jet which clearly establishes an accretion-disk-jet connection. The kpc-

scale jet of 3C 120 has a complex structure with several knots, k4, k7, s2, s3, and k25 (see Fig. 2 of [48], where on the 1.6 GHz radio contours the section of the jet with knot labels is shown), detected in the radio, optical, and X-ray bands [47, 48]. The knots are labeled by their distance from the core in arcseconds (e.g., k4, k7) and the smooth sections of the jet detected in the optical band [49] are labeled as s2 and s3. These knots appeared to have interesting morphology and spectra, more tricky among which is the X-ray emission from the knot k25: it has a very weak radio flux but it is bright in the X-ray band. It is a real challenge for one-zone synchrotron emission scenario to interpret the emission from k25 in case of which large deviation from the minimal energy condition is required. It has been suggested that X-rays might be produced through the synchrotron radiation of an electron population distinct from that responsible for the radio emission [48]. Alternative theories such as proton synchrotron emission [11] or inverse-Compton scattering of CMB photons [96] have also been proposed. However, it is to date not clear which is the exact mechanism responsible for the X-ray emission.

The core of 3C 120's jet itself has interesting and peculiar features. It is very bright in the X-ray band with a flux of  $\approx 5 \times 10^{-11}$  erg cm<sup>-2</sup>s<sup>-1</sup> at 2-10 keV, variable on time scales from days to months [45]. The  $\gamma$ -rays from 3C 120 had been already detected by Fermi LAT during first 15 months' scan of the whole sky [4] which was then confirmed by the data accumulated for two years [58]. Also a long-term (several months) variability had been found using the five-year Fermi LAT data [81] with short periods (days and hours) of brightening [89, 54]. Inverse Compton scattering of synchrotron photons seems to be the mechanism responsible for the  $\gamma$ -ray emission from 3C 120 [89, 81] while the flares and the fast  $\gamma$ -ray variability are explained within more complex structured jet scenarios [54].

Combining of the data derived at the sub-*pc* and kilo-parsec regions of the same jet could greatly help to understand the features of powerful extragalactic jets, e.g., shed some light on the evolution and propagation of the jets from the central engine to the outer regions, where the jet is starting to significantly decelerate. This approach can be fruitfully applied to the sources showing a large-scale jet long enough to be resolved by Chandra. Unfortunately, the best-studied blazars do not tend to have well-studied large-scale jets, precisely because the blazars are most closely aligned with the line of sight, reducing the projected angular dimension of the large-scale jet. Thus, only a few jets can be studied on both scales. The prominent features of 3C 120, e.g., the strong jet well resolved in both small (pc) and large (kpc) scales

makes this object an ideal target for investigation of the processes occurring in the powerful jet along its propagation.

The low statistics in the  $\gamma$ -ray band did not allow to study the flux changes on sub-month scales (the light curves contain many upper limits). The recent update of the Fermi LAT event-level analysis from PASS7 to PASS8 has significantly improved the event reconstruction and classification which increased the sensitivity and improved the angular resolution. Combining this with the data accumulated for a longer period (8 years) would significantly improve the statistics allowing to perform a detailed study of the  $\gamma$ -ray flux evolution in time. Also, the analysis of the Swift data will allow to explore the emission from the core region with the help of contemporaneous Spectral Energy Distributions (SEDs). Moreover, due to several Chandra observations of the large-scale jet of 3C 120 in 2001-2016, the overall exposure is large enough to perform a spectral analysis of the X-ray data. This motivated us to have a new look on the emission from the jet of 3C 120 in small and large scales using the most recent data available.

The paper is structured as follows. The analyses of Fermi LAT and Swift XRT/UVOT data are presented in Section 6.2. The analysis of Chandra data is described in Section 6.3. The modeling of the emission from the core and knots is presented in Section 6.4. The results are discussed in Section 5.5 and summarized in Section 4.6.

## 4.2 Observations and data analysis of central region

### 4.2.1 Fermi LAT data extraction

On board the Fermi satellite, LAT is a pair-conversion telescope designed to detect HE  $\gamma$ -rays in the energy range 20 MeV - 300 GeV. Operating since August 4, 2008, it is always in the survey mode by default, scanning the entire sky every  $\sim 3$  hours, thereby providing continuous monitoring of  $\gamma$ -ray sources. Details about the Fermi LAT can be found in [17].

In the current paper we analyze the data accumulated for 8 years, from the beginning of the Fermi LAT mission up to August 8, 2016 (MET 239557417-460339204). Fermi LAT Science Tool version v10r0p5 is used with the instrument response function P8R2.SOURCE.V6. The recently updated PASS8 ver-

## 4 Comparing 3C 120 jet emission at small and large scales

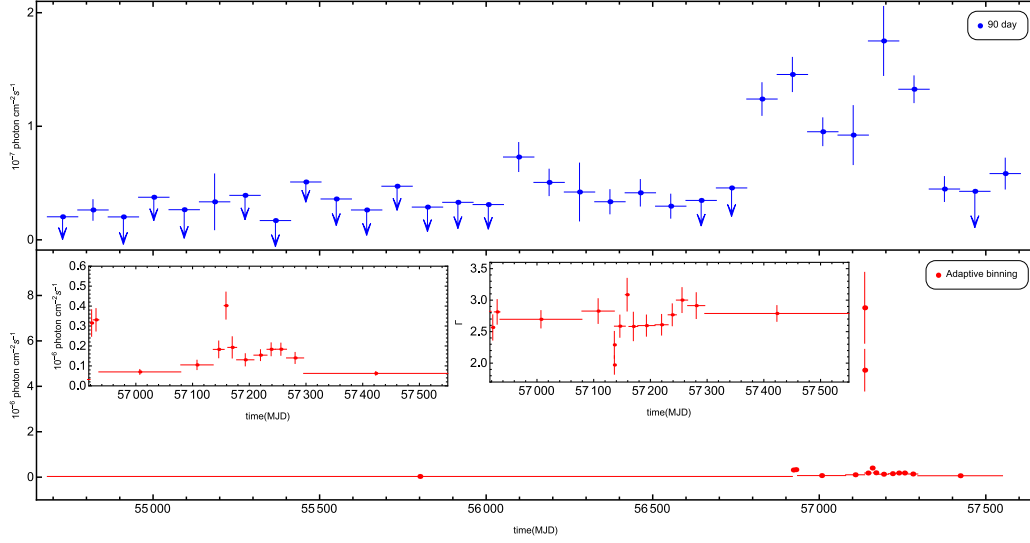


**Figure 4.1:** The  $\gamma$ -ray light curve of 3C 120 from August 4, 2008, to August 4, 2016. (a) The bin intervals correspond to 90 days. (b) The light curve obtained by adaptive binning method assuming 20 % of uncertainty. The change of photon index is shown in the insert.

sion of the data in the energy range between 100 MeV - 300 GeV is analyzed. The entire data set is filtered with `gtselect` and `gtmktime` tools and only the events with a high probability of being photons `evclass=128`, `evtype=3` have been considered. The zenith angle cutoff  $> 90^\circ$  is made to exclude atmospheric  $\gamma$ -rays from the Earth limb that can be a significant source of background.

The photons from a circular Region of Interest (ROI) centered on VLBI radio positions of 3C 120 (RA,dec) = (68.296, 5.354) are used in the analysis. The photons are binned within  $14.1^\circ \times 14.1^\circ$  square regions with `gtbin` tool, with a stereographic projection into  $0.1^\circ \times 0.1^\circ$  pixels. In order to account for the emission from other sources within ROI, the model file is generated using the Fermi-LAT third source catalog [7] and the sources within  $10^\circ + 5^\circ$  from the position of 3C 120 are included in the model file. Since 3C 120 is not included in the catalog, a point-like source in the known location of 3C 120 was added to the model file. The Galactic background component is modeled using the LAT standard diffuse background model `gll_iem_v05_rev1` and `iso_source_v05 ?` for the isotropic  $\gamma$ -ray background. The normalization of

background models as well as the fluxes and spectral indices of the sources within  $10^\circ$  are left as free parameters during the analysis.

### 4.2.2 Temporal variability

In order to have SEDs with contemporaneous data for broadband modeling we created  $\gamma$ -ray light curves with different time binning. The  $\gamma$ -ray light curve is calculated with the unbinned likelihood analysis method implemented in the `gtlike` tool. (0.1 – 300) GeV photons are used in the analysis with the appropriate quality cuts applied in the data selection. The photon indices of all background sources are fixed to the best guess values obtained in full time analysis in order to reduce the uncertainties in the flux estimations. The power-law index of 3C 120 is first considered as a free parameter and then as a fixed one. Since no variability is expected for the background diffuse emission, the normalization of both background components is also fixed to the values obtained for the whole time period.

The light curve obtained for 90-day binning is shown in the upper panel of Fig. 6.2. Before  $\approx$  MJD 56000 (March 14, 2012), the source is mostly undetectable by Fermi LAT: only in two of the total 15 cases, the source detection significance exceeded the required threshold of  $4\sigma$ . Then the source flux was high enough to be detected by Fermi LAT, and up to  $\approx$  MJD 56800 it remained constant with no significant changes. Starting from  $\approx$  MJD 56800, the flux substantially increased up to a few times  $10^{-7} \text{ photon cm}^2 \text{ s}^{-1}$  and remained so till  $\approx$  MJD 57350. The standard  $\chi^2$  analysis revealed a highly variable  $\gamma$ -ray flux, where the probability of the flux to be constant is  $p(\chi^2) \ll 5\%$ . No strong variation of the  $\gamma$ -ray photon index is found during the time under consideration.

The active state identified above can be further investigated using denser time sampling. However, considering the relatively weak flux, the light curve will contain many upper limits preventing to make any conclusion. Therefore, a light curve generated with an adaptive binning method is used. In this method, the time bin widths are flexible and chosen to produce bins with constant flux uncertainty [60]. This method allows detailed investigation of flux changes in time, since at times of high fluxes, the time bins are narrower than during lower ones, therefore the rapid changes of the fluxes can be found. In order to reach the necessary relative flux uncertainty, the integral fluxes are computed above the optimal energies [60] ( $E_0 = 183.2 \text{ MeV}$

in this case). Also, in order to improve the accuracy of the method, the flux of bright sources which lie close to 3C 120 have been taken into account. This is done by providing the parameters of confusing sources during the adaptive binning light curve calculations.

For 20% adaptively binned intervals, light curve is generated for the energy range 100 MeV-300 GeV (lower panel in Fig. 6.2). As it is expected, initially it took a long time to reach the necessary 20 % uncertainty. Indeed, the first bin contains the data from the start of the mission to MJD 56919.31(19 September 2014), amounting to more than 6 years. Afterwards, it took shorter time to reach the required uncertainty. The most dramatic increase in the  $\gamma$ -ray flux was observed on April 24, 2015. First, within 19.0 min the flux reached  $(7.46 \pm 1.56) \times 10^{-6} \text{ photon cm}^{-2} \text{ s}^{-1}$  with  $\Gamma = 2.29 \pm 0.21$  and  $11.2\sigma$  detection significance. Then for another 3.15 hours it was as high as  $(4.71 \pm 0.92) \times 10^{-6} \text{ photon cm}^{-2} \text{ s}^{-1}$  with  $\Gamma = 1.97 \pm 0.14$  and  $12.7\sigma$ . Then the flux slowly decreased down to a few times  $10^{-7} \text{ photon cm}^{-2} \text{ s}^{-1}$  with the bin size varying within 10 to 35 days. The source was in an active state up to  $\approx$  MJD 57300 and then turned again into its quiescent state, in which case the data should be accumulated for  $\simeq 254$  days.

### 4.2.3 Spectral analysis

In order to investigate the emission from 3C 120 in its quiet and active states, the  $\gamma$ -ray spectra were extracted from the following periods:

- 1) long quiescent states, namely, between MJD 54682.65 and MJD 56919.31.
- 2) the active state after MJD 56919.31. The period overlaps with the Swift observations on MJD 56934.19, 56937.70 and 5638.50. Although the Swift observation lasted several thousands of seconds, in order to increase the  $\gamma$ -ray photon statistics, the Fermi LAT spectrum was extracted from 15 days (MJD 56919.31-56934.76), when the source showed a comparable flux level as inferred from the light curve obtained by an adaptive binning method.

The spectrum of 3C 120 was modeled as a power-law function ( $dN/dE \sim N_0 E^{-\Gamma}$ ) with the normalization and index considered as free parameters. In order to find the best matches between the spectral models and events, a binned likelihood analysis is performed with *gtlike* for the first period, while an unbinned analysis was applied for the second one. The spectral fitting

**Table 4.1:** Parameters of spectral analysis

| Swift XRT             |   |  |                  |
|-----------------------|---|--|------------------|
| Obsid                 | $\Gamma_X$                                    | $\nu F_\nu$  | reduced $\chi^2$ |
|                       | MJD   | $\times 10^{-11} \text{erg cm}^{-2} \text{s}^{-1}$ |                  |
| 37594002              | $1.42 \pm 0.07$                               | $4.27 \pm 0.18$                                    | 0.43             |
| 37594004              | $1.53 \pm 0.08$                               | $2.41 \pm 0.11$                                    | 0.75             |
| 37594042              | $1.76 \pm 0.04$                               | $6.73 \pm 0.15$                                    | 1.21             |
| 37594048              | $1.72 \pm 0.04$                               | $5.37 \pm 0.12$                                    | 1.05             |
| 37594049              | $1.80 \pm 0.06$                               | $3.73 \pm 0.13$                                    | 0.86             |
| Fermi LAT             |   |  |                  |
| date                  | Flux  | $\Gamma$   | TS               |
|                       | $10^{-8} \text{photon cm}^{-2} \text{s}^{-1}$ |  |                  |
| 2008/08/04-2014/09/19 | $2.87 \pm 0.49$                               | $2.79 \pm 0.08$                                    | 179.43           |
| 2014/09/19-2014/10/04 | $24.9 \pm 4.21$                               | $2.57 \pm 0.16$                                    | 90.5             |
| Chandra               |   |  |                  |
| Region                | $\Gamma_X$                                    | $\nu F_\nu$  | reduced $\chi^2$ |
|                       |   | $\times 10^{-14} \text{erg cm}^{-2} \text{s}^{-1}$ |                  |
| k4                    | $1.82 \pm 0.10$                               | $15.97 \pm 2.3$                                    | 1.03             |
| k7                    | $2.72 \pm 0.66$                               | $1.85 \pm 0.82$                                    | 1.03             |
| s2                    | $2.64 \pm 1.26$                               | $0.78 \pm 0.51$                                    | 0.81             |
| s3                    | $2.14 \pm 0.28$                               | $0.45 \pm 0.37$                                    | 0.89             |
| k25 inner             | $1.63 \pm 0.22$                               | $3.89 \pm 1.42$                                    | 0.98             |
| k25 outer             | $1.62 \pm 0.11$                               | $12.16 \pm 1.9$                                    | 0.79             |
| k25 new               | $1.80 \pm 0.19$                               | $6.28 \pm 1.67$                                    | 0.91             |

results are summarized in Table 4.1 and the plot of the SEDs is shown in Fig. 4.2. During the flaring periods, the  $\gamma$ -ray flux increased nearly by an order of magnitude and the photon index hardened.

#### 4.2.4 Swift observations

Swift satellite [29] observed 3C 120 in its  $\gamma$ -ray quiescent and active states. As the X-ray flux varies as well (see [www.bu.edu/blazars/VLBA\\_GLAST/3c120.html](http://www.bu.edu/blazars/VLBA_GLAST/3c120.html)), we have selected the observations made on MJD 55252.70 and MJD 55800.25 when the X-ray flux also was low. During the  $\gamma$ -ray active state 3C 120 was observed only three times, on MJD 56934.19, MJD 56937.70 and MJD 56938.50. The data from two of the instruments on board Swift, the UltraViolet and Optical Telescope (UVOT) and the X-Ray Telescope (XRT), have been used in the

analysis.

### 4.2.5 Swift XRT

The Swift-XRT observations were made in the photon counting (PC) (Obsid 37594002, 37594004) and windowed timing (WT) (Obsid 37594042, 37594048, 37594049) modes. The data were analyzed using the XRTDAS software package (v.3.3.0) distributed by HEASARC as part of the HEASoft package (v.6.21). The source spectrum region was defined as a circle with a radius of 30 pixels ( $\sim 71''$ ) at the center of the source, while the background region - as an annulus centered at the source with its inner and outer radii being 80 ( $\sim 190''$ ) and 120 pixels ( $\sim 280''$ ), respectively. For the PC-mode observation 37594004, the count rate was above 0.5 count/s, being affected by the piling up in the inner part of the PSF. This effect was removed by excluding the events within a 4-pixel radius circle centered on the source position. Then, using `xrtmkarf` task, ancillary response files were generated by applying corrections for the PSF losses and CCD defects.

The spectrum was rebinned to have at least 20 counts per bin, ignoring the channels with energy below 0.5 keV, and fitted using XSPEC v12.9.1a. The results of the fit are given in Table 4.1 and the corresponding spectra are shown in Fig. 4.2. The 0.5-6.0 keV spectrum is well fitted by an absorbed power-law model with column density  $N_H = 1.06 \times 10^{21} \text{ cm}^{-2}$ . Although the X-ray flux did not increase significantly (the highest flux of  $F_{0.5-6 \text{ keV}} \simeq (6.73 \pm 0.15) \times 10^{-11} \text{ erg cm}^{-2} \text{ s}^{-1}$  observed on October 4, 2014, exceeds the lowest one  $\sim 2.8$  times), the X-ray photon index softened, changing in the range of  $\Gamma_x = (1.76 - 1.80)$  during the bright  $\gamma$ -ray periods.

### 4.2.6 Swift UVOT

In the analysis of the Swift UVOT data, the source counts were extracted from an aperture of  $5.0''$  radius around the source. The background counts were taken from the neighboring circular region having a radius of  $20''$ . The magnitudes were computed using the `uvotsource` tool (HEASOFT v6.21), corrected for extinction according to [43] using  $E(B - V) = 0.256$  from [45] and zero points from [16], converted to fluxes following [40]. The corresponding spectra are shown in Fig. 4.2. The optical-UV data points harden during the flaring periods.

### 4.3 Chandra observations of the knots

In the public archive we found 5 observations (ObsId 3015, 16221, 17564, 17565, 17576) of 3C 120 with Chandra telescope, the overall observation time being 251.86 ksec. We applied the standard data reduction procedure, using the Chandra Interactive Analysis of Observations (CIAO) 4.8 with Chandra Calibration Database (CALDB) version 4.7.2. We checked for flaring background events and did not find any significant flares. The readout streaks were removed for each observation and the events files were then re-projected to a single physical coordinate system (using observation 16221 as a reference). Also, to reduce the uncertainties caused by the position offsets of different observations, we made astrometric corrections, following the thread from [www.cxc.harvard.edu/ciao/threads/reproject\\_aspect/](http://www.cxc.harvard.edu/ciao/threads/reproject_aspect/). For each knot, the source region and the background are selected based on the position and shape given in Table 3 and Fig. 3 of [48].

We extracted the spectra and created weighted response files for each observation, using the `specextract` script. The knots spectra were rebinned using a different count threshold depending on the total number of counts, and fitted in the 0.5-10 keV energy range using a power-law with the Galactic absorption model (column density fixed at  $N_H = 1.06 \times 10^{21} \text{ cm}^{-2}$ ), where the index and the normalization are allowed to vary freely. The spectral fit was done with Sherpa using `levmar` optimization method and `chi2datavar` statistics.

The fitted spectral parameters are summarized in Table 4.1. The X-ray emission from the core is heavily saturated making it impossible to study the innermost parts of the jet. However, the nearby k4 knot's emission is well resolved from the core, the X-ray spectral index being  $1.82 \pm 0.1$  and the flux being  $(1.60 \pm 0.23) \times 10^{-13} \text{ erg cm}^{-2} \text{ s}^{-1}$ . The net counts from k7, s2 and s3 knots are relatively low  $< 50$  (as compared with  $> 100$  from other knots), not enough for a detailed spectral fitting. The fitting resulted in a steep X-ray slope ( $> 2.0$ ) and a relatively faint X-ray flux ( $\leq 10^{-14} \text{ erg cm}^{-2} \text{ s}^{-1}$ ). Because of low statistics and estimated large uncertainties, we did not consider them further. Following [48] we also sub-divide k25 into inner, outer and new regions which have different properties in the radio band (the inner refers to the upstream edge and the outer refers to the western edge, see Fig. 3 of [48]). The X-ray emission from all 3 regions has harder X-ray emission spectra ( $\leq 1.8$ ) with the X-ray flux varying within  $(3.89 - 12.16) \times 10^{-14} \text{ erg cm}^{-2} \text{ s}^{-1}$ . It is interesting to note that the flux of k25 outer is at the same level as that of the bright k4 but with a significantly harder X-ray spectral index of

## 4 Comparing 3C 120 jet emission at small and large scales

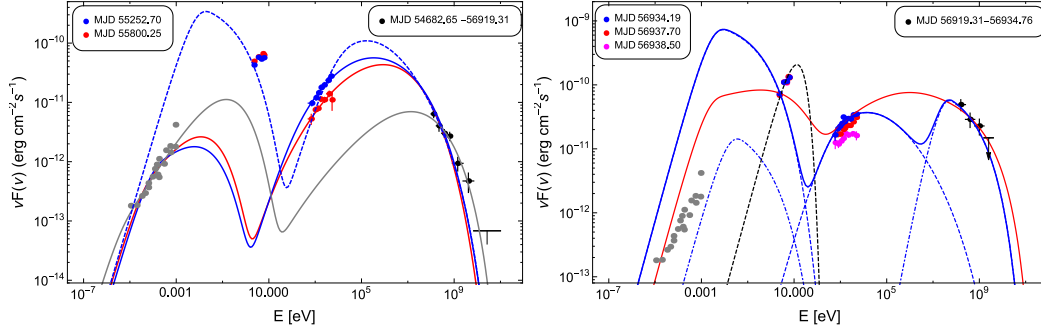


**Figure 4.2:** The broadband SED of 3C 120 core emission for quiescent (left) and flaring (right) states. Left panel: The blue and red solid lines are the synchrotron/SSC model fitting for two different X-ray fluxes, taking into account the radio data and assuming Swift UVOT data are upper limits. Instead the dashed blue line is calculated assuming optical/UV emission is also produced by the jet. Right panel: The SED in flaring state fitting with one-zone synchrotron/SSC (red solid line) and two zone SSC+ EIC (blue solid line) models. The model parameters are presented in Table 2.

$\Gamma_X = 1.62 \pm 0.11$ . The knot SEDs shown in Fig. 4.3 have been calculated by `sample_energy_flux` in Sherpa.

## 4.4 Modeling the spectral energy distributions

### 4.4.1 The core region

The broadband SEDs of 3C 120 core's emission in its quiescent and flaring states are shown in Fig. 4.2 with the radio data (gray) from [42, 89] where the data from the period corresponding to the  $\gamma$ -ray quiescent state of 3C 120 is analyzed. As in the previous studies [42, 81, 89, 54] the SEDs hint at the existence of two nonthermal emission peaks in the IR/optical/UV and HE  $\gamma$ -ray bands. The UVOT data revealed a rather hard optical-UV spectrum which indicates that perhaps direct thermal emission from the accretion disk was being observed [31, 36, 35].

Taking into account the results of the previous studies of other Fermi LAT-observed radio galaxies [1, 5, 81, 89], the multiwavelength emission of 3C 120 is modeled using the synchrotron/Synchrotron Self-Compton (SSC) [62, 20,

**Table 4.2:** Parameters obtained from the fit of the emission from the inner jet of 3C 120 during quiescent and flaring states.

|  | Parameter                       | SSC(blue-dashed)                   | SSC (red)                      | SSC                       | SSC+EIC   |
|--|---------------------------------|------------------------------------|--------------------------------|---------------------------|---|
| Doppler factor                         | $\delta$                        | 4                                  | 4                              | 6                         | 4(6)  |
| Normalization of electron distribution | $N'_0 \times 10^{50} eV^{-1}$   | $15292.18^{+34383.07}_{-10357.06}$ | $16.77^{+176.69}_{-14.02}$     | $1.96^{+2.75}_{-1.13}$    | $1713.92^{+19.88}_{-18.69}(817.55^{+118.64}_{-117.96})$ |
| Electron spectral index                | $\alpha$                        | $3.12^{+0.15}_{-0.16}$             | $1.85^{+0.31}_{-0.22}$         | $2.79^{+0.16}_{-0.13}$    | $3.12 \pm 0.22(3.24^{+0.89}_{-0.80})$                   |
| Minimum electron energy                | $E'_{min}$ (MeV)                | $354.51^{+27.20}_{-24.55}$         | $228.18^{+92.19}_{-120.10}$    | $67.57^{+18.03}_{-20.65}$ | $117.23^{+11.80}_{-12.64}(514.51^{+569.19}_{-352.58})$  |
| Cut off electron energy                | $E'_{cut}$ (GeV)                | $3.21^{+0.60}_{-0.46}$             | $4.61^{+1.63}_{-0.77}$         | $6.32^{+2.93}_{-1.48}$    | $1.68^{+0.42}_{-0.41}(4.05^{+5.37}_{-2.10})$            |
| Maximum electron energy                | $E'_{max}$ (TeV)                | $2.30^{+3.84}_{-1.54}$             | $1.90^{+3.02}_{-1.26}$         | $1.83^{+2.19}_{-1.27}$    | $10.71^{+4.64}_{-6.56}(54.56^{+75.36}_{-40.27})$        |
| Magnetic field                         | B [G]                           | $0.16^{+0.006}_{-0.007}$           | $0.0023^{+0.00025}_{-0.00018}$ | $0.86^{+0.11}_{-0.09}$    | $0.63 \pm 0.12(0.11^{+0.11}_{-0.08})$                   |
| Electron energy density                | $U_e(erg cm^{-3})$              | $1.02 \times 10^{-3}$              | $1.99 \times 10^{-2}$          | 0.14                      | $4.39 \times 10^{-4}(0.25)$                             |
| Jet power in magnetic field            | $L_B \times 10^{44} erg s^{-1}$ | 2.58                               | $4.98 \times 10^{-4}$          | 0.22                      | 38.34(0.0034)   |
| Jet power in electrons                 | $L_e \times 10^{44} erg s^{-1}$ | 2.46                               | 48.00                          | 1.09                      | 1.06(2.02)  |

34] and/or External Inverse-Compton (EIC) [86] models. The radio through optical emission is due to the synchrotron emission of energetic electrons in the homogeneous, randomly oriented magnetic field, while the X-ray to HE  $\gamma$ -ray emission is due to the inverse Compton scattering of the same synchrotron photons or photons of external origin.

In the flaring state (right panel of Fig. 4.2) the X-ray flux moderately increased and the spectrum softened, while the HE  $\gamma$ -ray flux increased and its spectrum shifted to higher energies. Within the synchrotron/SSC or EIC scenarios such modifications can be explained by means of introducing changes in the electron acceleration, increase of the comoving radius and bulk Lorentz factor [72] or due to the contribution from external photons. Here we discuss the following possibilities: (i) in the quiescent state the jet energy dissipation occurs close to the central black hole and the dominant mechanism is the synchrotron/SSC emission, (ii) in the flaring period again the dominant processes is SSC, although the emission region has a higher bulk Lorentz factor, and (iii) the optical/UV/X-ray emission is due to the synchrotron/SSC emission from an extended and slow-moving region, while the HE  $\gamma$ -rays come from a compact and fast-moving region, where EIC is dominating. This is similar to the scenario adopted by [90] to explain the very fast VHE  $\gamma$ -ray variations and the hard GeV spectrum of PKS 1222+216. The choice of this scenario is justified since strong changes are observed only in the  $\gamma$ -ray band. The emission region (the "blob") is assumed to be a sphere with a radius of  $R$  which carries a magnetic field with an intensity of  $B$  and a population of rela-

tivistic electrons which have a power-law with an exponential cut-off energy distribution expected from shock acceleration theories [52]:

$$N'_e(E'_e) = N'_0 \left( E'_e / m_e c^2 \right)^{-\alpha} \text{Exp}[-E'_e / E'_{cut}] \quad (4.4.1)$$

for  $E'_{min} \leq E'_e \leq E'_{max}$  where  $E'_{min}$  and  $E'_{max}$  are the minimum and maximum electron energies, respectively. The total electron energy  $U_e = \int_{E'_{min}}^{E'_{max}} E'_e N'_e(E'_e) dE'_e$  is defined by  $N'_0$ ,  $\alpha$  is the electron spectral index and  $E'_{cut}$  is cut-off energy. Since the blob moves along the jet with a bulk Lorentz factor of  $\Gamma_{bulk}$ , the radiation will be amplified by a relativistic Doppler factor of  $\delta = 1/\Gamma_{bulk}(1 - \beta \cos(\theta_{obs}))$ , where  $\theta_{obs}$  is the angle between the bulk velocity and the line of sight. For 3C 120, the averaged bulk Lorentz factor has been estimated to be  $\Gamma_{bulk} = 5.3 \pm 1.2$  [56, 22], while different mean values for  $\theta_{obs}$  were obtained in VLBI observations;  $\theta_{obs}$  varies from  $9.7^\circ$  [51] to  $20.5^\circ$  [56]. So, we assumed  $\delta = 4$  (e.g.,  $\theta_{obs} \sim [15^\circ - 20^\circ]$ ) and  $\delta \approx 6$  (e.g.,  $\theta_{obs} \sim 9.7^\circ$ ) for the quiescent and flaring states, respectively. In the quiescent state, since no significant  $\gamma$ -ray variability is observed (or it varies in a long period) most likely the emission is produced in a large region for which we assume  $R \approx 4 \times 10^{17} \text{cm} \sim 0.1 \text{pc}$ . Instead, in the active state the fast  $\gamma$ -ray flares in day/sub-day scales indicate that the emitting region size should be  $R/\delta \leq c \times t \times \delta = 1.56 \times 10^{16} (t/1 \text{day}) (\delta/6) \text{cm}$ .

In the flaring state, the inverse Compton scattering of external photons either reflected from the BLR [86] or from the hot dusty torus [19, 32] can contribute to the emission in the  $\gamma$ -ray band. For any reasonable assumption about the jet opening angle ( $\theta = 0.1^\circ$ ) and Doppler boosting factor ( $\delta = 6$ ) the  $\gamma$ -ray emission region is at the distance  $\sim R/\theta \approx 2.3 \text{pc}$  well beyond the radius of BLR  $(5.9 - 7.4) \times 10^{16} \text{cm}$  determined from reverberation mapping [76]. In this case the dominant external photon field is the IR radiation from the hot dusty torus which, as we assume, has a blackbody spectrum with a luminosity of  $L_{IR} = \eta L_{disk}$  ( $\eta = 0.6$ ) [36] and these photons are filling a volume that for simplicity is approximated as a spherical shell with a radius of  $R_{IR} = 3.54 \times 10^{18} (L_{disk}/10^{45})^{0.5} \text{cm}$  [69]. The accretion disk luminosity was estimated using the Swift UVOT data points observed during the flaring periods. Reproducing the UVOT fluxes with the Shakura-Sunyaev disk spectrum [84] fixing the peak energy at  $\sim 10 \text{eV}$ , we obtained that the disk luminosity  $L_{disk} = 1.2 \times 10^{45} \text{erg s}^{-1}$  (see Fig.4.2 black dashed line), which is close to the value obtained in [54].

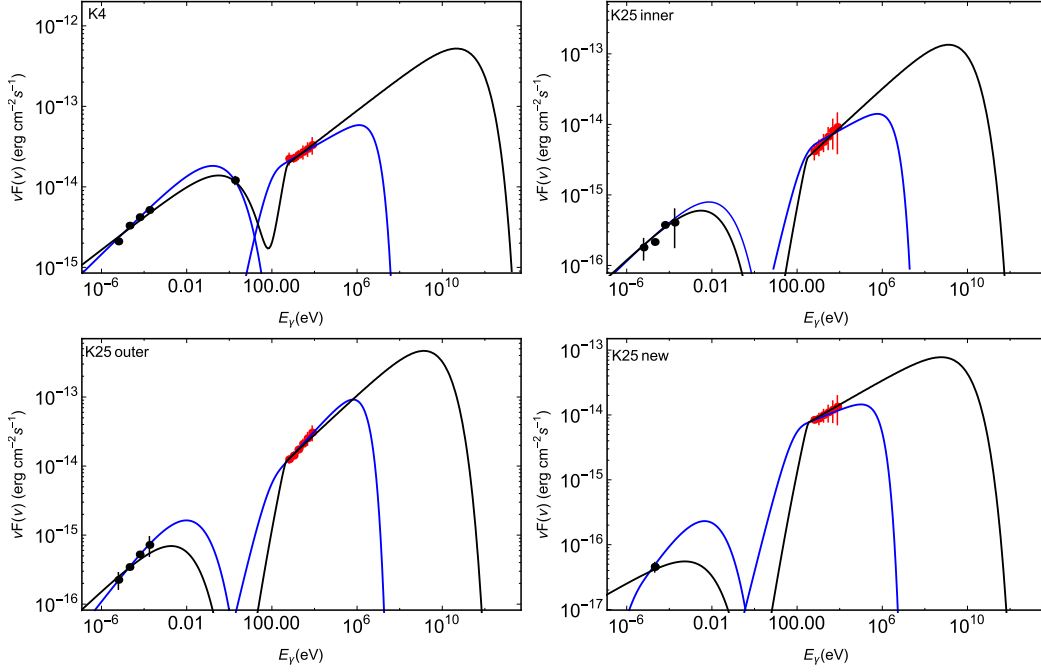


**Figure 4.3:** The SED of knots. The radio-to-optical data (black points) are from previous studies and the X-ray data (red points) are derived in this paper. Black lines are the IC/CMB model calculated for  $\delta = 10$ , and blue lines are the fit by the two-component synchrotron model.

#### 4.4.2 The large-scale jet emission

We assembled the 3C 120 knots' SEDs from the radio to X-ray bands, using the radio-to-optical data from [48] (black points in Fig. 4.3) and the X-ray data obtained in Section 6.3 (red points in Fig. 4.3). The X-ray flux is well above the extrapolation from the radio-to-optical spectra and it hardens; this is more evident for the k25\_new where  $L_X/L_{rad} \simeq 250$ . This confirms the previous findings that two different components are necessary to explain the radio-to-optical and X-ray emission from the knots of 3C 120.

The detected highly polarized emission led to a conclusion that the radio-to-optical emission from the knots is of a synchrotron origin. The radiative mechanism usually considered to explain the origin of the X-ray emission is either the synchrotron emission from a second, much more energetic population of electrons (e.g., [55, 48, 64, 79]) or the inverse Compton scattering on various possible sources of soft photons, including the synchrotron photons (SSC; e.g., [46]) and the cosmic microwave background photons (IC/CMB; e.g., [91]). Most naturally, the X-ray emission could originate from IC scattering of synchrotron photons with a density of  $U_{syn} = L_{radio}/4\pi R_{k4}^2 c \approx 3.2 \times 10^{-14} \text{ erg cm}^{-3}$  where  $L_{radio} \simeq 2.0 \times 10^{40} \text{ erg s}^{-1}$  is the radio luminosity of k4 and  $R_{k4} \approx 0.42 \text{ kpc}$  is the knot size. When comparing the radio and X-ray data it becomes clear that  $L_{SSC} \geq L_{syn}$  ( $U_B \leq U_{syn}$ ) which is satisfied only if  $B \leq 0.8 \mu\text{G}$ , which is in contradiction with the averaged value of  $\geq 10 \mu\text{G}$  usually estimated for the knots. In such a weak magnetic field, the observed radio luminosity can be accounted for only if the particle energy ( $U_e$ ) strongly dominates over the magnetic field thus contravening the equipartition condition. Because of this we only consider (1) the inverse Compton scattering of CMB photons and (2) synchrotron emission from a second, much more energetic population of electrons. In the IC/CMB scenario, it is assumed that the emitting region moves with a relativistic bulk Lorentz factor of  $\Gamma_{bulk}$  in order to predict a larger X-ray luminosity, since in the jet frame the energy density of CMB photons will be enhanced by a factor of  $\Gamma_{bulk}^2$ . The condition of  $L_{X-ray} > L_{radio}$  is satisfied only if  $\delta$  is at least 10. In contrast, if the X-ray emission is produced by synchrotron radiation from a second population of relativistic electrons with very high maximum energy, it is not required to have a highly relativistic jet, and we assume  $\delta = 1$ . Since the electrons with high maximum energy would quickly cool down, most likely they had been produced in a separate episode of acceleration, which occurred more recently. Moreover, the second population of electrons can be produced in

different parts of the knot [e.g., [70, 88]]. We do not go much into details, but assume that there are two different electron populations responsible for the emission.

In the IC/CMB scenario, the underlying electron distribution is given by Eq. 6.3.1 with the cutoff energy allowed to vary only for k4, where the optical flux at  $\sim 10^{14}$  Hz allows to constrain the HE tail of synchrotron emission, while for the other knots it is fixed at  $E_{cut} = 100$  GeV due to the lack of data. In addition, a power-law distribution in the form of  $N_{PL} \sim E_e^{-\alpha_{PL}}$  is added to model the X-ray spectrum in the two-component synchrotron scenario. Since the data are not enough to constrain  $E_{max,PL}$ , an artificial HE limit of  $E_{PL,max} = 1$  PeV has been introduced, whereas  $E_{PL,min}$  is left as a free parameter only ensuring that the flux from the second component does not exceed the first one. In our calculations we used the shapes and sizes of the knots as provided in [48]. To make the deviation from the equipartition condition as less as possible, we define  $\eta = U_e/U_B$ , which is used as a free parameter with  $U_e$  during the fit. This will allow to find the optimum value for  $\eta$  when  $\eta = 1$  does not give satisfactory representation of the data. In the two-component synchrotron model, we fix  $\eta = 1$  and perform fitting of the radio-to-optical data. Then fixing this magnetic field, the X-ray data are fitted with the second component.

### 4.4.3 Fitting technique

In order to constrain the model free parameters we have modified the naima package [95] which derives the best-fit and uncertainty distributions of spectral model parameters through MCMC sampling of their likelihood distributions. The prior likelihood, our prior knowledge of the probability distribution of a given model parameter and the data likelihood functions are passed onto the emcee sampler function for an affine-invariant Markov Chain Monte Carlo run. In the parameter sampling, the following expected ranges are considered:  $1.5 \leq (\alpha, \alpha_{PL}) \leq 10$ ,  $0.511 \text{ MeV} \leq E'_{cut} \leq 1 \text{ TeV}$  and  $N_0$  and  $B$  are defined as positive parameters. The synchrotron emission is calculated using the parameterization of the emissivity function of synchrotron radiation in random magnetic fields presented in [13] while the IC emission is computed based on the monochromatic differential cross section of [12].

**Table 4.3:** The parameters derived from the modeling of the knots SEDs.

| Parameter                                 | k4   | k25 inner   | k25 outer  | k25 new   |
|---|--|---|--|---|
| $U'_e(U_e)[erg\ cm^{-3}] \times 10^{-12}$ | $111.8^{+16.49}_{-9.91}(531.52^{+110.7}_{-84.76})$ | $20.65^{+9.95}_{-3.47}(102.91^{+82.45}_{-45.22})$ | $30.25^{+6.21}_{-2.73}(48.56^{+26.11}_{-13.47})$ | $7.43^{+2.89}_{-1.43}(4.09^{+1.27}_{-0.63})$          |
| $\alpha$                                  | $2.59 \pm 0.03(2.48 \pm 0.06)$                     | $2.44 \pm 0.1(2.41^{+0.22}_{-0.26})$              | $2.42 \pm 0.04(2.20^{+0.17}_{-0.15})$            | $2.62^{+0.14}_{-0.10}(2)$                             |
| $E'_{min}(E_{min})[MeV]$                  | $24.01^{+3.62}_{-5.44}(4.40^{+2.92}_{-2.31})$      | $18.2 \pm 10.6(3.39^{+3.57}_{-1.90})$             | $22.23^{+5.53}_{-8.43}(4.04^{+8.48}_{-2.92})$    | $19.1^{+7.11}_{-8.57}(1445.67^{+3852.81}_{-1198.91})$ |
| $B'(B)[\mu G]$                            | $5.61(115.6)$                                      | $2.35(50.85)$                                     | $1.36(34.94)$                                    | $0.93(10.14)$   |
| $\eta$                                    | $89.39^{+7.48}_{-12.75}$                           | $94.04^{+49.8}_{-43.7}$                           | $410.86^{+64.28}_{-104.94}$                      | $214.3^{+162.67}_{-124.63}$                           |
| $U_{e,p}(erg\ cm^{-3}) \times 10^{-14}$   | $6.01^{+5.85}_{-2.38}$                             | $2.36^{+2.59}_{-1.19}$                            | $7.22^{+3.01}_{-1.93}$                           | $13.22^{+15.7}_{-5.62}$                               |
| $\alpha_p$                                | $2.69^{+0.22}_{-0.18}$                             | $2.66^{+1.15}_{-0.54}$                            | $2.32^{+0.17}_{-0.18}$                           | $2.73^{+0.29}_{-0.24}$                                |
| $E_{min,p}[TeV]$                          | $2.83^{+3.22}_{-1.73}$                             | $6.89^{+9.83}_{-5.17}$                            | $5.31^{+5.65}_{-3.16}$                           | $8.88^{+10.24}_{-6.78}$                               |
| $L_B \times 10^{42}$                      | $6.48(128)$  | $71.26(333.7)$                                    | $31.98(211)$                                     | $0.67(3.69)$  |
| $L_e \times 10^{44}$                      | $5.81(1.28)$                                       | $66.98(3.34)$                                     | $131.45(2.11)$                                   | $1.44(0.04)$  |

## 4.5 Results and discussion

In this paper, the multiwavelength emission from the 3C 120 core is investigated using the Swift XRT/UVOT and Fermi LAT data. Quiescent and flaring states are identified and their modeling allowed to investigate the jet properties and physical processes that take place in the core where, most likely, the jet is formed. On the other hand, the jet properties are also estimated at large distances from the core using the Chandra X-ray data.

The adaptively binned  $\gamma$ -ray light curve showed that before MJD 56900 and after MJD 57300, the source was in a quiescent state characterized by a relatively faint  $\gamma$ -ray emission with the flux and the photon index consistent with the previously reported values. Then, from MJD 56900 to MJD 57300, most of the time, the source was in an effective  $\gamma$ -ray emitting state with rapid  $\gamma$ -ray flares. During the bright periods, the  $\gamma$ -ray photon index hardened and corresponds to  $\approx 2.3$  and  $\approx 2.0$ . Two strong events with  $(7.46 \pm 1.56) \times 10^{-6}$   $photon\ cm^{-2}\ s^{-1}$  and  $(4.71 \pm 0.92) \times 10^{-6}$   $photon\ cm^{-2}\ s^{-1}$  within accordingly 19.0 min and 3.15 hours were detected on April 24, 2015, which are the highest fluxes detected so far from 3C 120. At a distance of 144.9 Mpc, these correspond to an isotropic  $\gamma$ -ray luminosity of  $(1.20 - 1.66) \times 10^{46}$   $erg\ s^{-1}$ . The same value estimated for the quiescent state (the first bin in Fig. 6.2 red data) is  $2.85 \times 10^{43}$   $erg\ s^{-1}$ . Yet, assuming  $\delta = 6$ , the total power emitted in the  $\gamma$ -ray band in the proper frame of the jet would be  $L_{em,\gamma} = L_\gamma/2\ \delta^2 = (1.67 - 2.31) \times 10^{44}$   $erg\ s^{-1}$  during the peak flux and  $L_{em,\gamma} = 8.9 \times 10^{41}$   $erg\ s^{-1}$  in a quiescent state (assuming  $\delta = 4$ ). Thus, during

the peak emission, the energy released in the  $\gamma$ -ray band corresponds to large fraction of Eddington luminosity ( $L_{Edd} = 6.5 \times 10^{45} \text{ erg s}^{-1}$  for the black hole mass of  $5.5 \times 10^7 M_{\odot}$  [73]) while it is a small fraction ( $\sim 1.4 \times 10^{-4}$ ) in the quiescent state.

Usually the radio galaxies have a luminosity of  $\leq 10^{44} \text{ erg s}^{-1}$  [4, 8], and the peak  $\gamma$ -ray apparent luminosity of  $(1.20 - 1.66) \times 10^{46} \text{ erg s}^{-1}$  is unusual, more characteristic for BL Lac objects. Such a strong  $\gamma$ -ray output observed from 3C 120 is not surprising as the jet inclination angle is relatively small as compared with other radio galaxies.

In the X-ray band, the average flux in the 0.5-10.0 keV range is around  $(2.4 - 4.3) \times 10^{-11} \text{ erg cm}^{-2} \text{ s}^{-1}$  in the quiet state and  $(5.4 - 6.7) \times 10^{-11} \text{ erg cm}^{-2} \text{ s}^{-1}$  in October 4-7, 2014 (active state). When the lowest and highest fluxes from Table 4.1 are compared, a nearly 2.8 times increase of the X-ray flux is found, but its amplitude is lower as compared with the substantial increase in the  $\gamma$ -ray band. During the considered periods, the source spectra were always hard,  $\Gamma_X < 2.0$ . At bright  $\gamma$ -ray flares, the X-ray photon index softened (1.72 – 1.80) as compared with the hard photon index of 1.42 – 1.53 in a quiescent state. The small change in the X-ray flux level and the photon index softening might indicate that different mechanisms are contributing to the acceleration and/or cooling of electrons which modifies the power-law index and the minimum energy of underlying electrons.

The data accumulated during several observations of 3C 120 allowed to resolve and study the X-ray emission from the large-scale jet of 3C 120. In particular, the counts from k4 and k25 are high enough for detailed spectral analysis, resulting in a flux of  $\leq 1.60 \times 10^{-13} \text{ erg cm}^{-2} \text{ s}^{-1}$  with hard X-ray photon indices  $\leq 1.8$  which imply that most of the energy is released above 10 keV. It is interesting to note that the X-ray flux of  $(1.22 \pm 0.19) \times 10^{-13} \text{ erg cm}^{-2} \text{ s}^{-1}$  from k25 outer located at  $\sim 16$  kpc from the core is of the order of the flux from the nearby k4 at  $\sim 2.5$  kpc however with a much harder,  $\Gamma_X = 1.62 \pm 0.11$ , X-ray photon index.

#### 4.5.1 The origin of emission from the inner Jet

The broadband emission modeling results obtained in the quiescent and flaring states are shown in Fig. 4.2 with the corresponding parameters in Table 6.2. In the quiescent state, the X-ray spectra have different photon indices,  $\Gamma_X = 1.42 \pm 0.07$  and  $1.53 \pm 0.08$ , this is why both spectra have been consid-

ered during the fit. In the fit we also included the archival radio data from the observations in the period when the source was in the quiescent state. The radio emission can be produced from the low-energy electrons which are accumulated for longer periods, so the the radio flux should not exceed the presented limit. When both radio and optical/UV data are considered, in order to have model which predicts emission below the radio flux, a larger value of  $E'_{min}$  is required. However, the increase of  $E'_{min}$  would also affect the flux predicted by SSC in the X-ray band; for example, the blue dashed line in Fig. 4.2 illustrates the model for  $E'_{min} \simeq 354.51 \pm 25.91$  MeV (summing the errors in quadrature), beyond which the model predicts either a high radio flux or a low X-ray flux. The magnetic field is  $B = 0.16$  G with an energy density of  $U_B = 1.07 \times 10^{-3} \text{ erg cm}^{-3}$ , slightly higher than that of the electrons,  $U_e = 1.02 \times 10^{-3} \text{ erg cm}^{-3}$ . This magnetic field energy density should be considered as an upper limit, since the Swift UVOT data may represent the direct thermal disc emission, so, in principle, the synchrotron component can be much lower. Thus, in the second modeling, we assume that the low-energy component is only defined by the radio data (blue and red solid lines in Fig. 4.2). In this case the underlying electron distribution is characterized by a harder power-law index ( $\alpha = 2.22 \pm 0.19$  and  $\alpha = 1.85 \pm 0.27$  for blue and red solid lines respectively) and higher cut-off energy  $E'_{cut} = 4.61 \pm 1.27$ . The magnetic field is significantly lower,  $B = 2.3 \times 10^{-3}$  G, and the jet should be strongly particle-dominated to have the peak flux of the HE component exceeding that of the low energy one. This particle dominance can be minimized assuming that the X-ray emission is of a different origin (e.g., from another blob or from thermal Comptonization near the disk). When the optical/UV and X-ray data are assumed as upper limits in the fit, a lower flux from SSC emission is expected (gray line in Fig. 4.2 [left panel]) and now  $U_e/U_B \approx 43$ .

When the SED in the flaring period is modeled considering SSC emission (red solid line in Fig. 4.2 [right panel]) the electron distribution as well as the magnetic field should vary. As the X-ray spectrum is soft ( $\Gamma_X = 1.8$ ), the modeling yielded a lower  $E'_{min} = (67.57 \pm 19.38)$  MeV and  $\alpha \simeq 2.79 \pm 0.15$ . As the  $\gamma$ -ray spectrum is shifted to higher energies, then  $E'_{cut} = (6.32 \pm 2.32)$  GeV cutoff is required. Since the emitting region radius decreases  $\sim 25.6$  times, in order to produce a synchrotron flux of the same order (or higher), the magnetic field should increase ( $0.86 \pm 0.1$  G), because the synchrotron emission depends on the total number of the emitting electrons  $N_e$ ,  $\delta$  and magnetic field  $B$ . In this case, the required electron energy density exceeds that of the magnetic field

only 2.6 times, meaning there is no significant deviation from equipartition. The radio data are also plotted as reference values, but we note that in the flaring state the radio flux can also increase. However, the model does not predict a flux that significantly exceeds the observed radio data.

In the right panel of Fig. 4.2, SSC (blue dashed) and EIC (blue dot dashed) modeling of the SED is shown (blue solid line corresponds to SSC+EIC). The X-ray emission can be explained by the SSC emission produced in a blob of the size similar to that emitting in a quiescent state, but additional changes in  $\alpha$ ,  $E'_{cut}$  and  $B$  are necessary to account for the new X-ray spectrum. Whereas the  $\gamma$ -ray emission is entirely due to the IC scattering of external photons in the fast and compact blob which is strongly particle-dominated with  $U_e/U_B \approx 519$  and the magnetic field  $B = 0.11 \pm 0.1$  G which does not differ much from the values obtained in the one-zone models. In the radio band, the modeling predicts a higher flux as compared with the presented radio data. As the radio data are not from the source active periods, this is not a strong argument to disfavor such modeling. When a larger value for  $E'_{min}$  is used in the modeling, it does not introduce significant changes in the model parameters (especially in the energetics of the jet). Even if the data are not sufficient for the estimation of the parameters with a high significance, so the conclusions are not definite, this is an interesting modeling, as it could possibility explain the rapid  $\gamma$ -ray activities. Such blob can be naturally formed in the reconnection events that could produce compact regions of rapidly moving plasma inside the jet ("jet in jet scenario", [40, 41]).

### 4.5.2 The origin of emission from knots

The black lines in Fig. 4.3 represents the IC/CMB radiation model calculated for  $\delta = 10$ . The obtained parameters are presented in Table 4.3. Similar photon indices observed in the radio and X-ray bands allowed to well define the power-law index of electrons which varies from 2.4 to 2.6. The cut-off energy estimated for k4 is  $E'_c \approx (916.3 \pm 251.4)$  GeV implies there is an effective particle acceleration above the TeV energies.  $E'_{min} \simeq (18.20 - 24.01)$  MeV is estimated, which we obtain by requiring a turnover below the X-ray data in order to not overproduce the radio/optical flux but in principle lower values cannot be excluded. The IC scattering of CMB photons with  $u_{CMB} \simeq 4.0 \times 10^{-11} \text{ erg cm}^{-3}$  density (when  $\delta = 10$ ) still predicts a flux lower than the observed one, so we were forced to adopt larger values of  $\eta$ . We found

that when  $B = (0.93 - 5.6) \mu\text{G}$  and  $\eta = (83.4 - 410.8)$ , the IC/CMB model can reproduce the observed spectra. The maximum electron energy density is estimated to be  $1.12 \times 10^{-10} \text{ erg cm}^{-3}$  for the k4, while for the other knots it is  $> 4$  times lower. This is natural, since even if the total number of particles is conserved, the low-energy cutoff moves to lower energies (because of adiabatic losses), the normalization decreases and  $U_e$  does so as well. The IC/CMB component predicts emission up to  $\sim \epsilon_{\text{CMB}}(E_e/m_e c^2)^2 \approx 27.4 \text{ GeV}$  so that  $\gamma$ -ray emission is also expected. However, even if the predicted flux is above the Fermi LAT sensitivity ( $\sim 10^{-13} \text{ erg cm}^{-2} \text{ s}^{-1}$ ), its level (a few times  $10^{-13} \text{ erg cm}^{-2} \text{ s}^{-1}$ ) would be still below the core emission in the quiet state (Fig. 4.2). Moreover, the Doppler boosting of  $\delta \geq 10$  requires the jet to be highly relativistic or viewed at small angles at kpc distances from the core which seems unrealistic for 3C 120, so even lower flux levels are expected.

The blue lines in Fig. 4.3 show the two-component synchrotron model fitting of knots' SEDs. The radio-to-optical data of the four knots are modeled with synchrotron emission with the following plausible parameters:  $B$  between 10.1 and 115.6  $\mu\text{G}$  and an electron power-law index of  $\alpha = 2.20 - 2.48$ . The plasma in the knots is in equipartition,  $U_e = U_B = (4.1 - 531.5) \times 10^{-12} \text{ erg cm}^{-3}$ , which requires more than 10 times stronger magnetic field for all the knots, as compared with the previous modeling. The synchrotron emission of the second population of electrons for the same magnetic field can explain the X-ray flux when  $E_{\text{min}} \simeq (2.83 - 8.88) \text{ TeV}$  and  $\alpha = 2.32 - 2.69$ . The particle energy density of this component is negligible as compared with the other one. A significant contribution from the electrons with  $E_e \simeq 10 \text{ TeV}$  is expected, the cooling time of which  $t_{\text{cool}} = 6 \pi m_e^2 c^3 / \sigma_T B^2 E_e \simeq 255.75 \text{ yr}$ . This corresponds to a travel distance of  $c \times t_{\text{cool}} \simeq 78.4 \text{ pc}$ , which is much smaller than the size of the knots. Thus, it is required that the particle acceleration in situ over the entire volume of the knots should be extremely efficient. The above obtained parameters were estimated taking into account the equipartition condition, when the system is close to internal pressure or energy density condition. But for jet dynamics and propagation more important is the jet pressure balance with the ambient medium. The results presented here and previous observations of the knots allow to put important constraints on some of the physical parameters of the jet. The jet half opening angle ( $\theta_j$ ) at kpc scale can be estimated using the first resolved jet knot (k4); at a distance of 4 arcseconds from the core its radius is 0.738 arcsecond, implying  $\theta_j \simeq 10.45^\circ$ . Having the independent information on the jet Doppler factor, the upper bound on the magneto sonic (Mach) number is  $M_j \sim 1/\tan(\theta_j) \Gamma_{\text{bulk}} \simeq$

$5.42/\Gamma_{bulk}$ . If the jet remains relativistic up to kpc scale with  $\Gamma_{bulk} = 5.3 \pm 1.2$ ,  $M_j \simeq 1.02$ . For the pc jet of 3C 120, assuming an  $R = 1.56 \times 10^{16}$  cm emitting region at parsec distance,  $M_j$  corresponds to 37.32. Thus, the relativistic jet with an initial high Mach number comes into static pressure equilibrium with the interstellar medium of the parent galaxy, starting to interact with it, causing the Mach number to decrease. This is qualitatively supported by the radio/X-ray observations, which reveal that at the distance of after k4/k7 knots the jet starts to expand (e.g., Fig. 3 of [48]).

### 4.5.3 Jet energetics

The fundamental quantity is the total power (particles + magnetic field) transported by the jet flow. The total jet power can be estimated using the parameters derived from the SEDs modeling by  $L_e = \pi c R_b^2 \Gamma^2 U_e$  and  $L_B = \pi c R_b^2 \Gamma^2 U_B$  [23] for electrons and magnetic field, respectively ( $\Gamma = 1$  is assumed in the two-component synchrotron model). The protons with unknown contribution to the jet have not been considered in the calculations, since a number of assumptions need to be made.

In the quiescent state, the total power at the jet core for all models presented in Fig. 4.2 is  $L_{jet} = L_e + L_B \simeq (2.35 - 48.0) \times 10^{44}$  erg s<sup>-1</sup> (like in [89, 54, 81]). Thus, the isotropic  $\gamma$ -ray luminosity,  $L_{em,\gamma} \simeq 8.2 \times 10^{41}$  erg s<sup>-1</sup>, is only the small fraction of the total jet power. The jet's total power,  $L_{jet} \simeq 1.31 \times 10^{44}$  erg s<sup>-1</sup>, decreases in the active state, since it scales with the emitting region size ( $L_{jet} \sim R^2 U$ ) and a smaller region is considered. However, this region is more energetic, as the particle energy density is  $\sim 146.9$  times higher than that in the quiet state. The SSC+EIC scenario requires a total jet luminosity of  $L_{jet} \simeq 4.14 \times 10^{45}$  erg s<sup>-1</sup>, which is higher than the previous values, but is well achievable for the black hole mass in 3C 120.

When the jet power is estimated for the knots, their largest reasonable volumes are used, so that the obtained values are the upper limits. In case of the beamed IC/CMB scenario the total jet power should be  $L_{jet} \simeq (1.4 - 131.4) \times 10^{44}$  erg s<sup>-1</sup> in order to explain the X-ray luminosity of  $L_X \simeq (1.0 - 4.0) \times 10^{41}$  erg s<sup>-1</sup>. This jet luminosity is mostly defined by the kinetic energy of particles since the modeling reveals a moderate domination of particles over the magnetic field ( $\eta \gg 1$ ). In the two-component synchrotron model, the total jet luminosity is lower,  $L_{jet} \leq 6.7 \times 10^{44}$  erg s<sup>-1</sup>, where the contribution of the X-ray emitting component is negligible. The powers independently derived

for the inner and outer regions of the jet are of the same order, suggesting that the jet does not substantially dissipate its power until its end but it becomes radiatively inefficient farther from the formation point.

## 4.6 Summary

The main properties of the powerful jet of 3C 120 are investigated by comparing the physical state of the plasma on sub-pc and kpc scales. The main processes responsible for the broadband emission in the innermost ( $\leq$  pc; Swift XRT/UVOT and Fermi LAT data) and outer ( $\geq$  1 kpc; Chandra data) regions are also studied.

On April 24, 2015, a rapid and dramatic increase of the  $\gamma$ -ray flux was observed from the inner jet of 3C 120. Within 19.0 min and 3.15 hours the flux was as high as  $(7.46 \pm 1.56) \times 10^{-6}$  *photon cm<sup>-2</sup> s<sup>-1</sup>* and  $(4.71 \pm 0.92) \times 10^{-6}$  *photon cm<sup>-2</sup> s<sup>-1</sup>* above 100 MeV which corresponds to an isotropic  $\gamma$ -ray luminosity of  $(1.2 - 1.6) \times 10^{46}$  *erg s<sup>-1</sup>*. Such luminosity is unusual for radio galaxies and more typical for BL Lacs. The synchrotron/SSC mechanism gives a reasonable explanation of the multiwavelength SED in the quiescent and flaring states. The increase and rapid changes in the flaring state can be also explained assuming an additional contribution from the blob where the dominant photon fields are of external origin. The necessary jet kinetic power is  $L_{jet} \simeq (1.31 - 48.0) \times 10^{44}$  *erg s<sup>-1</sup>*.

The X-ray emission from the knots has a hard photon index of  $\simeq (1.6 - 1.8)$  with a luminosity of  $L_X \simeq (1.0 - 4.01) \times 10^{41}$  *erg s<sup>-1</sup>*. This X-ray emission can be explained by IC/CMB models only if  $\delta > 10$ , otherwise the particle energy density will strongly dominate over that of the magnetic field. If the X-rays are produced from the direct synchrotron radiation of the second population of electrons, which are produced more recently than the cooler population responsible for the radio-to-optical spectrum, lower jet luminosity and no bulk relativistic motion on kpc scales is required.

The jet luminosities of the innermost and outer regions are comparable, suggesting that the jet does not suffer important energy losses from the regions close to the black hole to those at hundreds of kiloparsecs from it. However, at larger distances the magnetic field and the particle energy density decrease and the jet becomes radiatively inefficient.

# 5 Rapid Gamma-ray variability of NGC 1275

## 5.1 Introduction

Due to its proximity ( $z = 0.0176$ ,  $\approx 75.6$  Mpc) and brightness, the radio galaxy NGC 1275 has been a target for observations in almost all energy bands. Core-dominated asymmetrical jets at both kpc [38] and pc scales [12] have been detected in the radio band with characteristics more similar to those of Fanaroff and Riley type 1 sources [21]. The emission in the X-ray band is mostly dominated by the thermal emission from the cluster, although a nonthermal component in the energy range 0.5-10 keV with a photon index of  $\Gamma_X \simeq 1.65$  has been observed [19, 20]. High Energy (HE;  $> 100$  MeV)  $\gamma$ -rays from NGC 1275 had already been detected by Fermi Large Area Telescope (*Fermi*) using the data obtained during the first 4 months of observations [2]. Then, using the data accumulated for longer periods  $\gamma$ -ray flux and photon index variation on month timescales were detected [28]. However, the  $\gamma$ -ray emission is variable also in shorter (a few days?) timescales [17]. Very High Energy (VHE;  $> 100$  GeV)  $\gamma$ -ray emission with a steep spectral index of  $4.1 \pm 0.7$  was detected by MAGIC, using the data accumulated between August 2010 and February 2011 [8]. No hints of variability above 100 GeV were seen on month time scales.

Even if the observed  $\gamma$ -ray variability allowed to exclude Perseus cluster as the main source of  $\gamma$ -ray emission, the exact mechanisms responsible for the broadband emission from NGC 1275 are still unclear. The multiwavelength Spectral Energy Distribution (SED) hints at a double-peaked SED with the peaks around  $10^{14}$  Hz and  $(10^{23} - 10^{24})$  Hz [10]. Within a "classical" misaligned BL Lac scenario, a one-zone synchrotron/Synchrotron Self Compton (SSC) interpretation of the SED can well explain the HE peak constrained by *Fermi* and MAGIC data but has difficulties explaining the low energy data. It requires that the jet should be more aligned than it is estimated, e.g.,  $30^\circ - 55^\circ$

**Table 5.1:** Parameters of spectral analysis

| <i>Fermi</i>      |                 |                   |                           |                              |                                    |
|-------------------|-----------------|-------------------|---------------------------|------------------------------|------------------------------------|
| Period            | Date            | Flux <sup>a</sup> | Photon Index <sup>b</sup> | Test Statistic               | Highest photon energy <sup>c</sup> |
| 57442.32-57444.45 | 2016/02 (24–26) | 4.18 ± 0.85       | 1.93 ± 0.14               | 123                          | 10.39                              |
| 57752.75-57753.25 | 2016/12 (30–31) | 8.56 ± 2.30       | 1.79 ± 0.17               | 106                          | 34.77                              |
| 57753.81          | 2016/12 31      | 34.82 ± 8.67      | 1.93 ± 0.19               | 102                          | 5.84                               |
| 57754.00-57755.75 | 2017/01 (01–02) | 6.27 ± 1.20       | 1.67 ± 0.11               | 178                          | 4.18                               |
| Swift-XRT         |                 |                   |                           |                              |                                    |
| Obsid             | Date            | Exp. time         | Photon Index <sup>d</sup> | Unabsorbed Flux <sup>e</sup> | $\chi^2_{red}$ (d.o.f.)            |
| 34380005          | 2016-02-25      | 2750              | 1.52 ± 0.08               | 3.10 ± 0.19                  | 1.04 (75)                          |
| 87312001          | 2016-12-30      | 939               | 1.75 ± 0.12               | 8.64 ± 0.76                  | 0.74 (24)                          |
| 87311001          | 2017-01-01      | 619               | 1.77 ± 0.17               | 10.57 ± 1.26                 | 1.15 (15)                          |
| 31770011          | 2017-01-01      | 984               | 1.77 ± 0.08               | 10.29 ± 0.55                 | 0.95 (173)                         |

Notes: a: Integrated  $\gamma$ -ray flux in the 0.1 – 100 GeV energy range in units of  $10^{-7}$   $photon\ cm^{-2}\ s^{-1}$ .  
b:  $\gamma$ -ray photon index from likelihood analysis. c: Photon energy in GeV. d: Photon index from X-ray data analysis. e: X-ray flux in the energy range 0.3–10 keV in units of  $\times 10^{-11}$   $erg\ cm^{-2}\ s^{-1}$  (corrected for the Galactic absorption).

[48]. Therefore additional assumptions on the jet properties and/or more complex scenarios for inverse-Compton scattering should be made.

In the HE  $\gamma$ -ray band frequently flaring activities are known for NGC 1275 [14]. A substantial increase of the  $\gamma$ -ray flux in the HE and VHE  $\gamma$ -ray bands was detected in October 2015 and January 2017 [39, 35, 36, 33]. In October 25, 2015 *Fermi* detected a bright flare with a daily peak flux of  $(1.6 \pm 0.2) \times 10^{-6}$   $photon\ cm^{-2}\ s^{-1}$  [39]. Then, in the night between 31 December 2016 and 01 January 2017 a major flare was detected in the VHE  $\gamma$ -ray band when the flux was 60 times higher than the mean flux [35]. Also the flux  $> 100$  MeV was about 12 times higher than the most significant flux observed with AGILE [33]. Besides, Swift observations during this major  $\gamma$ -ray active period provided data in the UV and X-ray bands and so giving a unique chance to investigate the flaring activity of NGC 1275 in the multiwavelength context. The goal of this paper is to have a new look on the  $\gamma$ -ray emission from NGC 1275 in the last  $\sim 8.7$  years in general and during the major flaring periods in particular. The larger data set allows to investigate the  $\gamma$ -ray flux evolution in time with improved statistics in shorter time scales, while a detailed analysis of recently observed exceptional flares will allow to have an insight into the particle acceleration and emission processes.

This paper is organized as follows. The *Fermi* data reduction and temporal analyses are presented in Section 6.2. The spectral analyses of *Fermi* and Swift data are described in Section 6.3. We present our results and discussion in Section 6.4. Summary is given in Section 5.5.

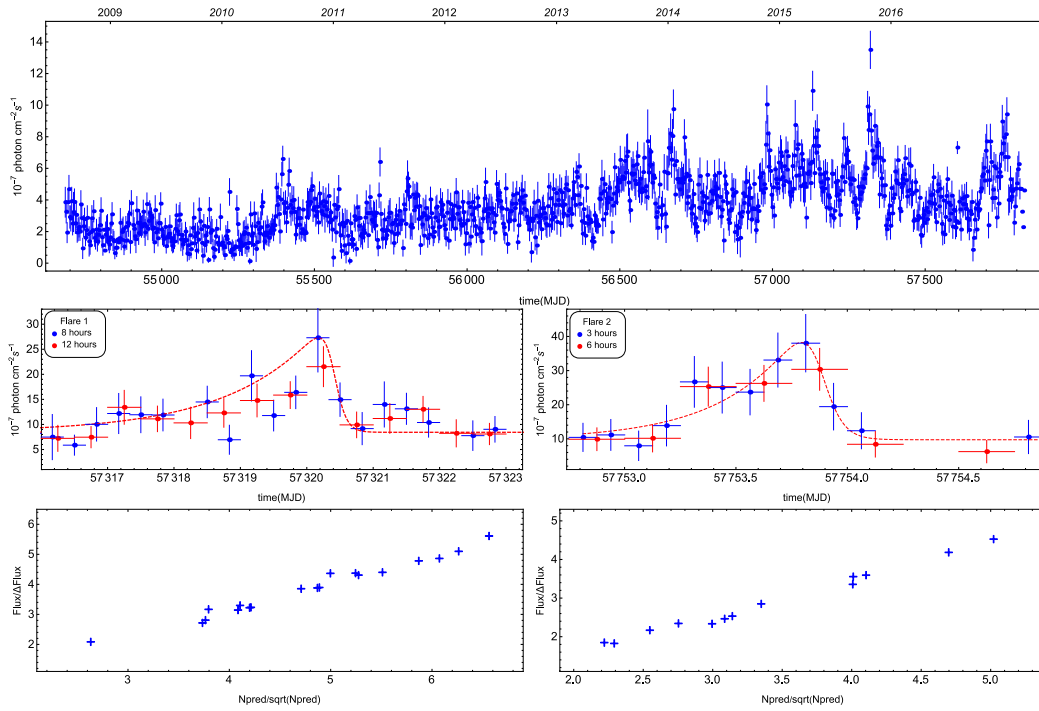


**Figure 5.1:** Top panel: The light curve of  $0.1 < E_\gamma < 500$  GeV  $\gamma$ -rays from NGC 1275 from August 4, 2008 to March 5, 2017, with 3-day (blue) binning. Middle panels: Sub intervals covering F1 (left) and F2 (right). F1 is shown with 8-hour (blue) and 12-hour (red) time intervals and F2 with 3-hour (blue) and 6-hour (red) bins. The red dashed lines show the fit of F1 and F2 with Eq. 6.2.1. Lower panels: The plot of  $N_{\text{pred}}/\sqrt{N_{\text{pred}}}$  vs  $\text{Flux}/\Delta\text{Flux}$  for 8-hour (left) and 3-hour (right) bins.

## 5.2 FERMI LAT OBSERVATIONS AND DATA ANALYSIS

The Large Area Telescope on board the Fermi satellite is a pair-conversion telescope sensitive to  $\gamma$ -rays in the energy range of 20 MeV - 500 GeV [13]. We have used the publicly available data accumulated during the last  $\sim$  8.7 years of *Fermi* operation (from August 4, 2008 to March 15, 2017). The data were analyzed with the standard Fermi Science Tools v10r0p5 software package released on May 18, 2015. The most recent reprocessed PASS 8 events and spacecraft data were used with P8R2\_SOURCE\_V6 instrument response function. Only the events with a higher probability of being photons (ev-class=128, evtype=3) in the energy range of 100 MeV - 500 GeV were analyzed. In the analysis we selected different radii ( $9^\circ$ ,  $10^\circ$ ,  $12^\circ$  and  $15^\circ$ ) of the Region of Interest (ROI) to ensure that the selected ROI is an accurate representation of the observation. This yielded essentially the same results within statistical uncertainties, so a radius of  $12^\circ$  was used and the photons from a  $16.9^\circ \times 16.9^\circ$  square region centered at the location of NGC 1275, (RA,dec)= (49.96, 41.51), were downloaded. The recommended quality cuts, (DATA\_QUAL==1)&&(LAT\_CONFIG==1) and a zenith angle cut at  $90^\circ$  to eliminate the Earth limb events were applied with gtselect and gtmktime tools. We binned photons with gtbins tool with an Aitoff projection into pixels of  $0.1^\circ \times 0.1^\circ$  and into 37 equal logarithmically-spaced energy bins. Then with the help of gtlike tool, a standard binned maximum likelihood analysis is performed. The fitting model includes diffuse emission components and  $\gamma$ -ray sources within ROI. The model file is created based on the *Fermi* third source catalog (3FGL) [6] and the Galactic background component is modeled using the Fermi LAT standard diffuse background model gll\_iem\_v06 and iso\_P8R2\_SOURCE\_V6\_v06 for the isotropic  $\gamma$ -ray background. The normalization of background models as well as fluxes and spectral indices of sources within  $12^\circ$  are left as free parameters. As in 3 FGL, the  $\gamma$ -ray spectrum of NGC 1275 was modeled using a log-parabolic spectrum.

Using of the data accumulated for an almost 2 times longer period than in 3 FGL, can result in new  $\gamma$ -ray sources in the ROI which are not properly accounted for in the model file. In order to probe for additional sources, a Test Statistics map of the ROI (TS defined as  $TS = 2(\log L - \log L_0)$ , where  $L$  and  $L_0$  are the likelihoods when the source is included or is not) is created with gttsmmap tool using the best-fit model of 0.1-500 GeV events. To identify the

coordinates of the excess hot spots with  $TS > 25$  ( $5\sigma$ ) we used the `find_source` iterative source-finding algorithm implemented in `Fermipy`<sup>1</sup>. In the TS map it identifies the peaks with  $TS > 25$  and adds a source at each peak starting from the highest TS peak. The sources position is obtained by fitting a 2D parabola to the log-likelihood surface around the maximum. Alternatively, the sources position was calculated by hand using the pixels surrounding the highest TS (similar to the method used in [34]). Both methods resulted in similar values. For each given point we sequentially added a new point source with a conventional spectral definition (power-law) and performed binned likelihood analysis with `gtlike`. For the further analysis we used the model file with the new additional point-like sources to have better representation of the data.

### 5.2.1 Temporal variability

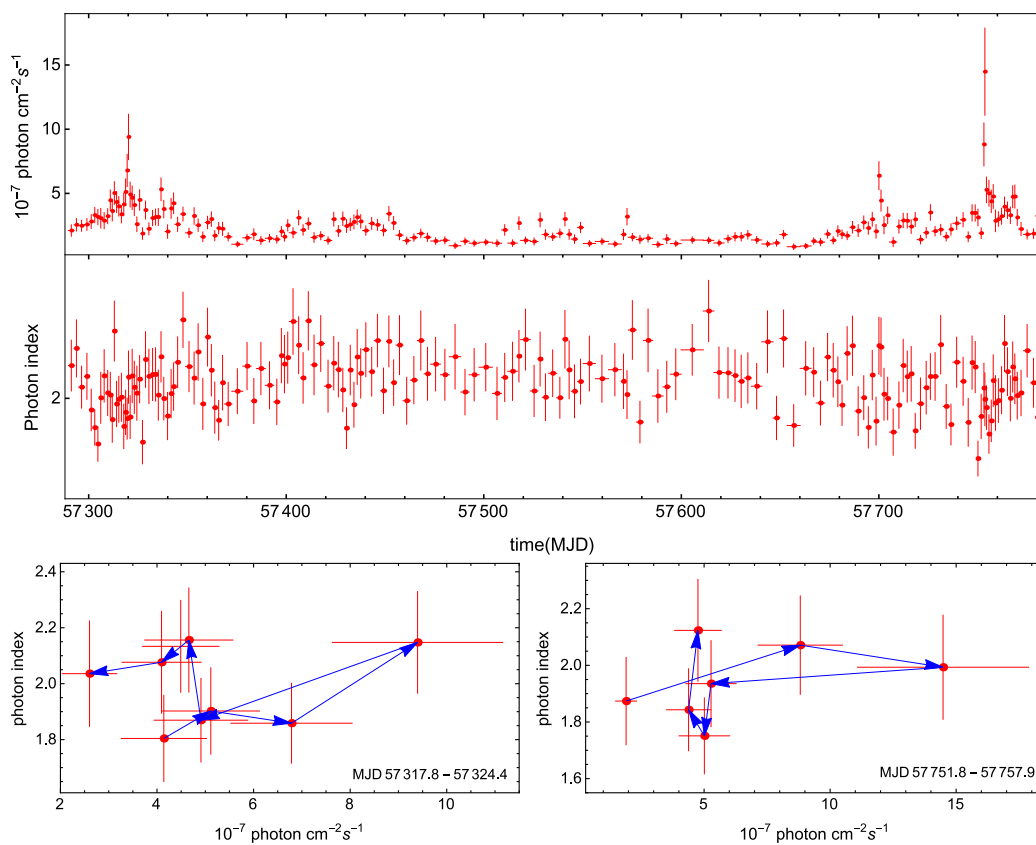
The  $\gamma$ -ray light curve is calculated using the unbinned likelihood analysis method implemented in the `gtlike` tool. (0.1 – 500) GeV photons are used in the analysis with the appropriate quality cuts applied in the previous section. Different model files are used to ensure that the possible contribution from sources within ROI are properly accounted for. In the model file obtained from the whole-time analysis, the photon indices of all background sources are first fixed to the best guess values in order to reduce the uncertainties in the flux estimations, then those of the sources within ROI are considered as free parameters. In addition we analyzed the data accumulated during the one-month periods covering the major flares (01-30 October and 15 December 2016-15 January 2017). Then we fixed the spectral parameters of all background sources as in [7]. All approaches yielded essentially the same results. We used the latter model as the rising and decaying times of the first flare can be evaluated better. Given shorter periods are considered, the spectrum of NGC 1275 has been modeled using a power-law function with the index and normalization as free parameters. Since no variability is expected for the background diffuse emission, the normalization of both background components is also fixed to the values obtained for the whole time period.

Fig. 6.2 (upper panel) shows the  $\gamma$ -ray light curve with three-day bin size. Despite the fact that the flux sometimes exceeded the averaged value presented in 3FGL ( $\approx 2.26 \times 10^{-7} \text{ photons cm}^{-2} \text{ s}^{-1}$ ), pronounced flaring activ-

<sup>1</sup><http://fermipy.readthedocs.io/en/latest/>

ities were detected in October 2015 (hereafter Flare 1 [F1]) and in December 2016/January 2017 (hereafter Flare 2 [F2]). Starting from 22 October 2015 the daily averaged flux of NGC 1275 was above  $10^{-6}$  photons  $cm^{-2} s^{-1}$  and remained high for 5 days with a daily averaged maximum of  $(1.48 \pm 0.20) \times 10^{-6}$  photons  $cm^{-2} s^{-1}$  observed on 24 October 2015. Another substantial increase in the  $\gamma$ -ray flux was observed on December 31, 2016 when the flux increased from about  $(4 \sim 5) \times 10^{-7}$  photons  $cm^{-2} s^{-1}$  to  $(2.21 \pm 0.26) \times 10^{-6}$  photons  $cm^{-2} s^{-1}$  within a day with a detection significance of  $\sim 21.5\sigma$ . The photon statistics allowed us to study these flares with denser time sampling (sub-day) for the first time. The shortest bin sizes have been chosen to ensure that i) the flare rise and decay periods are well constrained and ii) the detection significance for each bin exceeds the  $\sim 5\sigma$  limit. The statistics allowed to use bins with 8-hour intervals for F1 and 3-hour bins for F2. For example, from MJD 57317 to MJD 57322, the detection significance varied between  $5.1\sigma$  and  $13.1\sigma$ , and from MJD 557753 to MJD 57754 it was between  $5.3\sigma$  and  $10.4\sigma$ . The corresponding light curves are shown in the middle panels of Fig. 6.2. In order to check if the likelihood fit has converged in each time bin, the plot of  $N_{pred} / \sqrt{N_{pred}}$  vs  $Flux / \Delta Flux$  is shown in the lower panels of Fig. 6.2 for 8-hour (left) and 3-hour (right) bins. We verified that the fit has converged in the surrounding bins as well. As one can see, it seems there is a linear correlation without any declination, so the errors are an accurate representation of the observation.

Further, the  $\gamma$ -ray flux and photon index variations are investigated using a light curve generated by an adaptive binning method [32]. In this method, the time bin widths are flexible and chosen to produce bins with a constant flux uncertainty. This method allows detailed investigation of the flaring periods, since at times of a high flux, the time bins are narrower than during lower flux levels, therefore rapid changes of the flux can be found. In order to reach the necessary relative flux uncertainty, the integral fluxes are computed above the optimal energy [32] which in this case is  $E_0 = 208.6$  MeV. Also, in order to improve the accuracy of the method, the flux of bright sources which lie close to NGC 1275 have been taken into account. This is done by providing the parameters of confusing sources during the adaptive binning light curve calculations. The light curve calculated assuming a constant 15% uncertainty is shown in Fig. 5.2 (upper panels) for the period covering the large flares.



**Figure 5.2:** Top panels: The upper panel shows the period of major flares with the constant uncertainty (15%) light curve above 208.6 MeV obtained with the adaptive binning method. The lower panel shows the photon index variation during the same period. Bottom panels: The photon index vs. the flux above 208.6 MeV for F1 (left) and F2(right).

## 5.3 Spectral analysis

### 5.3.1 Fermi data

The changes in the  $\gamma$ -ray photon index are investigated by analyzing the data from the following four periods:

- i) overlapping with the observation of Swift on 30 December 2016. Even if the Swift observations lasted  $\sim 960$  seconds, in order to increase the statistics, the  $\gamma$ -ray spectrum has been extracted for the period MJD 57752.75-57753.25 where the source has a comparable flux as revealed from the light curve with a 6-hour binning (Fig. 6.2, middle right panel).
- ii) MJD 57754.00-57755.75, when the flux is relatively constant and it coincides with the observations of Swift on 01 January 2017.
- iii) at the peak of F2 (MJD 57753.81), using the data accumulated for 3 hours.
- iv) MJD 57442.32-57444.45, which corresponds to the quiet (steady) state in the X-ray and  $\gamma$ -ray bands.

The  $\gamma$ -ray spectrum of NGC 1275 has been modeled using a power-law function ( $dN/dE \sim N_0 E^{-\Gamma}$ ) where the normalization ( $N_0$ ) and power-law index ( $\Gamma$ ) are considered as free parameters. The best matches between the spectral models and events are obtained with an unbinned likelihood analysis implemented in *gtlike*. The spectral fitting results are summarized in Table 5.1. After analyzing the data for each considered period, the SEDs are obtained by freezing the NGC 1275 photon index in the model file and separately running *gtlike* for smaller energy bins of equal width in log scale. The SED for each period is shown in Fig. 5.3. Although some features can be noticed, it is hard to make any conclusion because of large uncertainties in the estimated parameters.

We separately analyze the *Fermi* data to determine the energy of the highest energy photon detected from NGC 1275 using *gtsrcprob* tool and the model file obtained from the likelihood fitting. All spectral parameters of the sources within ROI are first fixed to the best fitting values obtained in the whole time analysis and then are left free. Both yielded identical results. In this case, additional care must be taken since IC 310, which is known to be a strong emitter in the VHE  $\gamma$ -ray band [9], is only at a distance of  $0.623^\circ$ . So both

sources are considered to estimate the probability whether the photon belongs to NGC 1275 or to IC 310. The highest-energy photons detected during the four periods mentioned above are presented in Table 5.1.

### 5.3.2 Swift UVOT/XRT data

During F2, Swift [24] had observed NGC 1275 three times (see Table 5.1). Unfortunately, there were no observations overlapping with F1. In addition to these observations, the Swift data of February 25, 2016, corresponding to a relatively stable state in the X-ray band have been analyzed. The XRT data were analyzed with the XRTDAS software package (v.3.3.0) distributed by HEASARC along with the HEASoft package (v.6.21). The source region was defined as a circle with a radius of 10.6 pixels ( $25''$ ) at the center of the source, while the background region as an annulus centered at the source with its inner and outer radii being 20 ( $47''$ ) and 30 pixels ( $71''$ ), respectively. Such selections allowed to minimize the possible contribution from the cluster emission. For PC mode observations (Obsid 87312001, 87311001), the count rate was above 0.5 count/s, being affected by the piling-up in the inner part of the PSF. This effect was removed, excluding the events within a 4 pixel radius circle centered on the source position. All spectra were re-binned to have at least 20 counts per bin, ignoring the channels with energy below 0.3 keV, and fitted using Xspec v12.9.1a. The results of the fit are presented in Table 5.1. In the analysis of Swift-UVOT data, the source counts were extracted from an aperture of  $5.0''$  radius around the source. The background counts were taken from the neighboring circular source-free region with a radius of  $20''$ . The magnitudes were computed using the uvotsource tool (HEASOFT v6.21) corrected for extinction according to [43], using  $E(B - V) = 0.14$  from [45] and zero points from [16] converted to fluxes, following [40]. The corresponding spectra are shown in Fig. 5.3.

## 5.4 RESULTS and DISCUSSIONS

The  $\gamma$ -ray emission from one of the brightest radio galaxies in the MeV/GeV band- NGC 1275- has been investigated using the *Fermi* data accumulated during the last  $\sim 8.7$  years. The  $\gamma$ -ray light curve appears to be quite a complex one, with many peaks and flaring periods. The highest fluxes were detected in October 2015 and December 2016/January 2017 when the daily

averaged peak  $\gamma$ -ray fluxes  $\simeq (1.48 - 2.21) \times 10^{-6}$  photons  $cm^{-2} s^{-1}$  integrated above 100 MeV were detected. It reached its maximum of  $(3.48 \pm 0.87) \times 10^{-6}$  photon  $cm^{-2} s^{-1}$  on December 31, 2016, within 3 hours, which is the highest  $\gamma$ -ray flux observed from NGC 1275 so far; it exceeds the averaged flux by a factor of  $\sim 15.4$ . The apparent isotropic  $\gamma$ -ray luminosity at the peak of the flare,  $L_\gamma \simeq 3.84 \times 10^{45}$  erg  $s^{-1}$  (using  $d_L = 75.6$  Mpc), exceeds the averaged  $\gamma$ -ray luminosity of other radio galaxies detected by *Fermi* (usually  $\leq 10^{45}$  erg  $s^{-1}$  [5]); it is more comparable with the luminosity of BL Lac blazars. This is quite impressive, considering the large Doppler boosting factors of blazars ( $\delta \geq 10$ ) as compared with the value of  $\delta \sim (2 - 4)$  usually used for the radio galaxies. Yet, at  $\delta = 4$  the total power emitted in the  $\gamma$ -ray band in the proper frame of the jet would be  $L_{em,\gamma} \simeq L_\gamma / 2 \delta^2 \simeq 1.2 \times 10^{44}$  erg  $s^{-1}$ . It is of the same order as the kinetic energy of the NGC 1275 jet ( $L_{jet} \simeq (0.6 - 4.9) \times 10^{44}$  erg  $s^{-1}$ ) estimated from broadband SED modeling [2]. This implies that during the discussed flaring period a substantial fraction of the total jet power, ( $L_{em,\gamma} / L_{jet} \leq 1$ ), is converted into  $\gamma$ -rays. These assumptions are in a strong dependence with  $\delta$ , which is highly unknown. But it seems that  $\delta = 4$  is already a limiting case, and larger decrease of  $L_{em,\gamma}$  is not expected.

The  $\gamma$ -ray spectrum estimated during the peak flux appeared as a nearly flat one (cyan data in Fig. 5.3), though the photon index estimation uncertainty is large ( $\Gamma = 1.93 \pm 0.19$ ). This is similar with the spectrum measured in a quiet state (Fig. 5.3, gray data), although with a significantly increased flux. The  $\gamma$ -ray photon index measured before and after the peak flux hints at spectral hardening (see Table 5.1 and Fig. 5.3 blue and red data). However, large uncertainties in the photon index estimations do not allow us to make strong conclusions on the spectral hardening or softening. Although, as compared with the quiet state, it is clear that during the active states the  $\gamma$ -ray flux increases and the spectrum shifts to higher energies.

The broadband SED of NGC 1275 (Fig. 5.3) shows that during the bright  $\gamma$ -ray states, the X-ray flux also has increased. The analysis of the Swift XRT data detected during F2 results in an unabsorbed flux of  $F_{0.3-10 keV} \simeq (0.86 - 1.06) \times 10^{-10}$  erg  $cm^{-2} s^{-1}$  which nearly 3 times exceeds the averaged flux observed in February 2016. We note that the X-ray photon index measured during the quiet state is somewhat similar to the values measured by XMM-Newton [19] and Swift BAT [11] while during the active states the X-ray photon index is steeper ( $\sim 1.7$ ). In the lower energy band, the UV flux from UVOT observations is relatively stable when comparing the quiescent

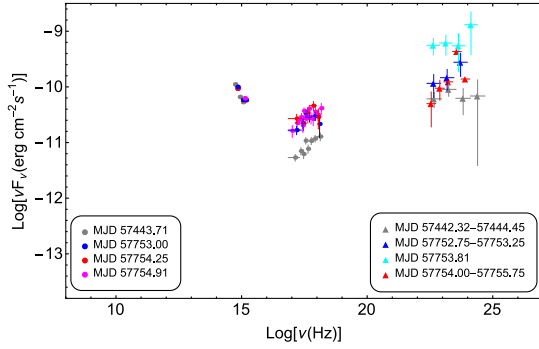


Figure 5.3: The multiwavelength SED for the periods presented in Table 5.1.

Table 5.2: Parameter values best explaining the flares.

| Flare period               | $t_r \pm err$<br>(hour) | $t_d \pm err$<br>(hour) | $t_0$<br>MJD        | $F_c$<br>$\times 10^{-7} \text{ photon cm}^{-2} \text{ s}^{-1}$ | $F_0$<br>$\times 10^{-7} \text{ photon cm}^{-2} \text{ s}^{-1}$ |
|----------------------------|-------------------------|-------------------------|---------------------|---|---|
| 2015 October               | $32.49 \pm 7.20$        | $2.22 \pm 1.19$         | $57320.41 \pm 0.19$ | $8.43 \pm 1.42$   | $23.92 \pm 3.08$  |
| 2016 December/2017 January | $8.03 \pm 1.24$         | $1.21 \pm 0.22$         | $57753.88 \pm 0.04$ | $9.73 \pm 1.75$   | $41.96 \pm 4.82$  |

and flaring states, albeit the data from all filters are not available to make definite conclusions.

#### 5.4.1 $\gamma$ -ray photon index variation

The  $\gamma$ -ray photon index changes during  $\sim 8.7$  years of *Fermi* observations are investigated with the help of an adaptively binned light curve. In Fig. 5.2 (upper panels) the photon flux and index variation in time are shown for the time that covers only F1 and F2. In the course of  $\sim 8.7$  years, the hardest photon index of  $\Gamma = 1.62 \pm 0.13$  was observed on MJD 55331.51 for  $\sim 2.78$  days, while the softest index of  $\Gamma = 2.77 \pm 0.21$  was detected on MJD 56124.71. The lowest and highest fluxes (above 208.6 MeV) were  $F_\gamma = (4.27 \pm 1.06) \times 10^{-8} \text{ photon cm}^{-2} \text{ s}^{-1}$  and  $F_\gamma = (1.18 \pm 0.28) \times 10^{-6} \text{ photon cm}^{-2} \text{ s}^{-1}$ , respectively. When the source is in active state, the data accumulated for a few hours is already enough to reach 15% flux uncertainty, while in the quiet states, the data should be accumulated for several days. Interestingly, in the first  $\sim 8.7$  years of *Fermi* operation, the highest-energy photon with  $E_\gamma = 241.2 \text{ GeV}$  has been detected on MJD 57756.62 (after F2) within a circle of  $0.071^\circ$  around the nucleus of NGC 1275 with the  $3.36\sigma$  probability to be associated with it. Another events with  $E_\gamma = 221.5, 164.9, 125.6, 123.3$

and 109.2 GeV have been observed on MJD 55402.39, 56760.82, 56610.75, 56578.00 and 57694.65, respectively. We note that the PSF of *Fermi* at energies  $> 10$  GeV is sufficient to distinguish the photons with high accuracy, so the highest energy photons are most likely coming from NGC 1275. It appeared that the  $\gamma$ -ray spectra for the periods when the highest energy photons were emitted, have mostly harder photon indexes (e.g.,  $\Gamma = 1.74 \pm 0.14$  when  $E_\gamma = 241.2$  GeV photon was detected). Likewise, when photons with  $E_\gamma = 221.5, 164.9, 125.6, 123.3$  and 109.2 GeV were detected, the photon indexes were  $\Gamma = 1.81 \pm 0.15, 1.93 \pm 0.15, 1.79 \pm 0.13, 1.94 \pm 0.14$  and  $1.86 \pm 0.15$ , respectively. This hardening is probably associated with the emission from reaccelerated or fresh electrons, which produce also the observed highest energy photons.

The spectral changes observed in the photon-index-flux plane give us important information about the dynamics of the source and an insight into the particle acceleration and emission processes. The photon index  $\Gamma$  as a function of the flux during F1 and F2 is shown in the bottom panels of Fig. 5.2. A counter-clockwise loop is observed during F1, while during F2 the spectral index and flux changes follow a clockwise path. Such loops are expected to occur as a consequence of diffusive particle acceleration at strong shocks and cooling of the radiating particles. As discussed in [29], it is expected to have a counter-clockwise loop, if the variability, acceleration and cooling timescales are similar, implying that during the flare, the spectral slope is controlled by the acceleration rather than by the cooling processes. Consequently, the occurrence of a flare propagates from lower to higher energies, so the lower energy photons lead the higher energy ones. Instead, if the spectral slope is controlled by synchrotron cooling or any cooling process that is faster at higher energies, a clockwise loop will be seen. The counter-clockwise loop observed during F1 suggests that, most likely, this flaring event is due to the acceleration of the lower-energy electrons. Note that such ‘harder-when-brighter’ behavior was already observed during the previous flares of NGC 1275 [28, 17]. The clockwise loop observed during F2 indicates that during this flare the flux started to increase at low energies (HE radiating particles cool down and radiate at lower and lower energies) and then propagate to HE. This shows that HE electrons are playing a key role during F2, which also produce the highest energy photons from NGC 1275 observed around F2.

The interpretation of the mechanism responsible for spectral evolution can be more complicated than it was discussed above. It has been already shown

that, depending on the change of the total injected energy, the dominance of synchrotron and Compton components can also vary, so that the trajectory in the photon index-flux plane evolves clockwise or counterclockwise, depending on the total energy and the observed energy bands [15, 31]. Thus, the observed spectral evolution is quite sensitive to various parameters in the model and it is hard to draw any firm conclusions. The discussions above are of first order approximation and are generally meant to understand the dynamics of the system.

### 5.4.2 Minimum flux variability period:

During F1 and F2, the flare time profiles are investigated by fitting them (Fig. 6.2 middle panels blue data) with double exponential functions in the following form [4]:

$$F(t) = F_c + F_0 \times \left( e^{\frac{t-t_0}{t_r}} + e^{\frac{t_0-t}{t_d}} \right)^{-1} \quad (5.4.1)$$

where  $t_0$  is the time of the maximum intensity of the flare ( $F_0$ ) and  $F_c$  is the constant level present in the flare.  $t_r$  and  $t_d$  are the rise and decay time constants, respectively. The fitting parameters are summarized in Table 5.2 and the corresponding fit is shown in Fig. 6.2 middle panels (red dashed line). The time profiles show asymmetric structures in both flares, showing a slow rise and a fast decay trend. The time peak of the flares calculated by  $t_p = t_0 + t_r t_d / (t_r + t_d) \ln(t_d / t_r)$  is MJD 57320.18 for F1 with the maximum intensity of  $(2.39 \pm 0.31) \times 10^{-6}$  photon  $\text{cm}^{-2} \text{s}^{-1}$ . The rise time is  $32.49 \pm 7.20$  hours with a sudden drop within  $2.22 \pm 1.19$  hours. The parameters of F2 are better estimated and are characterized with a shorter rise time, when within  $8.03 \pm 1.24$  hours the flux reaches its maximum of  $(4.20 \pm 0.48) \times 10^{-6}$  photon  $\text{cm}^{-2} \text{s}^{-1}$  on MJD 57753.79 and drops nearly 4 times in  $\sim 6$  hours. The minimal e-folding time is  $t_d = 1.21 \pm 0.22$  hours, using the decay time scale of F2, and it is the most rapid  $\gamma$ -ray variability observed for NGC 1275. We note that even if the rise time of F2 is used, the flux e-folding time of about  $8.03 \pm 1.24$  hours will still be shorter than any previously reported value.

The obtained shortest flux e-folding time,  $t_d = 1.21 \pm 0.22$  hours, is unusual for radio galaxies and has never been observed for any other radio galaxy so far. It is more similar to the rapid  $\gamma$ -ray variability detected from several bright blazars [18, 22, 23, 44, 37, 27, 41, 7]. [18] was the first to point out that during the  $\gamma$ -ray flares of PKS 1510-089 the flux doubling time-scale was as

short as  $1.3 \pm 0.12$  hours which was the shortest variability time-scales measured at MeV/GeV energies at that time. It is interesting that such rapid  $\gamma$ -ray variability is mostly observed from flat-spectrum radio quasars. The asymmetric profile of NGC 1275 flares can be explained if assumed that the accelerated particles (e.g., by shock acceleration) quickly cool down due to the increase of the magnetic field (assuming the electrons dominantly lose energy by synchrotron cooling). In order to interpret the fast decay ( $t_{dec} = 1.21 \pm 0.22$  hours) as cooling of relativistic electrons ( $t_{decay} = t_{cooling}/\delta$ ;  $t_{cooling} = 6 \pi m_e^2 c^3 / \sigma_T B^2 E_e$ ) with  $E_e = 100 \text{ GeV}$ , the magnetic field should be  $B \approx 478 \text{ mG} (\delta/4)^{-1/2} (t_{dec}/1.2 \text{ h})^{-1/2} (E_e/100 \text{ GeV})^{-1/2}$  (where we assumed a moderate Doppler boosting factor of  $\delta = 4$ ), which is not far from the typical values usually used in the modeling of emission from radio galaxies [1, 3]. Even if the magnetic field is 10 – 100 times lower than this value, the shock acceleration time scales ( $t_{acc} \approx 6 r_g c / v_s^2$  [42]) would be more than enough to accelerate the electrons  $> 100 \text{ GeV}$  within the observed rise time scale ( $8.03 \pm 1.24$  hours).

### 5.4.3 The origin of emission

The observed short time scale variability of  $1.21 \pm 0.22$  hours allows to constrain the characteristic size of the emitting region radius to  $R_\gamma \leq \delta \times c \times \tau \approx 5.22 \times 10^{14} (\delta/4) \text{ cm}$ . If the entire jet width is responsible for the emission, assuming the jet half-opening angle  $\theta_j \simeq 0.1^\circ$ , the location of the emitting region along the jet will be  $r \simeq R_\gamma / \theta_j \simeq 0.1 (\delta/4) (\theta_j/0.1^\circ)^{-1} \text{ pc}$ . This strongly suggests that the observed emission is most likely produced in the subparsec-scale jet. In principle the jet can be much more extended and the emission is produced in a region smaller than the width of the jet. For example, multiple regions moving in a wider jet having different beaming factors can be an alternative possibility [30]. In this model, the emission is expected to take place in a broadened jet formation zone close to the central supermassive black hole, where even for a large jet angle, a few emission zones can move directly toward the observer and Doppler boost the emission. Here the emission region is very close to central source, again implying that the innermost jet (subparsec-scale) is responsible for the emission.

The SED presented in Fig. 5.3 as well as that in [10], hint at a double-peaked SED similar to those of other GeV/TeV-emitting radio galaxies [1, 3] and blazars. This similarity allowed to model the SED of NGC 1275 within the

one-zone synchrotron SSC scenario [10]. However, it failed to reproduce the required large separation of the two peaks (gray data in Fig. 5.3) with small Doppler factors ( $\delta = 2 - 4$ ) typical for radio galaxies. With the new data, the situation even worsened: even if the data are not enough to exactly identify the location of the peaks, clearly, the first peak is at  $\sim (10^{14} - 10^{15})\text{Hz}$  (unchanged) while the rising shape of the MeV/GeV spectrum indicates the second peak shifted to higher frequencies. Such large separation of the two SED peaks unavoidably requires a higher Doppler factor than that used previously. Moreover, if one-zone SSC emission dominates, usually it is expected to have correlated changes in the X-ray/ $\gamma$ -ray band, which are not observed here. One can avoid these difficulties by assuming that HE emission is produced in a local substructure of the jet, which is characterized by a higher boosting factor and/or smaller inclination angle. For example, the mini-jets generated by local reconnection outflows in a global jet ('jets in a jet' model [25]) can have extra Lorentz boosting and the emission can be produced around these local reconnection regions. This successfully explains the fast TeV variability of M87 [26] so that it can be naturally considered also in this case. In addition, two-zone SSC models, when different regions are responsible for low and high-energy emissions, can be an alternative. In more complex-structured jet models the seed photons for IC scattering can be of external origin (the emission region is the layer and external photons are from the spine, or vice versa [46]) the energy of which is higher than that of synchrotron photons resulting in the shift of the emission peak to higher energies. However, these models involve additional parameters, which cannot be constrained with the current data set and additional observations in the radio/optical and VHE  $\gamma$ -ray bands are required.

## 5.5 SUMMARY

We report on the results of  $\sim 8.7$  years'  $\gamma$ -ray observations of NGC 1275 radio galaxy. The source displayed prominent flaring activities in October 2015 and December 2016/January 2017 with the 3-hour peak flux above 100 MeV of  $(3.48 \pm 0.87) \times 10^{-6} \text{ photon cm}^{-2} \text{ s}^{-1}$  observed on 2016 December 31 corresponding to an apparent isotropic  $\gamma$ -ray luminosity of  $L_\gamma \simeq 3.84 \times 10^{45} \text{ erg s}^{-1}$ . This luminosity is more typical for BL Lac blazars and corresponds to a large fraction of the kinetic energy of the NGC 1275 jet, implying that the  $\gamma$ -ray production efficiency is very high.

During the major flares, the photon statistics allowed us to investigate the flare properties with as short as 3-hour intervals for the first time. This allowed to find very rapid variability with the flux e-folding time as short as  $1.21 \pm 0.22$  hours, which is very unusual for radio galaxies. The  $\gamma$ -ray photon index of the source was evolving during the flaring periods, showing counter clockwise and clockwise loops in the photon-index-flux plane during the flares in October 2015 and December 2016/January 2017, respectively. Also, some of the highest energy  $\gamma$ -ray photons observed from the source during  $\sim 8.7$  years arrived around the same active periods. Perhaps this rapid  $\gamma$ -ray flare was associated with effective particle acceleration that led to emission of these photons.

The observed hour-scale variability suggests that the emission is produced in a very compact emission region with  $R_\gamma \leq 5.22 \times 10^{14} (\delta/4) \text{ cm}$ , and perhaps it is produced in a sub-parsec scale jet. During the  $\gamma$ -ray activity, the HE component not only increased but also shifted to higher energies. Considering this shift and the large  $\gamma$ -ray luminosity, it makes it very challenging to explain the observed X-ray and  $\gamma$ -ray data in the standard synchrotron/SSC models. Additional assumptions on the jet structure/emission processes are to be made.

# 6 High Energy Gamma-Ray Emission From PKS 1441+25

## 6.1 Introduction

Recent observations in the  $\gamma$ -ray band ( $\geq 100$  MeV) show that the extragalactic  $\gamma$ -ray sky is dominated by emission from blazars - an extreme class of Active Galactic Nuclei (AGNs) which have jets that are forming a small angle with respect to the line of sight [92]. Blazars are known to emit electromagnetic radiation in almost all frequencies that are currently being observed, ranging from radio to Very High Energy (VHE;  $> 100$  GeV)  $\gamma$ -ray bands. The broadband spectrum is mainly dominated by non-thermal emissions produced in a relativistic jet pointing toward the observer. Due to small inclination angle and large bulk motion, the emission from blazars is affected by relativistic beaming which has enormous effects on the observed luminosities. Indeed, the observed luminosity ( $L_{obs}$ ) is related to the emitted luminosity ( $L'_{em}$ ) as  $L_{obs} = \delta^{3+\alpha} L'_{em}$ . If so, the observed luminosity can be thus amplified by a factor of thousands or even more (usually  $\delta \geq 10$ ). Such amplification makes it possible to detect emission even from very distant blazars. A key feature of the non-thermal emission from blazars is the distinct variability at all frequencies (with different variability time scales - from years down to a few minutes). The shortest variability time scales are usually observed for the highest energy band; an example is the minute scale variability of PKS 2155-304 [10] and IC 310 [16] which implies that the emission is produced in a very compact region. Therefore, by observing blazars one gets a unique chance to investigate the jet structure on sub-parsec scales.

By their emission line features blazars are commonly grouped as BL Lacertae objects (BL-Lacs) and Flat-Spectrum Radio Quasars (FSRQs) [92]. BL Lacs have weak or no emission lines, while FSRQs have stronger emission lines. The difference in the emission-line properties of FSRQs and BL Lacs may be connected with that in the properties of accretion in these objects [33].

The multiwavelength observations of blazars have shown that their Spectral Energy Distribution (SED) has two broad non-thermal peaks - one at the IR/optical/UV/X-ray and the other at the Higher-Energy (HE;  $> 100$  MeV)  $\gamma$ -ray band. The low-energy peak is believed to be due to the non-thermal synchrotron emission of relativistic electrons while the origin of the second component is still debated. One of the most widely accepted theories for the second peak is that it is produced from Inverse Compton (IC) scattering of low energy synchrotron photons (Synchrotron Self Compton; SSC) [34, 62, 20] which often successfully explains the emission from BL-Lacs [27]. Besides, the photons from the regions outside the jet may serve as seed photons for IC scattering - External Compton (EC) models which are used to model the emission from FSRQs. The external photon field can be dominated either by the photons reflected by BLR [86] or by photons from a dusty torus [19, 37]. Domination of one of the components mostly depends on the localization of the emitting region; for example, if the energy dissipation occurs within BLR then the observed HE emission is mostly due to IC scattering of BLR reflected photons, otherwise, if the emitting region is far from the central source, then the IC scattering of torus photons will dominate. SSC and EC models assume that the emission is produced by the same population of electrons, though up to now it is not clear whether it is produced in the same part of the jet or by different electron populations. Alternatively, the HE emission can be explained by the interaction of energetic protons; e.g., a significant fraction of the jet power goes for acceleration of protons so that they reach the threshold for pion production [66, 67].

The majority of the blazars detected in VHE  $\gamma$ -ray band are high-frequency-peaked BL Lacs for which the synchrotron bump is in the UV/X-ray bands. In addition to BL Lacs, there are also 5 FSRQs detected in the VHE  $\gamma$ -ray band which is rather surprising, since the Broad Line Region (BLR) structure of these objects, which is rich in optical-UV photons, makes these environments strongly opaque to VHE  $\gamma$ -rays [59, 75]. Moreover, FSRQs have a relatively steep photon index in the energy range of  $> 100$  MeV as was observed with the Fermi Large Area Telescope (Fermi LAT) which does not make them as strong emitters of VHE  $\gamma$ -ray photons. Detection of FSRQs in the VHE  $\gamma$ -ray band is challenging for the near-black-hole dissipation scenarios; it assumes that the  $\gamma$ -rays are most likely produced farther from the central source, outside the BLR, where the dominant photon field is the IR emission from the dusty torus. Typically, the temperature of torus photons  $\sim 10^3$  K is lower than that of the photons reflected in the BLR  $\sim 10^5$  K, and, in principle, VHE

photons with energy up to  $\sim 1$  TeV can escape from the region. Thus, the observations of FSRQs in VHE  $\gamma$ -ray band provide an alternative view of blazar emission as compared to BL Lacs. Moreover, since FSRQs are more luminous than BL Lacs, they could, in principle, be observed at greater distances. Indeed, the farthest sources detected in the VHE  $\gamma$ -ray band are the FSRQs at a redshift of  $z \geq 0.9$  (e.g., PKS 1441+25 [6, 15] and S3 0218+35 [14]). That is why FSRQs are ideal for estimation of the intensity of Extragalactic Background Light (EBL) through the absorption of VHE photons when they interact with the EBL photons [24, 61].

Among FSRQs, PKS 1441+25 is one of the most distant sources detected so far at  $z=0.939$  [85]. In April 2015 both VERITAS and MAGIC collaborations announced the detection of VHE  $\gamma$ -rays from PKS 1441+25 (with up to 250 GeV photons) [35, 36]. A strong emission from the source had been detected on April 20 to 27, 2015. During the same period, the source had been also observed with the telescopes Swift and NuSTAR. The origin of the multiwavelength emission from PKS 1441+25 observed in April is modeled assuming the emission region is beyond the BLR, and the emission in the VHE  $\gamma$ -ray band is mostly due to the IC scattering of the dusty torus photons [6, 15]. Moreover, the large distance to PKS 1441+25 allowed to indirectly probe the EBL absorption at redshifts up to  $z \sim 1$  with the help of ground-based  $\gamma$ -ray instruments.

In the theoretical interpretation of the multiwavelength emission from blazars, the size/location of the emitting region, magnetic field and electron energy distribution are uncertain. Only during flaring periods some of the unknown parameters can be constrained based on the observations in different bands. The observations of PKS 1441+25 during the bright period in April 2015 by different instruments provide us with data on the maximums of the emitting components (Swift UVOT/ ASAS-SN and Fermi LAT) as well as on the transition region between these components in the energy range from 0.3 to 30 keV (Swift XRT and NuSTAR) [6]. Similar data (up to HE  $\gamma$ -ray band) are available also from the observations carried out on January 06 to 28, 2015, which is the period of the large flare that was observed with Fermi LAT. Thus, by modeling the emission in these two periods and estimating the parameter space that describes the underlying particle distribution responsible for the emission through the Markov Chain Monte Carlo (MCMC) technique, one can investigate and explore particle acceleration/emission processes and jet properties in these two significant flaring periods which are crucial for understanding the origin of the flares. This motivated us to have a new look

at the origin of the multiwavelength emission from PKS 1441+25, using currently available data from Swift, NuSTAR and Fermi LAT.

This paper is structured as follows. The results of the spectral and temporal analysis of the Fermi LAT data are presented in Section 6.2. The broadband SED modeling with MCMC technique is presented in Section 6.3 and discussion and conclusions are presented in Section 6.4.

## 6.2 Fermi LAT DATA ANALYSIS

The large Area Telescope on board the Fermi satellite is a pair-conversion telescope sensitive to  $\gamma$ -rays in the energy range from 20 MeV to 300 GeV. It constantly scans the whole sky every 3 hours already more than 8 years. More details about Fermi LAT can be found in [18].

In the present paper, for spectral analysis we use the publicly available data acquired in the periods from January 06 to 28 and from April 15 to 26, 2015. These two periods have been picked, because they are contemporaneous with the Swift XRT observations of the source [6]. The data were analyzed with the standard Fermi Science Tools v10r0p5 software package released on May 18, 2015 available from the Fermi Science Support Center <sup>1</sup>. The latest re-processed PASS 8 events and spacecraft data are used with the instrument response function P8R2\_SOURCE\_V6. We have downloaded photons in the energy range from 100 MeV to 100 GeV from a region of interest defined as a circle of a  $20^\circ$  radius centered at the  $\gamma$ -ray position of PKS 1441+25 (RA, Dec) = (220.996, 25.039) [7]. Only the events with higher probability of being photons (evclass=128 evtype=3) have been considered in the analysis. A cut on the zenith angle of  $90^\circ$  is applied to reduce contamination from the Earth-limb  $\gamma$ -rays produced by cosmic rays at their interaction with the upper atmosphere. The model file, describing the region of interest, contains point sources from the Fermi LAT third source catalog [7] (3FGL) within  $25^\circ$  from the target, as well as contains Galactic gll\_iem\_v05\_rev1 and isotropic iso\_source\_v05 diffuse components. All point-source spectra were modeled with those given in the catalog, allowing the photon index and normalization of the sources within  $20^\circ$  to be free in the analysis. Also, the normalization of diffuse background components was not fixed.

---

<sup>1</sup><http://fermi.gsfc.nasa.gov/ssc/data/analysis/software/>

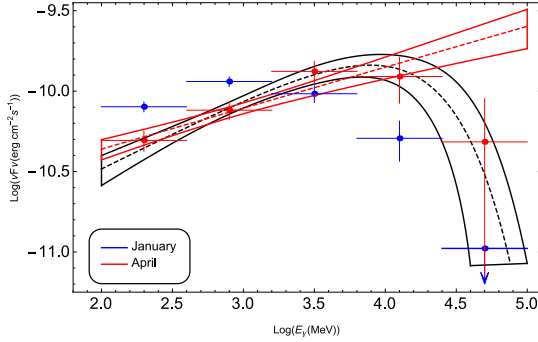


**Figure 6.1:** The  $\gamma$ -ray spectrum of PKS 1441+25 above 100 MeV averaged over the Fermi LAT observations in January (blue) and April (red).

| Parameter Name                     | Blue                             | Red                              |
|------------------------------------|----------------------------------|----------------------------------|
| Flux ( $photon\ cm^{-2}\ s^{-1}$ ) | $(5.89 \pm 0.30) \times 10^{-7}$ | $(3.63 \pm 0.36) \times 10^{-7}$ |
| $\alpha$                           | $1.99 \pm 0.04$                  | $1.74 \pm 0.06$                  |
| TS                                 | 2174                             | 910                              |

**Table 6.1:** The best parameters obtained with gtlake for power-law modeling. For each time period, photon flux in the range 0.1 – 100 GeV, photon index and detection significance are presented.

### 6.2.1 Spectral analysis

In order to find the best matches between spectral models and events, an unbinned likelihood analysis is performed with gtlake. The PKS 1441+25 spectrum has been initially modeled as a power-law function where the normalization and the power-law index are taken as free parameters. The best fit parameters obtained with gtlake analysis are presented in Table 6.1 and the corresponding spectrum is shown in Fig. 6.1 (blue and red data for January and April, respectively). The spectrum is calculated by separately running gtlake for 5 energy bands equal on a log scale.

The fluxes presented in Table 6.1 significantly exceed the averaged flux given in 3FGL ( $\approx 1.28 \times 10^{-8}\ photon\ cm^{-2}\ s^{-1}$ ) [7]. The photon index estimated in January 2015 is consistent with the value reported in 3FGL  $\alpha = 2.13$  (averaged over 4 years of observations); however, a relative hardening of  $\alpha = 1.74 \pm 0.06$  is observed in April, which is rarely observed for FSRQs. Moreover, we note an indication of deviation of the power-law model with

## 6 High Energy Gamma-Ray Emission From PKS 1441+25



**Figure 6.2:** The  $\gamma$ -ray light curve of PKS 1441+25 from January to December 2015 (a). The bin intervals correspond to 1- day (blue data) and 3-days (green data). The light curve obtained by adaptive binning method assuming 20 % of uncertainty is presented in red (b). The change of photon index for 3-day binning (green) and with adaptive binning method are shown in (c).

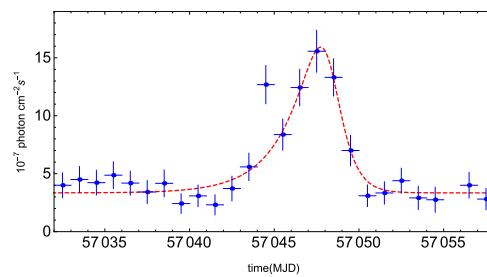


**Figure 6.3:** The light curve's sub interval that covers a major flaring period. The red dashed line shows the flare fit with Eq. 6.2.1.

respect to the data above 10s of GeV energies observed in April (red bowtie plot in Fig. 6.1). In order to check for a statistically significant curvature in the spectrum, an alternative fit of the power-law with an exponential cutoff function in the form of  $dN/dE \sim E_{\gamma}^{-\alpha} \times \text{Exp}(-E_{\gamma}/E_{cut})$  is done, which results in  $\alpha = 1.56 \pm 0.1$  and  $E_{cut} = 17.7 \pm 8.9$  GeV (black bowtie plot in Fig. 6.1). The power-law and cutoff models are compared with a log likelihood ratio test: the TS is twice the difference in the log likelihoods, which gives 8 for this case. Note that the TS probability distribution can be approximated by a  $\chi^2$  distribution with 1 degree of freedom (dof) corresponding to the difference of the dof between the two functions. The results give  $P(\chi^2) = 0.0046$ , which again indicates a deviation from a simple power-law function. The best-fit cutoff power-law function is shown as a black bowtie line in Fig. 6.1. However,  $2.8\sigma$  is not a high enough significance to claim for a statistically significant curvature although it is as high as  $3.86\sigma$  if the data collected during the whole month of April are considered.

### 6.2.2 Temporal analysis

In order to investigate the size of the  $\gamma$ -ray emitting region, light curves with different time binning are generated. A characteristic timescale for flux variation  $\tau$  would limit the (intrinsic) size of the emission region to  $R \leq c \times \delta \times \tau / (z + 1)$ . Thus, it is crucial to do a variability analysis in order to distinguish between different emission processes.

The light curve of PKS 1441+25 for the period from January to December 2015 has been calculated by the gtlake tool, applying the unbinned likelihood analysis method. (0.1 – 100) GeV photons from a region with a  $10^\circ$  radius centered on the position of PKS 1441+25 are used in the analysis with the appropriate quality cuts applied as in the previous case. During the analysis, in order to reduce the uncertainty in the flux estimations, in the model file the photon indices of all background sources are fixed to the best guess values. Two different sets of light curves are calculated, considering the power-law index of PKS 1441+25 as being fixed and then as free. Since no variability is expected for the background diffuse emission, the normalization of both background components is also fixed to the values obtained for the whole time period.

The  $\gamma$ -ray light curve of PKS 1441+25 obtained with one-day and three-days binning is presented in Fig. 6.2 (a) (blue and green data respectively). In the

light curve there can be identified several periods when the flux was in high as well as in quiescent states. A major increase of the  $\gamma$ -ray flux had been detected in the period from January 21 to 28, 2015, with a daily averaged maximum of  $(1.55 \pm 0.18) \times 10^{-6} \text{ photon cm}^{-2} \text{ s}^{-1}$  observed on January 25, 2015. Unfortunately the peak flare of January 25 was not observed by Swift. The  $\gamma$ -ray photon index evolution in time in a three-day long binning is shown in Fig. 6.2 (c) with green data (three-day long binning is used since the photon index uncertainties are less than in one-day binning). During the flaring period the photon index is 1.9 – 2.0. Also an increase in the flux can be noticed around January 22nd which lasted just one day. In order to check if this brightening is statistically significant, light curves with denser time sampling (half a day and 4 hours) are generated. However, the corresponding flux increase is within the uncertainty of the surrounding bins, while the peak of the flux around 25th of January is present in both light curves. In addition, a substantial increase in the  $\gamma$ -ray flux was observed in April, from June to about July 15, mid August and around October-November; but the maximum flux intensity was lower as compared with that observed during the strong  $\gamma$ -ray outburst of January 21 to 28 (Fig. 6.2). The active state in April is the period when PKS 1441+25 was observed by MAGIC on MJD 57130-57139 and VERITAS on MJD 57133-57140 [6, 15]. The  $\gamma$ -ray light curve with three-day binning shows that, between MJD 57125.56- 57140.64 (from April 13 to April 28, 2015), the  $\gamma$ -ray photon index is significantly harder,  $\Gamma = (1.73 - 1.79)$ . It implies that during the observations in the VHE band the source was in a state characterized by a hard  $\gamma$ -ray photon index in the MeV-to-GeV range. Next, in order to investigate the flux changes in time, and in particular in the flaring periods, the light curves have been generated by an adaptive binning method. In this method, the time bin widths are flexible and chosen to produce bins with constant flux uncertainty [60]. This method allows detailed investigation of the flaring periods, since at times of a high source flux, the time bins are narrower than during lower flux levels, therefore the rapid changes of the flux can be found. In order to reach the necessary relative flux uncertainty, the integral fluxes are computed above the optimal energies [60] which correspond to  $E_0 = 215.4 \text{ MeV}$  in this case.

Adaptively binned light curves in the 215 MeV-300 GeV energy range with 20% and 15% uncertainties have been generated. Flare is present in both light curves. The light curve with 20% flux uncertainty at each bin is presented in Fig. 6.2 (b) with red color. It confirms all the features visible in the constant-bin-width light curve, but also allows us to investigate fast variability during

high-flux states in greater detail. The first flare episode occurred during MJD 57043.30-57049.38, when the time width was less than  $\sim 15$  hours. A strong flaring period is observed around the 24th-25th of January. The flux peak of  $(1.14 \pm 0.24) \times 10^{-6} \text{ photon cm}^{-2} \text{ s}^{-1}$  was observed on the 24th of January at 22:35 *pm* in a bin with a half-width of 3.1 hours. The analysis of the data acquired in the mentioned period on the energies of  $> 100$  MeV results in a flux of  $(2.22 \pm 0.38) \times 10^{-6} \text{ photon cm}^{-2} \text{ s}^{-1}$ , which is the highest photon flux detected from this source. The data analysis for the entire flaring period (January 21-28) resulted in a flux of  $(1.05 \pm 0.06) \times 10^{-6} \text{ photon cm}^{-2} \text{ s}^{-1}$  and a photon index of  $\sim 1.98 \pm 0.04$  [80]. After MJD 57049.38, PKS 1441+25 was in its quiescent state, and the data should be accumulated for more than a day to reach 20 % uncertainty. Then from MJD 57109.89 to MJD 57143.91, PKS 1441+25 was again in its active state which was characterized by emission with a significantly hardened  $\gamma$ -ray photon index. Starting from MJD 57126.70 to MJD 57141.93, the photon index of PKS 1441+25 hardened and reached  $\leq 1.9$  most of the time. Measured within a few hours, the photon index kept varying from  $\Gamma = 1.73$  to  $\Gamma = 1.91$ . The hardest photon index of  $\Gamma = 1.54 \pm 0.16$  was observed on MJD 57131.46 with  $11.8\sigma$  and the data being accumulated for  $\approx 29$  hours. Other periods, when PKS 1441+25 was bright enough to be detected on sub-day scales, are MJD 57177.38- 57199.76 and MJD 57243.02-57249.39. For the rest of the time the source was in its quiescent state and the data should be accumulated for a few days or even longer in order to detect the source. The analysis of the light curve with the new adaptive binning method for the first time allowed us to investigate the flaring activity of PKS 1441+25 with a sub-day resolution and to perform detailed investigation of the flux and photon index changes. Furthermore, to derive the flare doubling timescales and understand the nature of the January flare, the light curve is fitted with an exponential function in the form of [2]

$$F(t) = F_c + F_0 \times \left( e^{\frac{t-t_0}{t_r}} + e^{\frac{t_0-t}{t_d}} \right)^{-1} \quad (6.2.1)$$

where  $t_0$  is the time of the maximum intensity of the flare ( $F_0$ ),  $F_c$  is the constant level present in the flare,  $t_r$  and  $t_d$  are the rise and decay time constants, respectively. The fit shows that the flare is best explained when  $t_0 = 57048.25 \pm 0.18$ ,  $t_r = 1.92 \pm 0.3$ ,  $t_d = 0.72 \pm 0.1$  and  $F_0 = (22.6 \pm 1.4) \times 10^{-7} \text{ photon cm}^{-2} \text{ s}^{-1}$ . The fit of the flaring period is shown in Fig. 6.3 with

a dashed red line. Using this technique, it is also possible to estimate the shortest time variability (flux doubling) defined by  $\tau = 2t_{r,d}$ , corresponding to  $\tau = 1.44$  days which is used to put an important constraint on the radiative region size. We note that the previous PKS 1441+25  $\gamma$ -ray emission studies with the Fermi LAT data that covered only the period in April did not allow to properly estimate the  $\gamma$ -ray emitting region size, while here the analysis of the flaring period in January allowed to constrain the flare doubling time which is necessary for constraining the  $\gamma$ -ray emission region size.

## 6.3 BROADBAND SED MODELLING

It is hard to make theoretical modeling of the observed broadband SED because the structure of the central region of blazars is complex and the exact localization of emitting regions is unknown. The observed fast variability indicates compactness of the emitting region but its localization remains an open problem. Along the jet, the emission can be produced in different zones and depending on the distance from the central black hole different components can contribute to the observed emission [87].

### 6.3.1 Broadband SED

The broadband SEDs of PKS 1441+25 for different periods are shown in Fig. 6.4 where with red and blue colors are the SED observed in January and April respectively, while the archival data from ASI science data center<sup>2</sup> are shown with gray color. We note that during the high states, the second emission peak increased by intensity and shifted to HEs. This kind of change has already been observed during the flaring state of 4C+49.22 [25] and PKS 1510-089 [1]. During the flaring periods the low-energy component's intensity increased as compared with the quiescent state; the increase in April exceeded that one observed in January (although the power-law photon index in the X-ray band ( $\approx 2.3$ ) had been relatively constant during both observations). More evident and drastic is the change of the peak intensity of the low energy component; from January to April it increased by nearly an order of magnitude and as compared with the quiescent state it increased  $\geq 15$  times. On the contrary, the peak of the second component (in the HE  $\gamma$ -ray band) is relatively con-

---

<sup>2</sup><http://tools.asdc.asi.it/SED/index.jsp>

stant, only the photon index in the MeV-GeV energy range is harder during the observations in April. The Compton dominance of the source is stronger and evident during the flaring periods which suggests that the density of the external photon fields significantly exceeds the synchrotron photon density ( $U_{ext}/U_{syn} \gg 1$ ).

Such a strong amplification of the emission from blazars can be explained by means of introducing changes in the emission region parameters, e.g., in the magnetic field, emitting region size, bulk Lorentz factor and others, and/or particle energy distribution. In principle, all the parameters describing the emitting region can be changed at the same time if the flares are due to a global change in the physical processes in the jet, which also affect the jet dynamics and properties. However, usually, the change in one or two parameters is enough to explain the flares. An interesting study of the flaring activity in FSRQs as a result of changes in different parameters has been investigated in [72]. Namely, the emission spectra evolution as a function of changes in different parameters (e.g., bulk Lorentz factor, magnetic field, accretion rate, etc.) is investigated. In the case of PKS 1441+25, during its flaring periods, both the low energy and HE components increased several times. The increase of the second component is most likely due to moving of the emitting region outside its BLR. In principle, there are two possibilities: i) either the emitting region moves faster due to increasing bulk Lorentz factor and leaves the BLR or ii) the bulk Lorentz factor is unchanged and only the emitting region is moving beyond the BLR. In the first case, since the external photon density in the comoving frame of the jet depends on the Doppler boosting factor, a strong increase in the Compton dominance will be observed. We note that the change of the bulk Lorentz factor will also affect the low energy component. In the second case, the flaring activity is due to the change of the location of the emitting region and due to the magnetic field amplification. Additional increase of the magnetic field from January to April is also evident when the low energy component kept increasing (this corresponds to the case shown in Fig. 1 (b) in [72]). Accordingly, we discuss two possibilities. First, we assume that  $\delta$  has increased from 10 in the quiescent to 18 in the flaring periods, and then we assume that it was constant ( $\delta = 18$ ) in both periods. These values are below and above the estimated mean bulk Lorentz factor of FSRQs obtained from the analysis of a large sample of  $\gamma$ -ray emitting FSRQs [38]. The emission region size can be estimated through the observed variability time scale  $\tau = 1.44$  d implying that  $R_b \leq \delta c \tau / (1 + z) \approx 3.5 \times 10^{16}$  cm when  $\delta = 18$  and  $R_b = 1.92 \times 10^{16}$  cm when  $\delta = 10$ .

### 6.3.2 Theoretical modeling

We attempt to fit the SEDs in the high states of January and April as well as in the quiescent state. Even if a quiescent state SED is constrained with non-simultaneous data, its modeling provides an insight into the dominant physical processes which are constantly present in the jet but are covered by the flaring components during the high states. We modeled the PKS 1441+25 SED for high and quiescent states in the framework of single-zone leptonic models that include the synchrotron, SSC, and EC processes. The emission region (the "blob"), assumed to be a sphere with a radius of  $R$  which is moving with a bulk Lorentz factor of  $\Gamma$ , carries a magnetic field with an intensity of  $B$  and a population of relativistic electrons. The blob velocity makes a small angle with respect to the line of sight, so the emission is amplified by a relativistic Doppler factor of  $\delta$ . The energy spectrum of the population of electrons in the jet frame, which is responsible for the non-thermal emission is assumed to have a broken power-law shape:

$$N'_e(E'_e) = \begin{cases} N'_0 \left( \frac{E'_e}{m_e c^2} \right)^{-\alpha_1} & E'_{e,\min} \leq E'_e \leq E'_{br} \\ N'_0 \left( \frac{E'_{br}}{m_e c^2} \right)^{\alpha_2 - \alpha_1} \left( \frac{E'_e}{m_e c^2} \right)^{-\alpha_2} & E'_{br} \leq E'_e \leq E'_{e,\max} \end{cases} \quad (6.3.1)$$

where  $N'_0$  is connected with the total electron energy  $U_e = \int_{E'_{\min}}^{E'_{\max}} E'_e N_e(E'_e) dE'_e$ ,  $\alpha_1$  and  $\alpha_2$  are the low and high indexes of electrons correspondingly below and above the break energy  $E'_{br}$ , and  $E'_{\min}$  and  $E'_{\max}$  are the minimum and maximum energies of electrons in the jet frame, respectively. The electron spectrum given in Eq. 6.3.1 is naturally formed from the cooling of relativistic electrons [57, 53].

The low-energy (from radio to optical/X-ray) emission is due to the synchrotron emission of electrons with an energy spectrum as given by Eq. 6.3.1 in a homogeneous and randomly oriented magnetic field. For the quiescent state we assume the energy dissipation occurs close to the central source region and it is explained as an IC scattering of synchrotron photons (SSC). Instead the high state emission is dominated by that from a region well outside the BLR in order to avoid the strong absorption of photons with energies  $\geq 100$  GeV (similar assumptions have been already made in [6, 15]). In this case the dominant external photon field is the IR radiation from the dusty torus which, as we assume, has a blackbody spectrum with a luminosity of

$L_{IR} = \eta L_{disc}$  ( $\eta = 0.6$ , [33]) and a temperature of  $T = 10^3$  K and fills a volume that for simplicity is approximated as a spherical shell with a radius of  $R_{IR} = 3.54 \times 10^{18} (L_{disc}/10^{45})^{0.5}$  cm [69]. The disc luminosity is estimated from the BLR luminosity,  $L_{disc} = 10 \times L_{BLR} \approx 2 \times 10^{45} \text{ erg s}^{-1}$  [94].

### 6.3.3 Fitting technique

In order to constrain the model parameters more efficiently, we employed the MCMC method, which enables to derive the confidence intervals for each model parameter. For the current study we have modified the naima package [95] which derives the best-fit and uncertainty distributions of spectral model parameters through MCMC sampling of their likelihood distributions. The prior likelihood, our prior knowledge of the probability distribution of a given model parameter and the data likelihood functions are passed onto the emcee sampler function for an affine-invariant MCMC run. In addition, there are multiple simultaneous walkers which improve the efficiency of the sampling and reduce the number of computationally expensive likelihood calls. We run the sampling with 64 simultaneous walkers, for 100 steps of burn-in, and 100 steps of run. In the parameter sampling, the following expected ranges are considered:  $1.5 \leq (\alpha_{1,2}) \leq 10$ ,  $0.511 \text{ MeV} \leq E'_{(br, min, max)} \leq 1 \text{ TeV}$ , and  $N_0$  and  $B$  are defined as positive parameters. The synchrotron emission is calculated using the parameterization of the emissivity function of synchrotron radiation in random magnetic fields presented in [13] while the IC emission is computed based on the monochromatic differential cross section of [12].

### 6.3.4 SED modeling and results

The results of SED modeling are shown in Fig. 6.4 with the corresponding parameters in Table 6.2. The radio emission is due to the low-energy electrons which are accumulated for longer periods, that is why, the radio data are treated as an upper limit for the purposes of our modeling. To have an indication of a change in the energetic contents of the jet, as well as of changes in the radiating particle distribution, first we try to fit the SED in a quiescent state which is modeled assuming two different Doppler boosting factors. The gray solid line in Fig. 6.4 shows the synchrotron/SSC emission assuming that the jet Doppler boosting factor is  $\delta = 10$ , and the gray dashed line is the

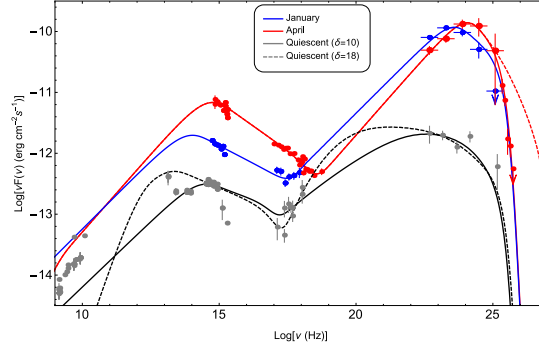


**Figure 6.4:** The broadband SED of PKS 1441+25 for January (red), April (blue) and for the quiescent state (gray). The blue, red and gray lines are the models fitting the data with the electron spectrum given by Eq. 6.3.1 for January, April and for the quiescent state, respectively. The model parameters are presented in Table 6.2. The UV-X-ray and VHE  $\gamma$ -ray data observed in January and April are from [6] and HE  $\gamma$ -ray data (Fermi LAT) are from this work.

**Table 6.2:** Model parameters.

|  | Parameter                               | Quiescent                 | Quiescent                  | January                    | April                    |
|--|---|---------------------------|----------------------------|----------------------------|--------------------------|
| Doppler factor                         | $\delta$                                | 10                        | 18                         | 18                         | 18                       |
| Normalization of electron distribution | $N'_0 \times 10^{48} eV^{-1}$           | $10.68^{+3.09}_{-2.64}$   | $43.44^{+6.59}_{-7.76}$    | $23.83^{+8.11}_{-7.32}$    | $6.12^{+1.67}_{-1.56}$   |
| Low-energy electron spectral index     | $\alpha_1$                              | $2.14 \pm 0.04$           | $2.09^{+0.03}_{-0.04}$     | $2.10^{+0.04}_{-0.05}$     | $1.98 \pm 0.03$          |
| High-energy electron spectral index    | $\alpha_2$                              | $3.39^{+0.27}_{-0.14}$    | $3.38 \pm 0.06$            | $3.46 \pm 0.06$            | $3.64 \pm 0.01$          |
| Minimum electron energy                | $E'_{min}$ (MeV)                        | $1.84^{+1.75}_{-1.23}$    | $286.37^{+30.64}_{-25.39}$ | $1.97^{+0.31}_{-0.34}$     | $4.16^{+1.00}_{-1.86}$   |
| Break electron energy                  | $E'_{br}$ (GeV)                         | $2.83^{+0.51}_{-0.31}$    | $1.11^{+0.14}_{-0.12}$     | $1.62^{+0.23}_{-0.15}$     | $3.11^{+0.15}_{-0.23}$   |
| Maximum electron energy                | $E'_{max}$ (GeV)                        | $46.27^{+49.74}_{-13.76}$ | $82.32^{+13.47}_{-17.14}$  | $127.82^{+26.74}_{-24.75}$ | $202.79^{+21.2}_{-14.6}$ |
| Magnetic field                         | B [G]                                   | $0.19 \pm 0.013$          | $0.046 \pm 0.002$          | $0.11^{+0.005}_{-0.004}$   | $0.18^{+0.009}_{-0.006}$ |
| Jet power in magnetic field            | $L_B \times 10^{43} \text{ erg s}^{-1}$ | 0.49                      | 0.31                       | 1.71                       | 4.51                     |
| Jet power in electrons                 | $L_e \times 10^{45} \text{ erg s}^{-1}$ | 2.11                      | 4.07                       | 9.60                       | 4.47                     |

case of  $\delta = 18$ . In case of  $\delta = 10$ , as the emitting region size is as small as  $R_b = 1.92 \times 10^{16}$  cm, the magnetic field should be as strong as  $B = 0.19$  G to account for the observed data, while at  $\delta = 18$  the magnetic field is much weaker,  $B = 0.046$  G. Also, the underlying electron distribution for the case of  $\delta = 10$  is characterized by a slightly higher break (2.83 GeV versus 1.11 GeV) in order to account for the observed emission.

The emission in flaring periods is modeled assuming that the HE emission is entirely due to the IC scattering of external photons (Fig. 6.4). In all calculations the absorption due to the EBL was taken into account using a model from [28] since a strong absorption is evident at  $\geq 100$  GeV (red dashed line in Fig. 6.4). In both periods the HE electron spectral index is within the range of  $\alpha_2 \sim (3.46 - 3.64)$  which is required to explain the UV-X-ray data with a photon index of  $\approx 2.3$ . The lack of low-energy data makes the precise estimation of the low energy electron index harder. Only the Swift XRT/NuSTAR data from the observation of the transition region between low and high energy components allows to define the parameters  $E_{min}$  and  $\alpha_1$ . The low energy electron index is in a typical range expected from shock acceleration theories,  $\alpha_1 \approx 2$ .

As distinct from the quiescent state, in order to explain the flaring activities, both, the electron distribution and the magnetic field should be varying. We note that the magnetic field required for modeling of flaring periods, ( $B \geq 0.11$  G), is weaker than that one estimated in the quiescent state in case of  $\delta = 10$  ( $B \sim 0.19$  G). Since the synchrotron emission depends on the total number of emitting electrons  $N_e$ ,  $\delta$  and magnetic field strength  $B$ , in case of smaller  $\delta$  (and emitting region size) the magnetic field should be stronger. Instead, when  $\delta$  is constantly equal to 18 in both states, the magnetic field should be nearly  $\sim 2.4$  and  $\sim 3.9$  times stronger in January and April, respectively, in order to explain the observed data. As the synchrotron photon density is proportional to  $B^2$ , the increase in the magnetic field strength resulted in the observed increase of the synchrotron flux by a factor of 5.7 and 15.3 (Fig. 6.4). In the modeling of the SEDs observed in the flaring periods of January and April, the magnetic field should be changed in accordance with the increase in the low energy component. Since the emission in the HE band is dominated by the IC scattering of external photons, this component remains stable during those periods (this corresponds to Fig. 1 (b) [72]).

The electron spectra obtained during the fit of SEDs in quiescent and flaring states are shown in Fig. 6.5. It is clear the evolution of the electron spectra during the quiescent and high states. The low energy indexes of the underly-

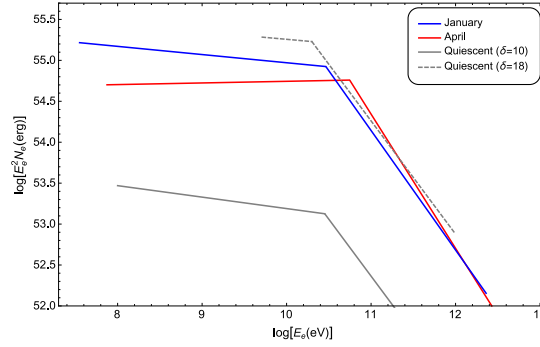


**Figure 6.5:** The electron spectra (broken power laws) obtained from the fit of the quiescent and flaring states of PKS 1441+25. Details on the parameter values are given in Table 6.2.

ing electron distribution in the quiescent state ( $\delta = 10$ ) are softer as compared with the flaring period (April). The total electron energy for modeling the emission in the quiescent period, when  $\delta = 18$ , is almost of the same order as that in the flaring periods, which is expected, as the magnetic field is weaker, most of the jet energy is carried by particles. During the flaring periods, there are evident changes also in the underlying electron distribution. The electron distribution best describing the data observed in April hints at i) hardening of the low energy index, ii) a higher break at  $\sim 3.1$  GeV and maximum energies of  $\sim 203$  GeV.  $E_{br}$  and  $E_{max}$  are expected to shift, as the  $\gamma$ -ray spectrum observed in April is slightly inclined toward HEs, as compared with the January spectrum (see Fig. 6.4). However, due to the large uncertainties in the estimations, especially for  $\alpha_1$  (since the data in between 100 keV and 100 MeV are missing), no definite conclusions can be drawn. For a statistically significant claim for hardening, there are required additional data in the energy range characterizing the rising part of the low and high energy components, which will allow to constrain  $\alpha_1$  with higher confidence. We note, however, that the significant hardening of the  $\gamma$ -ray emission observed in April (Fig. 6.2 (c)) supports and strengthens the assumptions on the hardening of the low energy electron index.

Similar modeling of the SED of PKS 1441+25 observed in April has been already done in [6, 15], but it was done in a different manner. For example, in [15] the low electron energy index is fixed to be  $\alpha_1 = 2$ , a value expected from strong shock acceleration theories, while in our case all the parameters can vary in the fitting procedure. After having observed the hardening of the

$\gamma$ -ray photon index in April, we believe that exact estimation of  $\alpha_1$  is important. Moreover, possible hardening or softening of  $\alpha_1$  would point out the acceleration processes in the jet. However, the main difference in the modeling presented here, as compared with the previous ones, is the size of the emitting region (blob). They used larger blob size,  $5 \times 10^{16}$  cm, in [15] and  $4 \times 10^{17}$  cm in [6]. In our case, the modeling of the January flare time profile allowed us to constrain the emitting region size by  $R_b \leq 3.5 \times 10^{16} (\delta/18)$  cm. Another difference with the previously reported parameters is that in our case the electron energy density is nearly 100 times higher than the magnetic field energy density. In [6]  $U_e/U_B = 1.5$ , which is related to the fact that much bigger emitting region size is used. We note that in [15], where the considered blob size is similar to our case, they also found that  $U_e/U_B \geq 10$ . Moreover, in our case the radius of the IR torus is derived from a different scaling law, which can cause additional difference in the estimation of the total energy. Despite using different approaches and parameters as compared with those used in the previous modelings, we note, that the main parameters for the underlying electron distribution obtained during April are similar to the previously reported values.

## 6.4 DISCUSSION and CONCLUSIONS

In this paper, we present the results of the study of the  $\gamma$ -ray emission from PKS 1441+25 during January-December 2015. The data from the observations of a bright GeV flare in January allow us to estimate the emitting region size whereas the modeling of the broadband SED of PKS 1441+25 in January and April provided a chance to probe into the physical process during the flaring periods.

The  $\gamma$ -ray light curve generated with an adaptive binning method shows that the source entered its high activity state around MJD 57043.3 and the flux reached its maximum on January 24, when, within a few hours, the flux increases up to  $F_\gamma(> 100 \text{ MeV}) = (2.22 \pm 0.38) \times 10^{-6} \text{ photon cm}^{-2} \text{ s}^{-1}$ . During this  $\gamma$ -ray brightening the fit of the flare profile shows a slow rise and a fast decay trend with the shortest variability (flux doubling) time being  $\tau_d = 1.44$  days. The rise of the flare can be attributed to the shock acceleration, whereas the decay phase cannot be explained by cooling of particles. Indeed, for the electrons that emit  $\gamma$ -rays with  $\epsilon_\gamma = 1$  GeV, as measured in the observer frame, the corresponding cooling timescale would then be

$\sim (3 m_e c / \sigma_T u_{IR}) \times (\epsilon_{IR}(1+z)/\epsilon_\gamma)^{0.5}$  [82] which corresponds to 0.47 days in this case. This timescale is shorter than the observed e-folding decay timescales of the flares, implying that the observed flux decrease is related to the processes other than radiative losses.

After the flare on MJD 57049.38, the source is in its quiet state and the next increase in the flux is observed starting from MJD 57109.89. Even if during this period, the flux amplitude is lower than one that observed in January, an interesting modification of the  $\gamma$ -ray emission spectrum is observed. First, the  $\gamma$ -ray photon index hardened during MJD 57126.70-57141.93, it was  $\leq 1.9$ . This period coincides with the one when VHE  $\gamma$ -rays from PKS 1441+25 were detected. The hardest  $\gamma$ -ray photon index,  $\Gamma = 1.54 \pm 0.16$ , has been observed on MJD 57131.46 with a convincingly high detection significance of  $11.8\sigma$ . This photon index is unusual for FSRQs which are with an averaged photon index of 2.4 in the third Fermi LAT AGN catalog (see Fig. 8 of [9]). This photon index is even harder than the index of B3 1151+408 ( $\Gamma = 1.77$ ) which has the hardest photon indexes in the clean sample of Fermi LAT detected FSRQs. Although, hard photon indexes have been occasionally observed during rapid flaring events in FSRQs [71]. The observed hardening was perhaps related to the emission of new energetic particles that were either injected into the emitting region or re-accelerated. Next, the data analysis covering only the period in April shows that the  $\gamma$ -ray flux hints at a spectral curvature and a power-law with an exponential cut-off model is preferred over the simple power-law modeling assuming a break around  $E_{cut} = 17.7 \pm 8.9$  GeV with a significance of  $2.8\sigma$ . Although the low statistics does not allow to claim for a statistically significant curvature in the spectrum, the  $\gamma$ -ray photon index observed in the VHE  $\gamma$ -ray band ( $\sim 5.4$ , which corresponds to an intrinsic index of 3.4 after correction for the EBL) strongly supports the presence of a break or a cut-off in the PKS 1441+25 spectrum around tens of GeV. Most likely, this break is defined by the break present in the radiating electron spectrum rather than is caused by the absorption within BLR [75] (otherwise the photons with  $>100$  GeV would be strongly absorbed).

**The origin of multiwavelength emission:** The SEDs observed during quiescent and flaring states are modeled using one-zone leptonic models and the model parameters are estimated using the MCMC method. The HE  $\gamma$ -ray emission observed in the flaring states can be explained by IC scattering of IR photons from the dusty torus whereas the SSC model gives a satisfactory

representation of the data observed during the quiescent state. The flares observed in January and April can be explained assuming there are changes in the bulk Lorentz factor or in the magnetic field. If the emitting region leaves the BLR region due to the increase of the bulk Lorentz factor (from  $\delta = 10$  to  $\delta = 18$ ), the Compton dominance will increase as it has been observed in the  $\gamma$ -ray band. Indeed in the flaring states, the IC to synchrotron luminosities ratio  $L_\gamma/L_{syn} \approx 200$  and  $\approx 28$  in January and April, respectively as compared with that in the quiescent state  $L_\gamma/L_{syn} \approx (2 - 4)$ . At the same time, the increase in the low energy component indicates that the magnetic field also increased between the flares in January and April [72]. On the other hand, if the bulk Lorentz factor is unchanged ( $\delta = 18$ ), only the change in the emitting region location and amplification of the magnetic field can explain the multifrequency behavior observed during the flares. It is possible to distinguish between these two scenarios, provided there are data in the hard X-ray or soft  $\gamma$ -ray band, as the modeling with  $\delta = 18$  predicts a higher flux in the hard X-ray band than when  $\delta = 10$  is assumed (gray dashed and solid lines in Fig. 6.2). Such data are missing in this case, making it hard to give exact interpretation of the origin of the flare. Anyway, physically reasonable parameters are used in both of these scenarios.

When comparing the electron parameters required for the modeling of the SEDs in January and April, we find a hint of possible hardening of the low energy electron index in April. We note, however, that no definite conclusions can be drawn since  $\alpha_1$  is poorly constrained (due to missing or nonsufficient data). For all that, the April hardening of the  $\gamma$ -ray photon index in the MeV-GeV energy region supports our assumptions on hardening of the power-law index of the underlying electron distribution.

**Jet Energetics:** The jet power in the form of magnetic field and electron kinetic energy are calculated by  $L_B = \pi c R_b^2 \Gamma^2 U_B$  and  $L_e = \pi c R_b^2 \Gamma^2 U_e$ , respectively, and are given in Table 6.2. The jet power in the electrons changes in the range  $(4.5 - 9.6) \times 10^{45} \text{ erg s}^{-1}$  during the flares, while in the quiescent state it is of the order of  $(2.1 - 4.1) \times 10^{45} \text{ erg s}^{-1}$ . Assuming one proton per relativistic electron (e.g., [23, 30]), the total kinetic energy in the jet is  $L_{kin} = 8.02 \times 10^{47} \text{ erg s}^{-1}$  and  $L_{kin} = 1.35 \times 10^{47} \text{ erg s}^{-1}$  for January and April, respectively.

The maximum  $\gamma$ -ray flux during the period of high activity is  $(2.22 \pm 0.38) \times 10^{-6} \text{ photon cm}^{-2} \text{ s}^{-1}$  which corresponds to an isotropic  $\gamma$ -ray luminosity

of  $L_\gamma = 1.22 \times 10^{49} \text{ erg s}^{-1}$  (using a distance of  $d_L \approx 6112.8 \text{ Mpc}$ ). Likewise, the  $\gamma$ -ray luminosities in the periods of January and April were  $L_\gamma = 3.48 \times 10^{48} \text{ erg s}^{-1}$  and  $L_\gamma = 5.21 \times 10^{48} \text{ erg s}^{-1}$ , respectively. Yet, at  $\delta = 18$  the total power emitted in the  $\gamma$ -ray band in the proper frame of the jet would be  $L_{em,\gamma} = L_\gamma/2 \delta^2 = 1.89 \times 10^{46} \text{ erg s}^{-1}$  during the peak flux and would change within  $L_{em,\gamma} = (5.38 - 8.04) \times 10^{45} \text{ erg s}^{-1}$  in January and April. These luminosity values account for only a small fraction ( $\leq 6.7\%$ ) of the total kinetic energy of the jet. However, assuming that the standard radiative efficiency of the accretion disc  $\eta_{disc} \sim 10\%$ , the accretion power would be  $L_{acc} = 2 \times 10^{46} \text{ erg s}^{-1}$ . Thus during the flaring period the power emitted as  $\gamma$ -ray photons constitutes the bulk of the total accretion power  $L_{em,\gamma}/L_{acc} \approx 1$ , while in January and April it made a substantial fraction of it -  $L_{em,\gamma}/L_{acc} \approx (0.3 - 0.4)$ ; this is in a good agreement with the recent results by [39], which showed that the radiative jet power in blazars is higher than (or of the order of) the accretion disk luminosity.

The observations in both X-ray and  $\gamma$ -ray bands show that after the activity observed in January and April the emission from the source again enters a quiescent state. A small increase in the  $\gamma$ -ray flux has been observed only in June, August and October-November 2015. Also, the UV/X-ray flux measured by Swift in May 2015 [6] shows that the synchrotron component is weaker than it was in April. Thus, this indicates that the magnetic field in the emitting region started to decrease. In addition, in the  $\gamma$ -ray band, the flux slowly decreases down to a few times  $10^{-7} \text{ photon cm}^{-2} \text{ s}^{-1}$  for most of the time after August 2015, and the  $\gamma$ -ray photon index reaches its mean level. These point out that the emission from the blob outside the BLR region weakened, and the decrease of the Compton component shows that the emission responsible for the emission in the quiescent state (SSC) starts to dominate again. Since in this case the emission occurs close to the central source, due to the strong absorption, it is not expected to have emission of VHE  $\gamma$ -ray photons.

The multiwavelength observations of PKS 1441+25 during the flaring periods allowed us to investigate and discuss the changes that possibly took place in the jets and caused flaring activities. However, the parameters describing the underlying electron distribution below the break are poorly constrained, because the data describing the rising part of both low and HE components are missing. It did not allow us to exactly identify the processes responsible for the acceleration of particles in the jet. However, the future possible observa-

tions of flaring periods also in other energy bands will provide a chance to investigate the dominant particle acceleration processes.



# Bibliography

- [1] A. A. Abdo, M. Ackermann, I. Agudo, M. Ajello, A. Allafort, H. D. Aller, M. F. Aller, E. Antolini, A. A. Arkharov, M. Axelsson, and et al. Fermi Large Area Telescope and Multi-wavelength Observations of the Flaring Activity of PKS 1510-089 between 2008 September and 2009 June. *ApJ*, 721:1425–1447, October 2010.
- [2] A. A. Abdo, M. Ackermann, M. Ajello, E. Antolini, L. Baldini, J. Ballet, G. Barbiellini, D. Bastieri, K. Bechtol, R. Bellazzini, B. Berenji, R. D. Blandford, E. D. Bloom, E. Bonamente, A. W. Borgland, A. Bouvier, J. Bregeon, A. Brez, M. Brigida, P. Bruel, R. Buehler, T. H. Burnett, S. Buson, G. A. Caliandro, R. A. Cameron, P. A. Caraveo, S. Carri-gan, J. M. Casandjian, E. Cavazzuti, C. Cecchi, Ö. Çelik, A. Chekht-man, C. C. Cheung, J. Chiang, S. Ciprini, R. Claus, J. Cohen-Tanugi, L. R. Cominsky, J. Conrad, L. Costamante, S. Cutini, C. D. Dermer, A. de Angelis, F. de Palma, E. d. C. e. Silva, P. S. Drell, R. Dubois, D. Dumora, C. Farnier, C. Favuzzi, S. J. Fegan, W. B. Focke, P. Fortin, M. Frailis, Y. Fukazawa, S. Funk, P. Fusco, F. Gargano, D. Gasparrini, N. Gehrels, S. Germani, B. Giebels, N. Giglietto, P. Giommi, F. Gior-dano, T. Glanzman, G. Godfrey, I. A. Grenier, M.-H. Grondin, J. E. Grove, S. Guiriec, D. Hadasch, M. Hayashida, E. Hays, S. E. Healey, D. Horan, R. E. Hughes, R. Itoh, G. Jóhannesson, A. S. Johnson, W. N. Johnson, T. Kamae, H. Katagiri, J. Kataoka, N. Kawai, J. Knödlse-dler, M. Kuss, J. Lande, S. Larsson, L. Latronico, M. Lemoine-Goumard, F. Longo, F. Loparco, B. Lott, M. N. Lovellette, P. Lubrano, G. M. Madejski, A. Makeev, E. Massaro, M. N. Mazziotta, J. E. McEnery, P. F. Michelson, W. Mitthumsiri, T. Mizuno, A. A. Moiseev, C. Monte, M. E. Monzani, A. Morselli, I. V. Moskalenko, M. Mueller, S. Murgia, P. L. Nolan, J. P. Norris, E. Nuss, M. Ohno, T. Ohsugi, N. Omodei, E. Orlando, J. F. Ormes, M. Ozaki, J. H. Panetta, D. Parent, V. Pelassa, M. Pepe, M. Pesce-Rollins, F. Piron, T. A. Porter, S. Rainò, R. Rando,

M. Razzano, A. Reimer, O. Reimer, S. Ritz, A. Y. Rodriguez, R. W. Romani, M. Roth, F. Ryde, H. F.-W. Sadrozinski, A. Sander, J. D. Scargle, C. Sgrò, M. S. Shaw, P. D. Smith, G. Spandre, P. Spinelli, J.-L. Starck, M. S. Strickman, D. J. Suson, H. Takahashi, T. Takahashi, T. Tanaka, J. B. Thayer, J. G. Thayer, D. J. Thompson, L. Tibaldo, D. F. Torres, G. Tosti, A. Tramacere, Y. Uchiyama, T. L. Usher, V. Vasileiou, N. Vilchez, V. Vitale, A. P. Waite, E. Wallace, P. Wang, B. L. Winer, K. S. Wood, Z. Yang, T. Ylinen, and M. Ziegler.

Gamma-ray Light Curves and Variability of Bright Fermi-detected Blazars.

*ApJ*, 722:520–542, October 2010.

- [3] A. A. Abdo, M. Ackermann, M. Ajello, W. B. Atwood, M. Axelsson, L. Baldini, J. Ballet, G. Barbiellini, D. Bastieri, K. Bechtol, R. Bellazzini, B. Berenji, R. D. Blandford, E. D. Bloom, E. Bonamente, A. W. Borgland, J. Bregeon, A. Brez, M. Brigida, P. Bruel, T. H. Burnett, G. A. Caliandro, R. A. Cameron, A. Cannon, P. A. Caraveo, J. M. Casandjian, E. Cavazzuti, C. Cecchi, Ö. Çelik, E. Charles, C. C. Cheung, J. Chiang, S. Ciprini, R. Claus, J. Cohen-Tanugi, S. Colafrancesco, J. Conrad, L. Costamante, S. Cutini, D. S. Davis, C. D. Dermer, A. de Angelis, F. de Palma, S. W. Digel, D. Donato, E. d. C. e. Silva, P. S. Drell, R. Dubois, D. Dumora, Y. Edmonds, C. Farnier, C. Favuzzi, S. J. Fegan, J. Finke, W. B. Focke, P. Fortin, M. Frailis, Y. Fukazawa, S. Funk, P. Fusco, F. Gargano, D. Gasparrini, N. Gehrels, M. Georganopoulos, S. Germani, B. Giebels, N. Giglietto, P. Giommi, F. Giordano, M. Giroletti, T. Glanzman, G. Godfrey, I. A. Grenier, M.-H. Grondin, J. E. Grove, L. Guillemot, S. Guiriec, Y. Hanabata, A. K. Harding, M. Hayashida, E. Hays, D. Horan, G. Jóhannesson, A. S. Johnson, R. P. Johnson, T. J. Johnson, W. N. Johnson, T. Kamae, H. Katagiri, J. Kataoka, N. Kawai, M. Kerr, J. Knödlseeder, M. L. Kocian, M. Kuss, J. Lande, L. Latronico, M. Lemoine-Goumard, F. Longo, F. Loparco, B. Lott, M. N. Lovellette, P. Lubrano, G. M. Madejski, A. Makeev, M. N. Mazziotta, W. McConville, J. E. McEnery, C. Meurer, P. F. Michelson, W. Mitthumsiri, T. Mizuno, A. A. Moiseev, C. Monte, M. E. Monzani, A. Morselli, I. V. Moskalenko, S. Murgia, P. L. Nolan, J. P. Norris, E. Nuss, T. Ohsugi, N. Omodei, E. Orlando, J. F. Ormes, M. Ozaki, D. Paneque, J. H. Panetta, D. Parent, V. Pelassa, M. Pepe, M. Pesce-Rollins, F. Piron, T. A. Porter, S. Rainò,

---

R. Rando, M. Razzano, A. Reimer, O. Reimer, T. Reposeur, S. Ritz, L. S. Rochester, A. Y. Rodriguez, R. W. Romani, M. Roth, F. Ryde, H. F.-W. Sadrozinski, R. Sambruna, D. Sanchez, A. Sander, P. M. Saz Parkinson, J. D. Scargle, C. Sgrò, M. S. Shaw, D. A. Smith, P. D. Smith, G. Spandre, P. Spinelli, M. S. Strickman, D. J. Suson, H. Tajima, H. Takahashi, T. Tanaka, G. B. Taylor, J. B. Thayer, D. J. Thompson, L. Tibaldo, D. F. Torres, G. Tosti, A. Tramacere, Y. Uchiyama, T. L. Usher, V. Vasileiou, N. Vilchez, A. P. Waite, P. Wang, B. L. Winer, K. S. Wood, T. Ylinen, M. Ziegler, D. E. Harris, F. Massaro, and Ł. Stawarz. Fermi Large Area Telescope Gamma-Ray Detection of the Radio Galaxy M87. *ApJ*, 707:55–60, December 2009.

- [4] A. A. Abdo, M. Ackermann, M. Ajello, L. Baldini, J. Ballet, G. Barbiellini, D. Bastieri, K. Bechtol, R. Bellazzini, B. Berenji, R. D. Blandford, E. D. Bloom, E. Bonamente, A. W. Borgland, A. Bouvier, T. J. Brandt, J. Bregeon, A. Brez, M. Brigida, P. Bruel, R. Buehler, T. H. Burnett, S. Buson, G. A. Caliandro, R. A. Cameron, A. Cannon, P. A. Caraveo, S. Carri- gan, J. M. Casandjian, E. Cavazzuti, C. Cecchi, Ö. Çelik, A. Celotti, E. Charles, A. Chekhtman, A. W. Chen, C. C. Cheung, J. Chiang, S. Ciprini, R. Claus, J. Cohen-Tanugi, S. Colafrancesco, J. Conrad, D. S. Davis, C. D. Dermer, A. de Angelis, F. de Palma, E. d. C. e. Silva, P. S. Drell, R. Dubois, C. Favuzzi, S. J. Fegan, E. C. Ferrara, P. Fortin, M. Frailis, Y. Fukazawa, P. Fusco, F. Gargano, D. Gaspar- rini, N. Gehrels, S. Germani, N. Giglietto, P. Giommi, F. Giordano, M. Giroletti, T. Glanzman, G. Godfrey, P. Grandi, I. A. Grenier, J. E. Grove, L. Guillemot, S. Guiriec, D. Hadasch, M. Hayashida, E. Hays, D. Horan, R. E. Hughes, M. S. Jackson, G. Jóhannesson, A. S. John- son, W. N. Johnson, T. Kamae, H. Katagiri, J. Kataoka, J. Knödlse- der, M. Kuss, J. Lande, L. Latronico, S.-H. Lee, M. Lemoine-Goumard, M. Llana Garde, F. Longo, F. Loparco, B. Lott, M. N. Lovellette, P. Lu- brano, G. M. Madejski, A. Makeev, G. Malaguti, M. N. Mazziotta, W. McConville, J. E. McEnery, P. F. Michelson, G. Migliori, W. Mit- thumsiri, T. Mizuno, C. Monte, M. E. Monzani, A. Morselli, I. V. Moskalenko, S. Murgia, M. Naumann-Godo, I. Nestoras, P. L. Nolan, J. P. Norris, E. Nuss, T. Ohsugi, A. Okumura, N. Omodei, E. Orlando, J. F. Ormes, D. Paneque, J. H. Panetta, D. Parent, V. Pelassa, M. Pepe, M. Persic, M. Pesce-Rollins, F. Piron, T. A. Porter, S. Rainò, R. Rando,

M. Razzano, S. Razzaque, A. Reimer, O. Reimer, L. C. Reyes, M. Roth, H. F.-W. Sadrozinski, D. Sanchez, A. Sander, J. D. Scargle, C. Sgrò, E. J. Siskind, P. D. Smith, G. Spandre, P. Spinelli, Ł. Stawarz, F. W. Stecker, M. S. Strickman, D. J. Suson, H. Takahashi, T. Tanaka, J. B. Thayer, J. G. Thayer, D. J. Thompson, L. Tibaldo, D. F. Torres, E. Torresi, G. Tosti, A. Tramacere, Y. Uchiyama, T. L. Usher, J. Vandenbroucke, V. Vasileiou, N. Vilchez, M. Villata, V. Vitale, A. P. Waite, P. Wang, B. L. Winer, K. S. Wood, Z. Yang, T. Ylinen, and M. Ziegler. Fermi Large Area Telescope Observations of Misaligned Active Galactic Nuclei. *ApJ*, 720:912–922, September 2010.

- [5] A. A. Abdo, M. Ackermann, M. Ajello, L. Baldini, J. Ballet, G. Barbiellini, D. Bastieri, K. Bechtol, R. Bellazzini, B. Berenji, R. D. Blandford, E. D. Bloom, E. Bonamente, A. W. Borgland, A. Bouvier, T. J. Brandt, J. Bregeon, A. Brez, M. Brigida, P. Bruel, R. Buehler, T. H. Burnett, S. Buson, G. A. Caliandro, R. A. Cameron, A. Cannon, P. A. Caraveo, S. Carri- gan, J. M. Casandjian, E. Cavazzuti, C. Cecchi, Ö. Çelik, A. Celotti, E. Charles, A. Chekhtman, A. W. Chen, C. C. Cheung, J. Chiang, S. Ciprini, R. Claus, J. Cohen-Tanugi, S. Colafrancesco, J. Conrad, D. S. Davis, C. D. Dermer, A. de Angelis, F. de Palma, E. d. C. e. Silva, P. S. Drell, R. Dubois, C. Favuzzi, S. J. Fegan, E. C. Ferrara, P. Fortin, M. Frailis, Y. Fukazawa, P. Fusco, F. Gargano, D. Gaspar- rini, N. Gehrels, S. Germani, N. Giglietto, P. Giommi, F. Giordano, M. Giroletti, T. Glanzman, G. Godfrey, P. Grandi, I. A. Grenier, J. E. Grove, L. Guillemot, S. Guiriec, D. Hadasch, M. Hayashida, E. Hays, D. Horan, R. E. Hughes, M. S. Jackson, G. Jóhannesson, A. S. John- son, W. N. Johnson, T. Kamae, H. Katagiri, J. Kataoka, J. Knödlse- der, M. Kuss, J. Lande, L. Latronico, S.-H. Lee, M. Lemoine-Goumard, M. Llena Garde, F. Longo, F. Loparco, B. Lott, M. N. Lovellette, P. Lu- brano, G. M. Madejski, A. Makeev, G. Malaguti, M. N. Mazziotta, W. McConville, J. E. McEnery, P. F. Michelson, G. Migliori, W. Mit- thumsiri, T. Mizuno, C. Monte, M. E. Monzani, A. Morselli, I. V. Moskalenko, S. Murgia, M. Naumann-Godo, I. Nestoras, P. L. Nolan, J. P. Norris, E. Nuss, T. Ohsugi, A. Okumura, N. Omodei, E. Orlando, J. F. Ormes, D. Paneque, J. H. Panetta, D. Parent, V. Pelassa, M. Pepe, M. Persic, M. Pesce-Rollins, F. Piron, T. A. Porter, S. Rainò, R. Rando, M. Razzano, S. Razzaque, A. Reimer, O. Reimer, L. C. Reyes, M. Roth,

- H. F.-W. Sadrozinski, D. Sanchez, A. Sander, J. D. Scargle, C. Sgrò, E. J. Siskind, P. D. Smith, G. Spandre, P. Spinelli, Ł. Stawarz, F. W. Stecker, M. S. Strickman, D. J. Suson, H. Takahashi, T. Tanaka, J. B. Thayer, J. G. Thayer, D. J. Thompson, L. Tibaldo, D. F. Torres, E. Torresi, G. Tosti, A. Tramacere, Y. Uchiyama, T. L. Usher, J. Vandenbroucke, V. Vasileiou, N. Vilchez, M. Villata, V. Vitale, A. P. Waite, P. Wang, B. L. Winer, K. S. Wood, Z. Yang, T. Ylinen, and M. Ziegler. Fermi Large Area Telescope View of the Core of the Radio Galaxy Centaurus A. *ApJ*, 719:1433–1444, August 2010.
- [6] A. U. Abeysekara, S. Archambault, A. Archer, T. Aune, A. Barnacka, W. Benbow, R. Bird, J. Biteau, J. H. Buckley, V. Bugaev, J. V. Cardenzana, M. Cerruti, X. Chen, J. L. Christiansen, L. Ciupik, M. P. Connolly, P. Coppi, W. Cui, H. J. Dickinson, J. Dumm, J. D. Eisch, M. Errando, A. Falcone, Q. Feng, J. P. Finley, H. Fleischhack, A. Flinders, P. Fortin, L. Fortson, A. Furniss, G. H. Gillanders, S. Griffin, J. Grube, G. Gyuk, M. Hütten, N. HA&Akansson, D. Hanna, J. Holder, T. B. Humensky, C. A. Johnson, P. Kaaret, P. Kar, N. Kelley-Hoskins, Y. Khassen, D. Kieda, M. Krause, F. Krennrich, S. Kumar, M. J. Lang, G. Maier, S. McArthur, A. McCann, K. Meagher, P. Moriarty, R. Mukherjee, D. Nieto, A. O’Faoláin de Bhróithe, R. A. Ong, A. N. Otte, N. Park, J. S. Perkins, A. Petrashyk, M. Pohl, A. Popkow, E. Pueschel, J. Quinn, K. Ragan, G. Ratliff, P. T. Reynolds, G. T. Richards, E. Roache, J. Rousselle, M. Santander, G. H. Sembroski, K. Shahinyan, A. W. Smith, D. Staszak, I. Telezhinsky, N. W. Todd, J. V. Tucci, J. Tyler, V. V. Vassiliev, S. Vincent, S. P. Wakely, O. M. Weiner, A. Weinstein, A. Wilhelm, D. A. Williams, B. Zitzer, VERITAS, P. S. Smith, SPOL, T. W.-S. Holoien, J. L. Prieto, C. S. Kochanek, K. Z. Stanek, B. Shappee, ASAS-SN, T. Hovatta, W. Max-Moerbeck, T. J. Pearson, R. A. Reeves, J. L. Richards, A. C. S. Readhead, OVRO, G. M. Madejski, NuSTAR, S. G. Djorgovski, A. J. Drake, M. J. Graham, A. Mahabal, and CRTS. Gamma-Rays from the Quasar PKS 1441+25: Story of an Escape. *ApJL*, 815:L22, December 2015.
- [7] F. Acero, M. Ackermann, M. Ajello, and et al. Fermi Large Area Telescope Third Source Catalog.

*ApJSS*, 218:23, June 2015.

- [8] M. Ackermann, M. Ajello, W. B. Atwood, L. Baldini, J. Ballet, G. Barbiellini, D. Bastieri, J. Becerra Gonzalez, R. Bellazzini, E. Bissaldi, R. D. Blandford, E. D. Bloom, R. Bonino, E. Bottacini, T. J. Brandt, J. Bregeon, R. J. Britto, P. Bruel, R. Buehler, S. Buson, G. A. Caliandro, R. A. Cameron, M. Caragiulo, P. A. Caraveo, B. Carpenter, J. M. Casandjian, E. Cavazzuti, C. Cecchi, E. Charles, A. Chekhtman, C. C. Cheung, J. Chiang, G. Chiaro, S. Ciprini, R. Claus, J. Cohen-Tanugi, L. R. Cominsky, J. Conrad, S. Cutini, R. D'Abrusco, F. D'Ammando, A. de Angelis, R. Desiante, S. W. Digel, L. Di Venere, P. S. Drell, C. Favuzzi, S. J. Fegan, E. C. Ferrara, J. Finke, W. B. Focke, A. Franckowiak, L. Fuhrmann, Y. Fukazawa, A. K. Furniss, P. Fusco, F. Gargano, D. Gasparrini, N. Giglietto, P. Giommi, F. Giordano, M. Giroletti, T. Glanzman, G. Godfrey, I. A. Grenier, J. E. Grove, S. Guiriec, J. W. Hewitt, A. B. Hill, D. Horan, R. Itoh, G. Jóhannesson, A. S. Johnson, W. N. Johnson, J. Kataoka, T. Kawano, F. Krauss, M. Kuss, G. La Mura, S. Larsson, L. Latronico, C. Leto, J. Li, L. Li, F. Longo, F. Loparco, B. Lott, M. N. Lovellette, P. Lubrano, G. M. Madejski, M. Mayer, M. N. Mazziotta, J. E. McEnery, P. F. Michelson, T. Mizuno, A. A. Moiseev, M. E. Monzani, A. Morselli, I. V. Moskalenko, S. Murgia, E. Nuss, M. Ohno, T. Ohsugi, R. Ojha, N. Omodei, M. Orienti, E. Orlando, A. Paggi, D. Paneque, J. S. Perkins, M. Pesce-Rollins, F. Piron, G. Pivato, T. A. Porter, S. Rainò, R. Rando, M. Razzano, S. Razzaque, A. Reimer, O. Reimer, R. W. Romani, D. Salvetti, M. Schaal, F. K. Schinzel, A. Schulz, C. Sgrò, E. J. Siskind, K. V. Sokolovsky, F. Spada, G. Spandre, P. Spinelli, L. Stawarz, D. J. Suson, H. Takahashi, T. Takahashi, Y. Tanaka, J. G. Thayer, J. B. Thayer, L. Tibaldo, D. F. Torres, E. Torresi, G. Tosti, E. Troja, Y. Uchiyama, G. Vianello, B. L. Winer, K. S. Wood, and S. Zimmer.

The Third Catalog of Active Galactic Nuclei Detected by the Fermi Large Area Telescope.

*ApJ*, 810:14, September 2015.

- [9] M. Ackermann, M. Ajello, and et al.

The Third Catalog of Active Galactic Nuclei Detected by the Fermi Large Area Telescope.

*ApJ*, 810:14, September 2015.

- 
- [10] F. Aharonian, A. G. Akhperjanian, A. R. Bazer-Bachi, B. Behera, M. Beilicke, W. Benbow, D. Berge, K. Bernlöhr, C. Boisson, O. Bolz, V. Borrel, T. Boutelier, I. Braun, E. Brion, A. M. Brown, R. Bühler, I. Büsching, T. Bulik, S. Carrigan, P. M. Chadwick, A. C. Clapson, L.-M. Chounet, G. Coignet, R. Cornils, L. Costamante, B. Degrange, H. J. Dickinson, A. Djannati-Ataï, W. Domainko, L. O. Drury, G. Dubus, J. Dyks, K. Egberts, D. Emmanoulopoulos, P. Espigat, C. Farnier, F. Feinstein, A. Fiasson, A. Förster, G. Fontaine, S. Funk, S. Funk, M. Füßling, Y. A. Gallant, B. Giebels, J. F. Glicenstein, B. Glück, P. Goret, C. Hadjichristidis, D. Hauser, M. Hauser, G. Heinzlmann, G. Henri, G. Hermann, J. A. Hinton, A. Hoffmann, W. Hofmann, M. Holleran, S. Hoppe, D. Horns, A. Jacholkowska, O. C. de Jager, E. Kendziorra, M. Kerschhaggl, B. Khélifi, N. Komin, K. Kosack, G. Lamanna, I. J. Latham, R. Le Gallou, A. Lemièrre, M. Lemoine-Goumard, J.-P. Lenain, T. Lohse, J. M. Martin, O. Martineau-Huynh, A. Marcowith, C. Masterson, G. Maurin, T. J. L. McComb, R. Moderski, E. Moulin, M. de Naurois, D. Nedbal, S. J. Nolan, J.-P. Olive, K. J. Orford, J. L. Osborne, M. Ostrowski, M. Panter, G. Pedalletti, G. Pelletier, P.-O. Petrucci, S. Pita, G. Pühlhofer, M. Punch, S. Ranchon, B. C. Raubenheimer, M. Raue, S. M. Rayner, M. Renaud, J. Ripken, L. Rob, L. Rolland, S. Rosier-Lees, G. Rowell, B. Rudak, J. Ruppel, V. Sahakian, A. Santangelo, L. Saugé, S. Schlenker, R. Schlickeiser, R. Schröder, U. Schwanke, S. Schwarzbürg, S. Schwemmer, A. Shalchi, H. Sol, D. Spangler, Ł. Stawarz, R. Steenkamp, C. Stegmann, G. Superina, P. H. Tam, J.-P. Tavernet, R. Terrier, C. van Eldik, G. Vasileiadis, C. Venter, J. P. Vialle, P. Vincent, M. Vivier, H. J. Völk, F. Volpe, S. J. Wagner, M. Ward, and A. A. Zdziarski.  
An Exceptional Very High Energy Gamma-Ray Flare of PKS 2155-304.  
*ApJL*, 664:L71–L74, August 2007.
- [11] F. A. Aharonian.  
Proton-synchrotron radiation of large-scale jets in active galactic nuclei.  
*MNRAS*, 332:215–230, May 2002.
- [12] F. A. Aharonian and A. M. Atoyan.  
Compton scattering of relativistic electrons in compact X-ray sources.  
*Ap&SS*, 79:321–336, October 1981.
- [13] F. A. Aharonian, S. R. Kelner, and A. Y. Prosekin.

Angular, spectral, and time distributions of highest energy protons and associated secondary gamma rays and neutrinos propagating through extragalactic magnetic and radiation fields.

*Phys. Rev. D*, 82(4):043002, August 2010.

- [14] M. L. Ahnen, S. Ansoldi, L. A. Antonelli, P. Antoranz, C. Arcaro, A. Babic, B. Banerjee, P. Bangale, U. Barres de Almeida, J. A. Barrio, J. Becerra González, W. Bednarek, E. Bernardini, A. Berti, B. Biasuzzi, A. Biland, O. Blanch, S. Bonnefoy, G. Bonnoli, F. Borracci, T. Bretz, S. Buson, A. Carosi, A. Chatterjee, R. Clavero, P. Colin, E. Colombo, J. L. Contreras, J. Cortina, S. Covino, P. Da Vela, F. Dazzi, A. De Angelis, B. De Lotto, E. de Oña Wilhelmi, F. Di Pierro, M. Doert, A. Domínguez, D. Dominis Prester, D. Dorner, M. Doro, S. Einecke, D. Eisenacher Glawion, D. Elsaesser, M. Engelkemeier, V. Fallah Ramazani, A. Fernández-Barral, D. Fidalgo, M. V. Fonseca, L. Font, K. Frantzen, C. Fruck, D. Galindo, R. J. García López, M. Garczarczyk, D. Garrido Terrats, M. Gaug, P. Giammaria, N. Godinović, D. Gora, D. Guberman, D. Hadasch, A. Hahn, M. Hayashida, J. Herrera, J. Hose, D. Hrupec, G. Hughes, W. Idec, K. Kodani, Y. Konno, H. Kubo, J. Kushida, A. La Barbera, D. Lelas, E. Lindfors, S. Lombardi, F. Longo, M. López, R. López-Coto, P. Majumdar, M. Makariev, K. Mallot, G. Maneva, M. Manganaro, K. Mannheim, L. Maraschi, B. Marcote, M. Mariotti, M. Martínez, D. Mazin, U. Menzel, J. M. Miranda, R. Mirzoyan, A. Moralejo, E. Moretti, D. Nakajima, V. Neustroev, A. Niedzwiecki, M. Nieves Rosillo, K. Nilsson, K. Nishijima, K. Noda, L. Nogués, S. Paiano, J. Palacio, M. Palatiello, D. Paneque, R. Paoletti, J. M. Paredes, X. Paredes-Fortuny, G. Pedalletti, M. Peresano, L. Perri, M. Persic, J. Poutanen, P. G. Prada Moroni, E. Prandini, I. Puljak, J. R. Garcia, I. Reichardt, W. Rhode, M. Ribó, J. Rico, T. Saito, K. Satalecka, S. Schroeder, T. Schweizer, S. N. Shore, A. Sillanpää, J. Sitarek, I. Snidaric, D. Sobczynska, A. Stamerra, M. Strzys, T. Surić, L. Takalo, F. Tavecchio, P. Temnikov, T. Terzić, D. Tesaro, M. Teshima, D. F. Torres, T. Toyama, A. Treves, G. Vanzo, V. Verguilov, I. Vovk, J. E. Ward, M. Will, M. H. Wu, R. Zanin, and R. Desiante.

Detection of very high energy gamma-ray emission from the gravitationally lensed blazar QSO B0218+357 with the MAGIC telescopes.

*A&A*, 595:A98, November 2016.

- [15] M. L. Ahnen, S. Ansoldi, L. A. Antonelli, P. Antoranz, A. Babic, B. Banerjee, P. Bangale, U. Barres de Almeida, J. A. Barrio, W. Bednarek, and et al.  
Very High Energy  $\gamma$ -Rays from the Universe's Middle Age: Detection of the  $z = 0.940$  Blazar PKS 1441+25 with MAGIC.  
*ApJL*, 815:L23, December 2015.
- [16] J. Aleksic, S. Ansoldi, and et al.  
Black hole lightning due to particle acceleration at subhorizon scales.  
*Science*, 346:1080–1084, November 2014.
- [17] W. B. Atwood, A. A. Abdo, M. Ackermann, W. Althouse, B. Anderson, M. Axelsson, L. Baldini, J. Ballet, D. L. Band, G. Barbiellini, and et al.  
The Large Area Telescope on the Fermi Gamma-Ray Space Telescope Mission.  
*ApJ*, 697:1071–1102, June 2009.
- [18] W. B. Atwood, A. A. Abdo, M. Ackermann, W. Althouse, B. Anderson, M. Axelsson, L. Baldini, J. Ballet, D. L. Band, G. Barbiellini, and et al.  
The Large Area Telescope on the Fermi Gamma-Ray Space Telescope Mission.  
*ApJ*, 697:1071–1102, June 2009.
- [19] M. Błażejowski, M. Sikora, R. Moderski, and G. M. Madejski.  
Comptonization of Infrared Radiation from Hot Dust by Relativistic Jets in Quasars.  
*ApJ*, 545:107–116, December 2000.
- [20] S. D. Bloom and A. P. Marscher.  
An Analysis of the Synchrotron Self-Compton Model for the Multi-Wave Band Spectra of Blazars.  
*ApJ*, 461:657, April 1996.
- [21] A. A. Breeveld, W. Landsman, S. T. Holland, P. Roming, N. P. M. Kuin, and M. J. Page.  
An Updated Ultraviolet Calibration for the Swift/UVOT.  
In J. E. McEnery, J. L. Racusin, and N. Gehrels, editors, *American Institute of Physics Conference Series*, volume 1358 of *American Institute of Physics Conference Series*, pages 373–376, August 2011.

- [22] C. Casadio, J. L. Gómez, P. Grandi, S. G. Jorstad, A. P. Marscher, M. L. Lister, Y. Y. Kovalev, T. Savolainen, and A. B. Pushkarev.  
The Connection between the Radio Jet and the Gamma-ray Emission in the Radio Galaxy 3C 120.  
*ApJ*, 808:162, August 2015.
- [23] A. Celotti and G. Ghisellini.  
The power of blazar jets.  
*MNRAS*, 385:283–300, March 2008.
- [24] P. S. Coppi and F. A. Aharonian.  
Simultaneous X-Ray and Gamma-Ray Observations of TEV Blazars: Testing Synchro-Compton Emission Models and Probing the Infrared Extragalactic Background.  
*ApJL*, 521:L33–L36, August 1999.
- [25] S. Cutini, S. Ciprini, M. Orienti, A. Tramacere, F. D’Ammando, F. Verrecchia, G. Polenta, L. Carrasco, V. D’Elia, P. Giommi, J. González-Nuevo, P. Grandi, D. Harrison, E. Hays, S. Larsson, A. Lähteenmäki, J. León-Tavares, M. López-Caniego, P. Natoli, R. Ojha, B. Partridge, A. Porras, L. Reyes, E. Recillas, and E. Torresi.  
Radio-gamma-ray connection and spectral evolution in 4C +49.22 (S4 1150+49): the Fermi, Swift and Planck view.  
*MNRAS*, 445:4316–4334, December 2014.
- [26] B. L. Fanaroff and J. M. Riley.  
The morphology of extragalactic radio sources of high and low luminosity.  
*MNRAS*, 167:31P–36P, May 1974.
- [27] J. D. Finke, C. D. Dermer, and M. Böttcher.  
Synchrotron Self-Compton Analysis of TeV X-Ray-Selected BL Lacertae Objects.  
*ApJ*, 686:181–194, October 2008.
- [28] A. Franceschini, G. Rodighiero, and M. Vaccari.  
Extragalactic optical-infrared background radiation, its time evolution and the cosmic photon-photon opacity.  
*A&A*, 487:837–852, September 2008.

- 
- [29] N. Gehrels, G. Chincarini, P. Giommi, K. O. Mason, J. A. Nousek, A. A. Wells, N. E. White, S. D. Barthelmy, D. N. Burrows, L. R. Cominsky, K. C. Hurley, F. E. Marshall, P. Mészáros, P. W. A. Roming, L. Angelini, L. M. Barbier, T. Belloni, S. Campana, P. A. Caraveo, M. M. Chester, O. Citterio, T. L. Cline, M. S. Cropper, J. R. Cummings, A. J. Dean, E. D. Feigelson, E. E. Fenimore, D. A. Frail, A. S. Fruchter, G. P. Garmire, K. Gendreau, G. Ghisellini, J. Greiner, J. E. Hill, S. D. Hunsberger, H. A. Krimm, S. R. Kulkarni, P. Kumar, F. Lebrun, N. M. Lloyd-Ronning, C. B. Markwardt, B. J. Mattson, R. F. Mushotzky, J. P. Norris, J. Osborne, B. Paczynski, D. M. Palmer, H.-S. Park, A. M. Parsons, J. Paul, M. J. Rees, C. S. Reynolds, J. E. Rhoads, T. P. Sasseen, B. E. Schaefer, A. T. Short, A. P. Smale, I. A. Smith, L. Stella, G. Tagliaferrri, T. Takahashi, M. Tashiro, L. K. Townsley, J. Tueller, M. J. L. Turner, M. Vietri, W. Voges, M. J. Ward, R. Willingale, F. M. Zerbi, and W. W. Zhang.  
The Swift Gamma-Ray Burst Mission.  
*ApJ*, 611:1005–1020, August 2004.
- [30] G. Ghisellini, editor.  
*Radiative Processes in High Energy Astrophysics*, volume 873 of *Lecture Notes in Physics*, Berlin Springer Verlag, 2013.
- [31] G. Ghisellini, L. Foschini, M. Volonteri, G. Ghirlanda, F. Haardt, D. Burion, and F. Tavecchio.  
The blazar S5 0014+813: a real or apparent monster?  
*MNRAS*, 399:L24–L28, October 2009.
- [32] G. Ghisellini, L. Maraschi, and F. Tavecchio.  
The Fermi blazars’ divide.  
*MNRAS*, 396:L105–L109, June 2009.
- [33] G. Ghisellini, L. Maraschi, and F. Tavecchio.  
The Fermi blazars’ divide.  
*MNRAS*, 396:L105–L109, June 2009.
- [34] G. Ghisellini, L. Maraschi, and A. Treves.  
Inhomogeneous synchrotron-self-Compton models and the problem of relativistic beaming of BL Lac objects.  
*A&A*, 146:204–212, May 1985.

- [35] G. Ghisellini, G. Tagliaferri, L. Foschini, G. Ghirlanda, F. Tavecchio, R. Della Ceca, F. Haardt, M. Volonteri, and N. Gehrels.  
High-redshift Fermi blazars.  
*MNRAS*, 411:901–914, February 2011.
- [36] G. Ghisellini and F. Tavecchio.  
Canonical high-power blazars.  
*MNRAS*, 397:985–1002, August 2009.
- [37] G. Ghisellini and F. Tavecchio.  
Canonical high-power blazars.  
*MNRAS*, 397:985–1002, August 2009.
- [38] G. Ghisellini and F. Tavecchio.  
Fermi/LAT broad emission line blazars.  
*MNRAS*, 448:1060–1077, April 2015.
- [39] G. Ghisellini, F. Tavecchio, L. Maraschi, A. Celotti, and T. Sbarrato.  
The power of relativistic jets is larger than the luminosity of their accretion disks.  
*Nature*, 515:376–378, November 2014.
- [40] D. Giannios, D. A. Uzdensky, and M. C. Begelman.  
Fast TeV variability in blazars: jets in a jet.  
*MNRAS*, 395:L29–L33, May 2009.
- [41] D. Giannios, D. A. Uzdensky, and M. C. Begelman.  
Fast TeV variability from misaligned minijets in the jet of M87.  
*MNRAS*, 402:1649–1656, March 2010.
- [42] P. Giommi, G. Polenta, A. Lähteenmäki, D. J. Thompson, M. Capalbi, S. Cutini, D. Gasparrini, J. González-Nuevo, J. León-Tavares, M. López-Caniego, M. N. Mazziotta, C. Monte, M. Perri, S. Rainò, G. Tosti, A. Tramacere, F. Verrecchia, H. D. Aller, M. F. Aller, E. Angelakis, D. Bastieri, A. Berdyugin, A. Bonaldi, L. Bonavera, C. Burlina, D. N. Burrows, S. Buson, E. Cavazzuti, G. Chincarini, S. Colafrancesco, L. Costamante, F. Cuttaia, F. D’Ammando, G. de Zotti, M. Frailis, L. Fuhrmann, S. Galeotta, F. Gargano, N. Gehrels, N. Giglietto, F. Giordano, M. Giroletti, E. Keihänen, O. King, T. P. Krichbaum, A. Lasenby, N. Lavonen, C. R. Lawrence, C. Leto, E. Lindfors, N. Mandolesi, M. Massardi, W. Max-Moerbeck, P. F. Michelson,

- M. Mingaliev, P. Natoli, I. Nestoras, E. Nieppola, K. Nilsson, B. Partridge, V. Pavlidou, T. J. Pearson, P. Procopio, J. P. Rachen, A. Readhead, R. Reeves, A. Reimer, R. Reinthal, S. Ricciardi, J. Richards, D. Riquelme, J. Saarinen, A. Sajina, M. Sandri, P. Savolainen, A. Sievers, A. Sillanpää, Y. Sotnikova, M. Stevenson, G. Tagliaferri, L. Takalo, J. Tammi, D. Tavagnacco, L. Terenzi, L. Toffolatti, M. Tornikoski, C. Tringilio, M. Turunen, G. Umama, H. Ungerechts, F. Villa, J. Wu, A. Zacchei, J. A. Zensus, and X. Zhou.  
Simultaneous Planck, Swift, and Fermi observations of X-ray and  $\gamma$ -ray selected blazars.  
*A&A*, 541:A160, May 2012.
- [43] J.-L. Gómez, A. P. Marscher, and A. Alberdi.  
86, 43, and 22 GHz VLBI Observations of 3C 120.  
*ApJL*, 521:L29–L32, August 1999.
- [44] J.-L. Gómez, A. P. Marscher, A. Alberdi, J. M. Martí, and J. M. Ibáñez.  
Subparsec Polarimetric Radio Observations of 3C 120: A Close-up Look at Superluminal Motion.  
*ApJ*, 499:221–226, May 1998.
- [45] J. P. Halpern.  
X-ray spectrum and variability of 3C 120.  
*ApJ*, 290:130–135, March 1985.
- [46] M. J. Hardcastle, M. Birkinshaw, R. A. Cameron, D. E. Harris, L. W. Looney, and D. M. Worrall.  
Magnetic Field Strengths in the Hot Spots and Lobes of Three Powerful Fanaroff-Riley Type II Radio Sources.  
*ApJ*, 581:948–973, December 2002.
- [47] D. E. Harris, J. Hjorth, A. C. Sadun, J. D. Silverman, and M. Vestergaard.  
X-ray emission from the radio jet in 3c 120.  
*The Astrophysical Journal*, 518(1):213, 1999.
- [48] D. E. Harris, A. E. Mossman, and R. C. Walker.  
The X-Ray Jet of 3C 120: Evidence for a Nonstandard Synchrotron Spectrum.  
*ApJ*, 615:161–172, November 2004.

- [49] J. Hjorth, M. Vestergaard, A. N. Sorensen, and F. Grundahl.  
Detection of a Faint Optical Jet in 3C 120.  
*ApJL*, 452:L17, October 1995.
- [50] D. C. Homan, R. Ojha, J. F. C. Wardle, D. H. Roberts, M. F. Aller, H. D. Aller, and P. A. Hughes.  
Parsec-Scale Blazar Monitoring: Proper Motions.  
*ApJ*, 549:840–861, March 2001.
- [51] T. Hovatta, E. Valtaoja, M. Tornikoski, and A. Lähteenmäki.  
Doppler factors, Lorentz factors and viewing angles for quasars, BL Lacertae objects and radio galaxies.  
*A&A*, 494:527–537, February 2009.
- [52] S. Inoue and F. Takahara.  
Electron Acceleration and Gamma-Ray Emission from Blazars.  
*ApJ*, 463:555, June 1996.
- [53] S. Inoue and F. Takahara.  
Electron Acceleration and Gamma-Ray Emission from Blazars.  
*ApJ*, 463:555, June 1996.
- [54] M. Janiak, M. Sikora, and R. Moderski.  
Application of the spine-layer jet radiation model to outbursts in the broad-line radio galaxy 3C 120.  
*MNRAS*, 458:2360–2370, May 2016.
- [55] S. Jester, D. E. Harris, H. L. Marshall, and K. Meisenheimer.  
New Chandra Observations of the Jet in 3C 273. I. Softer X-Ray than Radio Spectra and the X-Ray Emission Mechanism.  
*ApJ*, 648:900–909, September 2006.
- [56] S. G. Jorstad, A. P. Marscher, M. L. Lister, A. M. Stirling, T. V. Cawthorne, W. K. Gear, J. L. Gómez, J. A. Stevens, P. S. Smith, J. R. Forster, and E. I. Robson.  
Polarimetric Observations of 15 Active Galactic Nuclei at High Frequencies: Jet Kinematics from Bimonthly Monitoring with the Very Long Baseline Array.  
*AJ*, 130:1418–1465, October 2005.

- [57] N. S. Kardashev.  
Nonstationarity of Spectra of Young Sources of Nonthermal Radio Emission.  
*AJ*, 6:317, December 1962.
- [58] J. Kataoka, Ł. Stawarz, Y. Takahashi, C. C. Cheung, M. Hayashida, P. Grandi, T. H. Burnett, A. Celotti, S. J. Fegan, P. Fortin, K. Maeda, T. Nakamori, G. B. Taylor, G. Tosti, S. W. Digel, W. McConville, J. Finke, and F. D’Ammando.  
Broad-line Radio Galaxies Observed with Fermi-LAT: The Origin of the GeV  $\gamma$ -Ray Emission.  
*ApJ*, 740:29, October 2011.
- [59] H. T. Liu and J. M. Bai.  
Absorption of 10-200 GeV Gamma Rays by Radiation from Broad-Line Regions in Blazars.  
*ApJ*, 653:1089–1097, December 2006.
- [60] B. Lott, L. Escande, S. Larsson, and J. Ballet.  
An adaptive-binning method for generating constant-uncertainty/constant-significance light curves with Fermi-LAT data.  
*A&A*, 544:A6, August 2012.
- [61] P. Madau and E. S. Phinney.  
Constraints on the Extragalactic Background Light from Gamma-Ray Observations of High-Redshift Quasars.  
*ApJ*, 456:124, January 1996.
- [62] L. Maraschi, G. Ghisellini, and A. Celotti.  
A jet model for the gamma-ray emitting blazar 3C 279.  
*ApJL*, 397:L5–L9, September 1992.
- [63] A. P. Marscher, S. G. Jorstad, J.-L. Gómez, M. F. Aller, H. Teräsranta, M. L. Lister, and A. M. Stirling.  
Observational evidence for the accretion-disk origin for a radio jet in an active galaxy.  
*Nature*, 417:625–627, June 2002.

- [64] H. L. Marshall, B. P. Miller, D. S. Davis, E. S. Perlman, M. Wise, C. R. Canizares, and D. E. Harris.  
A High-Resolution X-Ray Image of the Jet in M87.  
*ApJ*, 564:683–687, January 2002.
- [65] R. Mirzoyan.  
Discovery of Very High Energy Gamma-Ray Emission from the distant FSRQ PKS 1441+25 with the MAGIC telescopes.  
*The Astronomer's Telegram*, 7416, April 2015.
- [66] A. Mücke and R. J. Protheroe.  
A proton synchrotron blazar model for flaring in Markarian 501.  
*Astroparticle Physics*, 15:121–136, March 2001.
- [67] A. Mücke, R. J. Protheroe, R. Engel, J. P. Rachen, and T. Stanev.  
BL Lac objects in the synchrotron proton blazar model.  
*Astroparticle Physics*, 18:593–613, March 2003.
- [68] R. Mukherjee.  
Very-high-energy gamma-ray emission from PKS 1441+25 detected with VERITAS.  
*The Astronomer's Telegram*, 7433, April 2015.
- [69] M. Nenkova, M. M. Sirocky, R. Nikutta, Ž. Ivezić, and M. Elitzur.  
AGN Dusty Tori. II. Observational Implications of Clumpiness.  
*ApJ*, 685:160–180, September 2008.
- [70] M. Ostrowski.  
On possible ‘cosmic ray cocoons’ of relativistic jets.  
*MNRAS*, 312:579–584, March 2000.
- [71] L. Pacciani, F. Tavecchio, I. Donnarumma, A. Stamerra, L. Carrasco, E. Recillas, A. Porras, and M. Uemura.  
Exploring the Blazar Zone in High-energy Flares of FSRQs.  
*ApJ*, 790:45, August 2014.
- [72] A. Paggi, A. Cavaliere, V. Vittorini, F. D’Ammando, and M. Tavani.  
Flaring Patterns in Blazars.  
*ApJ*, 736:128, August 2011.

- 
- [73] B. M. Peterson, L. Ferrarese, K. M. Gilbert, S. Kaspi, M. A. Malkan, D. Maoz, D. Merritt, H. Netzer, C. A. Onken, R. W. Pogge, M. Vestergaard, and A. Wandel.  
Central Masses and Broad-Line Region Sizes of Active Galactic Nuclei. II. A Homogeneous Analysis of a Large Reverberation-Mapping Database.  
*ApJ*, 613:682–699, October 2004.
- [74] T. S. Poole, A. A. Breeveld, M. J. Page, W. Landsman, S. T. Holland, P. Roming, N. P. M. Kuin, P. J. Brown, C. Gronwall, S. Hunsberger, S. Koch, K. O. Mason, P. Schady, D. vanden Berk, A. J. Blustin, P. Boyd, P. Broos, M. Carter, M. M. Chester, A. Cucchiara, B. Hancock, H. Huckle, S. Immler, M. Ivanushkina, T. Kennedy, F. Marshall, A. Morgan, S. B. Pandey, M. de Pasquale, P. J. Smith, and M. Still.  
Photometric calibration of the Swift ultraviolet/optical telescope.  
*MNRAS*, 383:627–645, January 2008.
- [75] J. Poutanen and B. Stern.  
GeV Breaks in Blazars as a Result of Gamma-ray Absorption Within the Broad-line Region.  
*ApJL*, 717:L118–L121, July 2010.
- [76] F. Pozo Nuñez, M. Haas, M. Ramolla, C. Bruckmann, C. Westhues, R. Chini, K. Steenbrugge, R. Lemke, M. Murphy, and W. Kollatschny.  
Modelling photometric reverberation data: a disk-like broad-line region and a potentially larger black hole mass for 3C 120.  
*A&A*, 568:A36, August 2014.
- [77] F. M. Rieger, V. Bosch-Ramon, and P. Duffy.  
Fermi acceleration in astrophysical jets.  
*Ap&SS*, 309:119–125, June 2007.
- [78] P. W. A. Roming, T. S. Koch, S. R. Oates, B. L. Porterfield, D. E. Vanden Berk, P. T. Boyd, S. T. Holland, E. A. Hoversten, S. Immler, F. E. Marshall, M. J. Page, J. L. Racusin, D. P. Schneider, A. A. Breeveld, P. J. Brown, M. M. Chester, A. Cucchiara, M. DePasquale, C. Gronwall, S. D. Hunsberger, N. P. M. Kuin, W. B. Landsman, P. Schady, and M. Still.  
The First Swift Ultraviolet/Optical Telescope GRB Afterglow Catalog.  
*ApJ*, 690:163–188, January 2009.

- [79] H.-J. Röser, K. Meisenheimer, M. Neumann, R. G. Conway, and R. A. Perley.  
The jet of 3C 273 observed with ROSAT HRI.  
*A&A*, 360:99–106, August 2000.
- [80] N. Sahakyan and S. Gasparyan.  
High energy gamma-rays from pks 1441+25.  
*AIP Conference Proceedings*, 1792(1):050005, 2017.
- [81] N. Sahakyan, D. Zargaryan, and V. Baghmanyanyan.  
On the gamma-ray emission from 3C 120.  
*A&A*, 574:A88, February 2015.
- [82] S. Saito, Ł. Stawarz, Y. T. Tanaka, T. Takahashi, G. Madejski, and F. D’Ammando.  
Very Rapid High-amplitude Gamma-Ray Variability in Luminous Blazar PKS 1510-089 Studied with Fermi-LAT.  
*ApJL*, 766:L11, March 2013.
- [83] E. F. Schlafly and D. P. Finkbeiner.  
Measuring Reddening with Sloan Digital Sky Survey Stellar Spectra and Recalibrating SFD.  
*ApJ*, 737:103, August 2011.
- [84] N. I. Shakura and R. A. Sunyaev.  
Black holes in binary systems. Observational appearance.  
*A&A*, 24:337–355, 1973.
- [85] M. S. Shaw, R. W. Romani, G. Cotter, S. E. Healey, P. F. Michelson, A. C. S. Readhead, J. L. Richards, W. Max-Moerbeck, O. G. King, and W. J. Potter.  
Spectroscopy of Broad-line Blazars from 1LAC.  
*ApJ*, 748:49, March 2012.
- [86] M. Sikora, M. C. Begelman, and M. J. Rees.  
Comptonization of diffuse ambient radiation by a relativistic jet: The source of gamma rays from blazars?  
*ApJ*, 421:153–162, January 1994.
- [87] M. Sikora, Ł. Stawarz, R. Moderski, K. Nalewajko, and G. M. Madejski.

- 
- Constraining Emission Models of Luminous Blazar Sources.  
*ApJ*, 704:38–50, October 2009.
- [88] Ł. Stawarz and M. Ostrowski.  
Radiation from the Relativistic Jet: A Role of the Shear Boundary Layer.  
*ApJ*, 578:763–774, October 2002.
- [89] Y. T. Tanaka, A. Doi, Y. Inoue, C. C. Cheung, L. Stawarz, Y. Fukazawa,  
M. A. Gurwell, M. Tahara, J. Kataoka, and R. Itoh.  
Six Years of Fermi-LAT and Multi-Wavelength Monitoring of the Broad-  
Line Radio Galaxy 3c 120: Jet Dissipation At Sub-Parsec Scales from  
the Central Engine.  
*ApJL*, 799:L18, February 2015.
- [90] F. Tavecchio, J. Becerra-Gonzalez, G. Ghisellini, A. Stamerra, G. Bonnoli,  
L. Foschini, and L. Maraschi.  
On the origin of the  $\gamma$ -ray emission from the flaring blazar PKS  
1222+216.  
*A&A*, 534:A86, October 2011.
- [91] F. Tavecchio, L. Maraschi, R. M. Sambruna, and C. M. Urry.  
The X-Ray Jet of PKS 0637-752: Inverse Compton Radiation from the  
Cosmic Microwave Background?  
*ApJL*, 544:L23–L26, November 2000.
- [92] C. M. Urry and P. Padovani.  
Unified Schemes for Radio-Loud Active Galactic Nuclei.  
*AJ*, 107:803, September 1995.
- [93] R. C. Walker, J. M. Benson, and S. C. Unwin.  
The radio morphology of 3C 120 on scales from 0.5 parsecs to 400 kilo-  
parsecs.  
*ApJ*, 316:546–572, May 1987.
- [94] D. R. Xiong and X. Zhang.  
Intrinsic  $\gamma$ -ray luminosity, black hole mass, jet and accretion in Fermi  
blazars.  
*MNRAS*, 441:3375–3395, July 2014.
- [95] V. Zabalza.

naima: a python package for inference of relativistic particle energy distributions from observed nonthermal spectra.

*Proc. of International Cosmic Ray Conference 2015*, page in press, 2015.

[96] J. Zhang, J. M. Bai, L. Chen, and E. Liang.

X-Ray Radiation Mechanisms and Beaming Effect of Hot Spots and Knots in Active Galactic Nuclear Jets.

*ApJ*, 710:1017–1031, February 2010.

# Bibliography

- [1] Abdo, A. A., Ackermann, M. et al. 2009, *ApJ*, 707, 55
- [2] —. 2009, *ApJ*, 699, 31
- [3] —. 2010, *ApJ*, 719, 1433
- [4] —. 2010, *ApJ*, 722, 520
- [5] —. 2010, *ApJ*, 720, 912
- [6] Acero, F., Ackermann, M. et al. 2015, *ApJSS*, 218, 23, 1501.02003
- [7] Ackermann, M., Anantua, R. et al. 2016, *ApJL*, 824, L20
- [8] Aleksić, J., Alvarez, E. A. et al. 2012, *A&A*, 539, L2
- [9] Aleksić, J., Antonelli, L. A. et al. 2014, *A&A*563, A91
- [10] Aleksić, J., Alvarez, E. A. et al. 2014, *A&A*, 564, A5
- [11] Ajello, M., Rebusco, P. et al. 2009, *ApJ*, 690, 367
- [12] Asada, K., Kamenon, S. et al., 2006, *PASJ*, 58, 261
- [13] Atwood, W. B., Abdo, A. A. et al. 2009, *ApJ*, 697, 1071
- [14] Baghmany, V. 2017, *AIP*, 1792, 050007
- [15] Böttcher, M., & Chiang, J. 2002, *ApJ*, 581, 127
- [16] Breeveld, A. A., Landsman, W. et al. 2011, *AIP*, 1358, 373.
- [17] Brown, A. M., and Adams, J. 2011, *MNRAS*, 413, 2785
- [18] Brown, A. M. 2013, *MNRAS*, 431, 824
- [19] Churazov, E., Forman, W. et al., H. 2003, *ApJ*, 590, 225

- [20] Fabian, A. C., Sanders, J. S. et al. 2011, MNRAS, 418, 2154
- [21] Fanaroff, B. L. and Riley, J. M. 1974, MNRAS, 167, 31
- [22] Foschini, L., Ghisellini, G. et al. 2011, A&A, 530, A77
- [23] Foschini, L., Bonnoli, G. et al. A. 2013, A&A, 555, A138
- [24] Gehrels, N., Chincarini, G. et al. 2004, ApJ, 611, 1005
- [25] Giannios, D., Uzdensky, D., and Begelman, M. 2009, MNRAS, 395, L29
- [26] —. 2010, MNRAS, 402, 1649
- [27] Hayashida, M., Nalewajko, K. et al. 2015, ApJ, 807, 79
- [28] Kataoka, J., Stawarz, Ł. et al. 2010, ApJ, 715, 554
- [29] Kirk, J., Rieger, F., and Mastichiadis, A. 1998, A&A, 333, 452
- [30] Lenain, J., Boisson, C., Sol, H., and Katarzyński, K. 2008, A&A, 478, 111
- [31] Li, H., & Kusunose, M. 2000, ApJ, 536, 729
- [32] Lott, B., Escande, L., Larsson, S., and Ballet, J. 2012, A&A, 544, A6
- [33] Lucarelli, F., Pittori, C. et al. 2017, The Astronomer?s Telegram, 9934
- [34] Macías-Ramírez, O., Gordon, C., Brown, A. M., et al. 2012, Phys. Rev. D, 86, 076004, 1207.6257
- [35] Mirzoyan, R. et al. 2017, The Astronomer?s Telegram, 9929
- [36] Mukherjee, R. et al. 2017, The Astronomer?s Telegram, 9931
- [37] Nalewajko, K. 2013, MNRAS, 430, 1324
- [38] Pedlar, A., Ghataure, H. S. et al., 1990, MNRAS, 246, 477
- [39] Pivato, G., Buson, S., 2015, The Astronomer?s Telegram, 8219
- [40] Poole, T. S., Breeveld, A. A. et al. 2008, MNRAS, 383, 627
- [41] Rani, B., Lott, B. et al. 2013, A&A, 557, A71

- [42] Rieger, F. M., Bosch-Ramon, V. & Duffy, P. 2007, *Ap&SS*, 309, 119
- [43] Roming, P. W., Koch, T. S. et al. 2009, *ApJ*, 690, 163
- [44] Saito, S., Stawarz, Ł. et al. 2013, *ApJL*, 766, L11
- [45] Schlafly, E. F., and Finkbeiner, D. P. 2011, *ApJ*, 737, 103
- [46] Tavecchio, F., and Ghisellini, G. 2014, *MNRAS*, 443, 1224
- [47] Vermeulen, R. C., Readhead, A. C. S. and Backer, D. C., *ApJ*, 430L, 41
- [48] Walker, R. C., Romney, J. D. and Benson, J. M., *ApJ*, 430L, 45

